Coversheet: EarthArXiv Preprint

Title: Beyond the 100-kyr and 41-kyr dichotomy: ∼76- and ∼52-kyr signals and forbidden periodicities in Quaternary glacial cycles

Author: Takahito Mitsui

Affiliation: Faculty of Health Data Science, Juntendo University, Urayasu, Chiba 279-0013, Japan

Correspondence: takahito321@gmail.com

Status: This is a non-peer-reviewed preprint submitted to EarthArXiv. The manuscript is under review at a peer-reviewed journal; subsequent versions may differ.

Version: Revised manuscript, 2 October 2026.

Contents: Main text (pp. 1–41), Supplementary Materials (Supplementary Text, Figs. S1 to S22, Table S1; pp. 42–72).

Data availability: Data S1 is archived at `https://doi.org/10.5281/zenodo.19534113`.

Beyond the 100-kyr and 41-kyr dichotomy: ~76- and ~52-kyr signals and forbidden periodicities in Quaternary glacial cycles

Takahito Mitsui

Faculty of Health Data Science, Juntendo University, Urayasu, Chiba 279-0013, Japan.

Email: takahito321@gmail.com

The Mid-Pleistocene Transition (MPT) is often described as a shift from 41-kyr to ~100-kyr glacial cycles, but this dichotomy misses much of the spectral evolution. Using weighted wavelet spectral analysis of benthic δ^{18}O records on tuned and untuned chronologies, we identify overlooked signals, ~52 kyr before 1.2 Ma and ~76 kyr thereafter, marking the MPT's onset. These timescales are integer multiples of the local-mean climatic precession period (T_p), shifted by obliquity, and their timing is set by the 405-kyr eccentricity cycle, near whose minima T_p shortens to ~19 kyr. Other periods are forbidden: successive precession cycles rarely sum to 82–88 or 100–110 kyr, and when T_p is 20.5–22 kyr, high eccentricity triggers early deglaciation, precluding cycles of 60–66 kyr. The pre-MPT regime, ~41 kyr with ~52-kyr cycles, evolved into a post-MPT sequence of quantized ~76-, ~95-, and ~120-kyr cycles. Our results restore precession-based pacing, modulated by obliquity, throughout the Quaternary.

INTRODUCTION

Glacial–interglacial cycles are the dominant mode of Quaternary climate variability, characterized by substantial fluctuations in temperature (*1, 2*), global ice volume (*3, 4*), and atmospheric greenhouse gas concentrations (*5, 6*). Benthic oxygen isotope ratios (δ^{18}O) from marine sediments record past ice volume variations, although they are also influenced by deep-sea temperature and salinity (*7, 8*) (Fig. 1d). Over the course of long-term Cenozoic cooling, the dominant periodicity of these cycles is conventionally described as having shifted from ~41 kyr to ~100 kyr, accompanied by an increase in amplitude—a reorganization known as the Mid-Pleistocene Transition (MPT; 1.25–0.7 Ma) (*4, 9–11*).

While the astronomical influence on glacial cycles via insolation forcing was proposed as early as the mid-19th century, it lacked robust observational support until the late 20th century (*14*). Hays et al. (1976) (*15*) provided the breakthrough by identifying, in the spectra of marine δ^{18}O records, ~19- and ~23-kyr peaks corresponding to climatic precession (Fig. 1b) and a ~41-kyr peak corresponding to obliquity (Fig. 1a) (*12, 16*). The pacemaker of the ~100-kyr cycles, however, remains controversial, because high-latitude summer insolation, considered crucial for the waxing and waning of continental ice sheets, lacks significant power within the ~100-kyr band (*14, 15*): eccentricity enters this insolation mainly by modulating the amplitude of climatic precession, and its ~95-, ~124-, and 405-kyr cycles are the beats among the ~19-, 22.4-, and 23.7-kyr precession terms (*12, 17*). The ~100-kyr cycles are therefore interpreted as nonlinear responses occurring once every four or five precession cycles (*18–21*) or every two or three obliquity cycles (*20, 22, 23*), and whether precession (*21, 24–27*), obliquity (*22*), or a combination of both (*20, 23, 28–32*) is critical for glacial terminations remains debated.

Many studies have investigated the triggers of deglaciations by relating their timing to the phases of obliquity, precession, and various insolation metrics (*21, 23, 27, 28, 32*). However, uniquely defining the timing of deglaciations is inherently challenging, as the process sometimes spans multiple precession cycles and involves several discrete stages of ice-sheet retreat (see below). Although spectral analysis avoids these timing ambiguities, it often lacks the resolution needed to separate the peaks relevant to the precession-versus-obliquity debate at the ~100-kyr scale. Better constraining the climatic rhythms tied to precession over the course of the Pleistocene has been

identified as a key to resolving the MPT (*9*).

Here, we revisit the spectral analysis of glacial-interglacial cycles using a weighted wavelet spectral analysis method, originally developed by Foster (1996) as the Weighted Wavelet Z-transform (*33*) and refined by Kirchner and Neal (2013) (*34*). The method, implemented in the Python package `Pyleoclim` (*35*), estimates spectral power by a localized weighted least-squares projection (Materials and Methods) and yields both the time evolution of the dominant periodicities (scalogram) and the overall power spectral density (PSD) without prior interpolation or detrending. Beyond well-established spectral components, our analysis reveals a distinct ~76-kyr peak after the onset of the MPT (~1.2 Ma) and a ~52-kyr power band before it, across multiple benthic stacks—findings corroborated by conventional spectral estimators and reproduced in two independent model simulations of glacial cycles. Drawing on the theoretical framework of Tzedakis et al. (2017) (*29*), we interpret these periodicities as robust evidence of nonlinear subharmonic (many-to-one) responses of glacial cycles to climatic precession forcing. We further show that the timing of these cycles is set by the 405-kyr eccentricity cycle, near whose minima the precession period shortens to ~19 kyr, and that the orbital configuration also explains why other periods, such as the double-obliquity period of ~82 kyr, are absent.

RESULTS

Weighted wavelet spectral analysis of benthic δ^{18}O records and model outputs

We performed weighted wavelet spectral analysis on seven benthic δ^{18}O records to investigate their periodicities under varying age-modeling constraints, and, for comparison, on the outputs of two models of glacial cycles (Fig. S1; see Materials and Methods). We first consider records whose chronologies involve minimal or no orbital tuning. BIGSTACK$_{\text{magrev}}$ (*7*) is primarily constrained by paleomagnetic events to minimize orbital circularity. The stack of Huybers (2007) (*36*) is derived from depth-based age models. Lisiecki (2010) (*37*) provides an orbital-tuning-free counterpart of the LR04 stack. U1476pMag is a single-site record from IODP Site U1476 anchored to an independent paleomagnetic age model (*26*).

We then consider orbitally tuned records. BIGSTACK$_{\text{mixed}}$ (*7*) uses speleothem-based age

constraints for 0–654 ka and, for earlier intervals, tuning to an ice-sheet model forced by a combination of Northern and Southern Hemisphere summer insolation; $\text{BIGSTACK}_{\text{auto}}$ is generated from $\text{BIGSTACK}_{\text{magrev}}$ using an automated optimization algorithm (*38, 39*) to minimally tune to the pervasive 41-kyr obliquity cycle, while avoiding assumptions about astronomical phase relationships; and the LR04 stack (*8*) is tuned to the same ice-sheet model driven by 65°N summer insolation.

In addition, we analyze the simulated benthic δ^{18}O of Willeit et al. (2019) (*40*), from a transient simulation with the CLIMBER-2 Earth system model of intermediate complexity, and the simulated global ice volume of Pollak et al. (2026) (*41*), from a conceptual ice-age model (RAMP) that closely reproduces reconstructed sea level over the past 2.6 Myr. Being model outputs, these carry no chronological uncertainty and are therefore free of both orbital circularity and sedimentation-rate jitter.

Rather than privileging one chronological strategy, we present the records in three groups—tuning-free or minimally tuned, orbitally tuned, and model output—and ask whether a given periodicity is detected across all three, following previous studies that evaluated orbital variability on both orbitally tuned and tuning-independent chronologies, e.g., (*26, 42*). The two classes of records carry different and largely independent sources of error: records without orbital tuning are free of circularity but retain age uncertainty from unconstrained sedimentation-rate variability, which preferentially attenuates shorter periodicities; orbitally tuned records have better-constrained chronologies but are potentially subject to circularity. Agreement across the groups is therefore stronger evidence than agreement within either one.

The result of time-frequency analysis for $\text{BIGSTACK}_{\text{magrev}}$ is shown in Fig. 1e, with the yellow line tracking the instantaneous period at which the wavelet amplitude is maximized (see Figs. S2–S7 for the other records). Because the wavelet window spans several cycles (Materials and Methods), this dominant period varies smoothly even where the durations of individual glacial cycles change discretely; it should therefore be read as a running measure of the prevailing periodicity rather than as the duration of any single cycle. The dominant periods of the seven records evolve in a broadly similar way (Fig. 1f), except during the MPT (0.7–1.25 Ma), where they differ markedly.

Prior to the MPT, the dominant period remains centered near 41 kyr, although it increases transiently between 1.8 and 2.1 Ma in most records (Fig. 1f), with some variability in timing among the stacks. At the onset of the MPT, the dominant period increases up to ~76 kyr by ~1.2 Ma, a

feature robust across records. This increase is interrupted around 1.1 Ma: during 1.1–0.9 Ma, the dominant period retreats at least once to ~22 kyr in the tuned and untuned LR04 records and to ~41 kyr in the other records, coinciding with the strongest eccentricity maximum of the Quaternary. While the emergence of strong ~100-kyr power after ~700 ka is well documented (*43–45*), the dominant period did not settle at a single value: it remained near ~95 kyr over 700–300 ka and then shifted toward ~120 kyr, reflecting the ~118-kyr duration of the last glacial cycle (MIS 5e to 1; Fig. 1f). After ~700 ka, the dominant period closely follows that of eccentricity (computed with the same wavelet window and excluding the 405-kyr component), suggesting frequency locking between ice volume and the ~100-kyr eccentricity cycles (Figs. 1f and S8). Both model outputs reproduce this progression after ~700 ka (Fig. S9); because they are driven by the same astronomical solution and carry no chronological uncertainty, this agreement supports the frequency locking.

To assess the statistical significance of the observed periodicities, we calculated power spectral densities (PSDs) for the intervals before and after the MPT. For the mid-to-late Pleistocene (the past 1.25 Myr), 95-kyr, 41-kyr, and 23-kyr periodicities generally exhibit significant power at the 95% confidence level (Fig. 2). Notably, a spectral peak near ~76 kyr is significant at the 95% level in five of the seven benthic records, including U1476, in which neither the 41-kyr nor the 23-kyr peak reaches this level; it reaches only the 90% level in the tuned LR04 and is not significant in the untuned LR04, consistent with its age model, which uses only three tie points over 2.6 Myr (*37*) (Materials and Methods). Across the seven benthic records, the maximum power within the 70–82 kyr band lies between 75.3 and 77.2 kyr, a spread of about 2 kyr despite the widely differing age-modeling strategies. Both model outputs show a peak in the same band, at 78.2 and 76.8 kyr (Fig. 2h), indicating that this periodicity arises independently of any proxy chronology.

The strength of the ~76-kyr peak does not increase with the degree of orbital tuning, as it would if tuning had generated it. It is most prominent in $\text{BIGSTACK}_{\text{magrev}}$ with paleomagnetic age constraints and weakest in LR04 in both its tuned and untuned versions (Fig. 2c, g). Because the two LR04 versions share the same $\delta^{18}\text{O}$ data and differ only in chronology, their comparably weak power indicates a property of that stack rather than of its age model.

During the early-to-mid Pleistocene (1.0–2.6 Ma), the 41-kyr spectral peak is prominent across all records (Fig. 3). Enhanced power on the long-period side of this 41-kyr peak is present in most records, but its expression varies. In $\text{BIGSTACK}_{\text{magrev}}$ and Huybers (2007), it appears as a

shoulder extending from the 41-kyr peak toward ~52 kyr; a similar but weaker feature is present in the untuned LR04. In the orbitally tuned records it forms a more distinct peak, at ~50 kyr in the tuned LR04 and ~48 kyr in $\mathrm{BIGSTACK_{auto}}$. In $\mathrm{BIGSTACK_{mixed}}$, by contrast, this band is a local minimum. U1476pMag covers only 786.5 kyr of this interval, which limits the spectral resolution available for such components. Both model outputs also show a peak in this band, at 55.3 and 53.4 kyr, significant at the 95% confidence level (Fig. 3h); as for the ~76-kyr peak, this feature thus arises independently of any proxy chronology. Rather than a single sharp line, it is best described as a band of enhanced power centered near ~52 kyr, hereafter the ~52-kyr band, whose precise period is not tightly constrained by the data.

Neither feature depends on the choice of spectral estimator (Fig. S10). In the five records in which the weighted wavelet spectrum finds the ~76-kyr peak significant, the Lomb–Scargle periodogram also finds it significant, as does the conventional periodogram in all but U1476, where the latter exceeds the threshold only at an isolated frequency. In the untuned LR04, by contrast, the conventional periodogram exceeds the 95% level only at a single isolated frequency near 76 kyr and the Lomb–Scargle periodogram does not reach it at all; the weak expression of this periodicity in the untuned LR04 is therefore a property of that record rather than of any particular estimator. The alternative estimators likewise show enhanced power in the ~52-kyr band in most records. The choice of wavelet estimator also does not alter the timing of the ~76-kyr band: a conventional Morlet transform places its significant intervals at 712–841 and 1060–1203 ka in $\mathrm{BIGSTACK_{magrev}}$ (with a further interval at 2077–2146 ka), closely matching the weighted wavelet result (743–796 and 1114–1167 ka; Fig. S11).

The differences between LR04 and the BIGSTACK records are not attributable to their differing geographical coverage: the Atlantic and Pacific benthic δ^{18}O stacks of Zhou et al. (2026) (*7*) yield spectra highly consistent with those of the global stack (Fig. S12), indicating that the principal periodicities identified here are not restricted to North Atlantic–dominated records. The global mean sea level reconstruction of Clark et al. (2025) (*4*), derived from the Prob-stack benthic δ^{18}O record (*47*), likewise shows the ~76-kyr peak over 0–1.25 Ma and the ~52-kyr peak over 1.0–2.6 Ma (Fig. S13).

In summary, the ~76-kyr peak is a consistent feature of late Pleistocene variability, and the ~52-kyr band, though less consistently expressed, is a real component of early-to-mid Pleistocene

variability rather than an analytical artifact; both are reproducible across datasets and estimators, with detectability depending on the age model. We also note that a ~29-kyr peak, at the sum tone of obliquity and the ~95-kyr eccentricity cycle ($1/29 \approx 1/41 + 1/95$) (*46*), is significant at the 95% level in five of the seven benthic records over the past 1.25 Myr (Fig. 2); relative to the 41-kyr peak, it is 4–18 times stronger than the weak 28.9-kyr obliquity term of the forcing (*17*). Combination tones of this kind (*48*), termed heterodynes in the monsoon literature (*49*), show that nonlinear interactions generate periodicities that are absent from, or far stronger than in, the spectrum of the forcing. The ~76-kyr peak has no counterpart in the spectrum of the forcing, whereas the ~52-kyr band has a weak one, a 53.7-kyr obliquity term whose power is 6% of the 41-kyr line in the 65°N caloric summer insolation, compared with 12–33% in the records (see Discussion). As shown below, we relate both features to precession-paced deglaciations rather than to combination tones or sidebands of the forcing.

Interpretation of ~76-kyr and ~52-kyr components

We interpret the periodicities detected in the PSDs in relation to insolation cycles, using the theoretical framework of interglacial spacing proposed by Tzedakis et al. (2017) (*29*) (T17). In this model, an interglacial occurs when the caloric summer half-year insolation peak at 65°N exceeds a threshold that declines with the time elapsed since the previous interglacial, reflecting the accumulated instability during the glacial period (Materials and Methods). Climatic precession and obliquity contribute almost equally to the variance of this insolation metric (*29*). Its peaks generally follow those of climatic precession, so that their spacing is set primarily by the precession period; obliquity shifts each peak by a few kyr and, by raising or lowering it, helps determine which peaks exceed the threshold. Using this criterion, the model predicts which insolation peaks lead to interglacials over the Quaternary (Fig. 4, filled circles). Though BIGSTACK was recently published (*7*) as an update to LR04, we use LR04 in the following analysis because the T17 model was calibrated using that stack.

We calculate proxy-based deglaciation spacings and insolation-based interglacial spacings, demonstrating their overall consistency. Following T17, interglacials are identified in the LR04 record when δ^{18}O values fall below a predefined threshold (see Materials and Methods). Near each

threshold crossing, the timing of deglaciation is specified as the peak in the derivative of the 10-kyr smoothed LR04 δ^{18}O record (Figs. S14–S16). Some deglaciations span multiple precession cycles, leaving multiple peaks in the δ^{18}O derivative (e.g., deglaciations leading to MIS 13a near 500 ka as well as MIS 17 near 700 ka in Fig. S14). We select the largest derivative peak within a window of either ±10 kyr or ±15 kyr around each threshold-crossing point. The ±10-kyr window tends to capture the later peak within a deglaciation sequence, whereas the ±15-kyr window captures the earlier peak (Figs. S14–S16). The resulting spacings between deglaciations, denoted T_{later} and T_{earlier}, are shown in Fig. 5. We also define the insolation-based interglacial spacing (T_{ins}) as the intervals between successive caloric summer insolation peaks that ultimately led to each interglacial (*29*) (Fig. 5; Fig. 4, filled circles). The proxy-based spacings relate directly to the periodicities in the PSDs but depend on the age model, whereas the insolation-based spacings, once the peaks are identified, are fixed by the astronomical solution and can be linked directly to orbital cycles. See Table S1 for the values of T_{later}, T_{earlier}, and T_{ins} (also provided as Data S1). These spacings agree closely (Fig. 5a; $r \gtrsim 0.95$, RMSE $\lesssim 6.5$ kyr). Discrepancies of up to ~20 kyr for a few deglaciations likely reflect the uncertainty in deglaciation timing and the simplicity of the T17 model, but the overall agreement supports using T_{ins} to interpret the periodicities in the PSDs.

The distribution of T_{ins} is neither unimodal nor smooth (Fig. 5e). Intervals form a broad cluster spanning ~35–53 kyr with a mode near 41 kyr and secondary concentrations near 47–48 and 52 kyr, an essentially empty range at 54–72 kyr, and two narrower clusters at 73–80 and 90–93 kyr. A similar, though more diffuse, structure is preserved in T_{earlier} (Fig. 5d). We therefore attribute the ~95-kyr spectral peak to the 90–93 kyr cluster and the ~76-kyr spectral peak to the 73–80 kyr cluster. This quantization is a property of which insolation maxima cross the deglaciation threshold, and the spectra inherit its structure: the narrow clusters give rise to well-defined spectral peaks, whereas the broad cluster produces a band of enhanced power whose precise period is not tightly constrained. The modest precession power in the δ^{18}O spectra (Figs. 2 and 3) does not conflict with this pacing: precession sets when the threshold is crossed, whereas the amplitude of the response is set by the ice sheet–climate system. The quantized spacings are the signature of such threshold crossing. Independent ice-core chronologies likewise place the last four terminations within the rising phase of Northern Hemisphere summer insolation (*50*). Before the MPT (~1.2 Ma), T_{ins} is distributed around the 41-kyr obliquity period (mean 41.2 kyr, standard deviation 10 kyr), contributing to the

dominant 41-kyr peak; within this broad distribution, four spacings fall within 51–53 kyr (Figs. 4 and 5e), contributing to the enhanced power near 52 kyr in the PSDs over 1.0–2.6 Ma.

Once linked with T_{ins}, the observed spectral peaks can be traced back to their physical origins by decomposing the insolation forcing into climatic precession and obliquity components. The duration of climatic precession cycles varies widely (14–31 kyr) when eccentricity is low but stays near 22 kyr when it is high (Fig. S17) (*51*), and this variability explains the lengths of late-Pleistocene glacial cycles (*21*). Building on this, we derive relationships between T_{ins} and the local durations of precession and obliquity cycles.

For each glacial cycle, we approximate the local variations in the caloric summer insolation as $f(t) = A_p \cos(\omega_p t + \varphi_p) + A_o \cos(\omega_o t + \varphi_o)$, accounting for the respective positive contributions of climatic precession and obliquity to the insolation. Here, $A_{p,o}$ are the local-mean amplitudes, $\omega_{p,o}$ are the angular frequencies (corresponding to local-mean periods $T_{p,o}$), and $\varphi_{p,o}$ are the local phases of climatic precession and obliquity cycles. Unless otherwise noted, we set $A_p = A_o = 1$ (Materials and Methods; Supplementary text). The local-mean periods T_p (T_o) are calculated from the time intervals between successive precession minima (obliquity maxima) associated with deglaciations (Figs. S18–S21; Table S1). The local phases $\varphi_{p,o}$ are chosen from the discrete set $\{0, \pm\pi/2, \pi\}$ for simplicity, to best capture local insolation variations.

We present two representative cases of the resulting approximation formulae for T_{ins}; all derivations are given in the Supplementary text. When the peaks of climatic precession and obliquity nearly coincide and collectively lead to an interglacial, we define this peak time as $t = 0$ by setting $\varphi_p = \varphi_o = 0$ (Fig. S22a). If the spacing T_{ins} between the peak at $t = 0$ and the next peak leading to an interglacial is close to the n-th multiple of the local-mean precession period T_p, it can be expressed as $T_{\mathrm{ins}} = nT_p + \delta$. Here, δ represents a small temporal shift relative to the nominal insolation peak, originating from the modulation by obliquity. By linearizing the peak condition as $f'(nT_p + \delta) \approx f'(nT_p) + f''(nT_p)\delta = 0$, we obtain approximation formulae for T_{ins} ($n = 2, 3, 4, 5$), called type-a:

$$T_{\mathrm{ins}} \approx nT_p - \frac{A_o \omega_o \sin(n\omega_o T_p)}{A_p \omega_p^2 + A_o \omega_o^2 \cos(n\omega_o T_p)}.$$

An example of type-a is the ~76-kyr spacing between interglacials MIS 11c and MIS 9e (Fig. S18), where the insolation peaks are separated by four precession cycles ($n = 4$) with a local-mean period of $T_p = 18.25$ kyr, and the local-mean obliquity period is $T_o = 41.5$ kyr. The type-a formula then

predicts $T_{\rm ins} = 74.3$ kyr. This value is closer to the actual value of 76 kyr than the simple multiple of precession, $nT_p = 73$ kyr, obtained without the shift $\delta = 1.3$ kyr.

The second case occurs when a glacial cycle spans roughly three precession cycles ($n = 3$); the insolation is then locally approximated as $f(t) = -A_p \cos(\omega_p t) - A_o \cos(\omega_o t)$ over the interval $-\frac{3}{2}T_p \lesssim t \lesssim \frac{3}{2}T_p$ corresponding to $\varphi_p = \varphi_o = \pi$ (Fig. S22b). For this case, we assume that deglaciations occur at $t = \pm(\frac{3}{2}T_p + \delta)$, with δ being a small obliquity-induced shift. Following a derivation similar to that of the type-a formulae, $T_{\rm ins}$ is given by the following formula (type-3b):

$$T_{\rm ins} \approx 3T_p + \frac{2A_o\omega_o \sin\left(\frac{3}{2}\omega_o T_p\right)}{A_p\omega_p^2 - A_o\omega_o^2 \cos\left(\frac{3}{2}\omega_o T_p\right)}.$$

An example of type-3b is the spacing between interglacials MIS 37 and MIS 35 (Fig. S19), where the insolation peaks are separated by three precession cycles with a local-mean period of $T_p = 19$ kyr, and the local-mean obliquity period is $T_o = 39$ kyr. Then, the type-3b formula predicts $T_{\rm ins} = 54.2$ kyr. This value is closer to the actual value of 53 kyr than the simple multiple of precession, $nT_p = 57$ kyr, obtained without the shift $\delta = -2.8$ kyr.

In this manner, we derive twelve distinct formulae for $T_{\rm ins}$ depending on the number of precession cycles (n) between successive interglacials and the local phases $\varphi_{p,o}$ (types 2a–5a, 1b–4b, 1c–2c, 2d, and pp). The formulae assigned to the individual glacial cycles are listed in Table S1. These expressions account for all interglacial spacings of the Quaternary except two. While we generally use a fixed amplitude ratio of $A_p/A_o = 1$ for simplicity, we explicitly consider the relative amplitudes in two specific cases of extremely low eccentricity (MIS 99–97 and MIS 97–95). The two exceptions, MIS 95–93 and MIS 93–91, fall in an epoch in which eccentricity remains near zero, so that the precession component of insolation effectively vanishes and the number of precession cycles between peaks is no longer defined; deglaciation instead aligns with the obliquity maximum at 2386 ka. For these two cases, we employ simplified estimates for $T_{\rm ins}$, described in the Supplementary text. Across the Quaternary, the formulae reproduce $T_{\rm ins}$ with a mean absolute error of only 0.8 kyr (Fig. 5b).

Precession phase-locking and forbidden periodicities

The formulae derived above quantize the interglacial spacings in units of the local precession cycle, $T_{\mathrm{ins}} = nT_p + \delta$, consistent with the classical observation that late Pleistocene terminations are separated by four or five precession cycles (*18, 19*). We use this property to explain which periodicities appear in the spectra and which do not. For the 48 spacings to which the formulae apply (all but the two exceptions, MIS 95–93 and MIS 93–91), the obliquity-induced shift δ has a standard deviation of only 2.7 kyr. Consequently, the insolation-based interglacial spacings T_{ins} cluster along the lines $T_{\mathrm{ins}} = nT_p$ ($n = 1, \ldots, 5$) as functions of the local-mean precession period T_p (Fig. 6a). The number of precession cycles within each interglacial spacing, n, can be explained by the T17 theory (*29*), where a longer spacing $T_{\mathrm{ins}} (\approx nT_p)$ facilitates crossing the deglaciation threshold due to the accumulated instability of the ice sheet–climate system (see Materials and Methods). After the onset of the MPT around 1.2 Ma, n statistically increases as a result of an elevated deglaciation threshold, and the points (T_p, T_{ins}) tend to cluster along higher branches with $n \geq 3$.

Figure 6a reveals that similar interglacial spacings (T_{ins}) can arise from different combinations of n and the mean duration of the n precession cycles within each spacing, T_p. The 90–93-kyr spacings comprise either four precession cycles with a mean period of $T_p \approx 23$ kyr or five with $T_p \approx 19$ kyr; the 73–76-kyr spacings, three cycles with $T_p \approx 24$ kyr or four with $T_p \approx 19$ kyr; and the 51–53-kyr spacings, three cycles with $T_p \approx 19$ kyr or two with $T_p \approx 26.5$ kyr. The points in the ~41-kyr cluster lie close to $T_{\mathrm{ins}} = 2T_p$ (Fig. 6a, the second dashed line from the bottom): all 26 spacings in this cluster fall within 4 kyr of this line, with a standard deviation of 1.9 kyr. The durations of the so-called 41-kyr cycles thus vary considerably, from 36 to 51 kyr, and this variability tracks that of the local-mean precession period. Although this is a property of the selected insolation peaks rather than of the proxy record, it independently supports the persistent influence of precession across the MPT reported previously (*26, 42, 52, 53*).

When each combination occurs is set by the 405-kyr eccentricity cycle (Fig. 7). Climatic precession is dominated by two terms with periods of 23.7 and 22.4 kyr, accompanied by a weaker 23.1-kyr term, and by a group of terms near 19 kyr (*12, 17*); the 405-kyr eccentricity cycle is the beat between the first two ($1/405 \approx 1/22.4 - 1/23.7$ kyr^{-1}; Fig. 7a). Near its minima these two terms

cancel, the ~19-kyr terms dominate, and precession cycles shorten to ~19 kyr; elsewhere the 22–24-kyr terms dominate and the cycles are longer (Fig. 7b, c). The duration of n consecutive precession cycles therefore alternates between two levels every ~405 kyr, and the realized interglacial spacings follow these levels (Fig. 7d). All five $n = 4$ spacings of 75–79 kyr lie mostly within the intervals in which the ~19-kyr terms dominate, as do the three $n = 3$ spacings of 52–53 kyr and the $n = 5$ spacing of 93 kyr; the oldest of the $n = 4$ spacings, at ~2.0 Ma, coincides with the transient increase of the dominant period at 1.8–2.1 Ma noted above (Fig. 1f). Outside these intervals, the same numbers of cycles yield 90–92 kyr ($n = 4$), 73–74 kyr ($n = 3$), and 118 kyr ($n = 5$). Each of these spacings spans a ~100-kyr eccentricity minimum, where one precession cycle is lengthened, so that T_p is 23–24 kyr; runs of regular cycles at high eccentricity, with T_p of 20.5–22 kyr, are not realized as long spacings, for the reason given below. The ~76- and ~52-kyr cycles are thus expected mainly near minima of the 405-kyr eccentricity cycle, whenever the deglaciation threshold permits four and three precession cycles, respectively; the two 73–74-kyr spacings of three ~24-kyr cycles near its maxima are the exception and are spectrally indistinguishable from the ~76-kyr peak.

Which interglacial spacings are actually realized, out of the durations that the orbital forcing can potentially produce, is determined by three constraints. Figure 8 presents these durations for the past 2.6 Myr: those of n consecutive precession cycles ($n = 2$–5) and the spacings between 65°N caloric summer insolation peaks that enclose n precession cycles, starting from every peak rather than only from those that led to interglacials.

First, the astronomical forcing itself offers only certain durations. Near each ~100-kyr eccentricity minimum, the phase of climatic precession changes irregularly (*21, 51*), so that one or two precession cycles become anomalously short or long (14–31 kyr, compared with ~22 kyr at high eccentricity; Fig. S17). Four consecutive cycles span about one eccentricity cycle and therefore contain such a minimum in most cases (81%), which makes their total duration either ~76 or ~93 kyr; durations of 82–88 kyr arise only in the few cases that do not (Fig. 8e). Likewise, five consecutive cycles cluster at 91–99 and 111–117 kyr and are rare in the 100–110-kyr band (Fig. 8g). The 65°N caloric summer insolation peaks show the same structure (Fig. 8b, d, f, h).

Second, among the durations that the forcing does offer, high eccentricity removes the longer ones: when T_p falls between 20.5 and 22 kyr, which coincides with high mean eccentricity ($\overline{e} > 0.04$; Fig. 6b), the amplified precession forcing triggers deglaciation within one or two precession cycles

(Fig. 6c), so that durations of 60–66 kyr and the few of 82–88 kyr, both concentrated at high eccentricity, are not realized (Fig. 8c, e).

Third, terminations begin at precession peaks that fall within intervals of above-average obliquity (*29*) and, more specifically, that start while obliquity is rising (*32*). This restricts the candidate peaks to a similar phase of the obliquity cycle, so that spacings near half-integer multiples of T_o, including 60–66 and 100–110 kyr, are disfavored, whereas integer multiples such as 82 kyr are not. Together these constraints account for the gaps in the spacing histograms (Figs. 5c–e).

These constraints also resolve a long-standing puzzle. Glacial cycles of ~80 kyr, two obliquity cycles long, have been proposed as a characteristic duration after the MPT (*20, 22, 36*), and $2T_o$ = 82 kyr is a natural phase-locked period (*54*). Bispectral analysis of the LR04 stack likewise interpreted the ~80-kyr periodicity of the MPT interval as a subharmonic of the 40-kyr obliquity-paced cycle (*53*). Ridgwell et al. (1999) (*19*) noted, however, that pacing by two or three obliquity cycles would produce sidebands not seen in δ^{18}O spectra. Our spectra show directly that 82 kyr is not a peak but a trough: in all seven benthic records and both model outputs, the minimum power within 80–86 kyr is only 13–43% of the lower of the adjacent ~76- and ~95-kyr peaks (Fig. 2). Figure 8 explains why. A ~82-kyr cycle would require four precession cycles averaging 20.5–22 kyr. Such a run occurs only at high eccentricity (Fig. 8e), but high eccentricity triggers earlier deglaciation (Fig. 6c), so that a glacial cycle of 82–88 kyr does not arise.

The proxy-based spacings show the same structure despite timing uncertainties of several kyr: only two of the T_{later} and one of the T_{earlier} spacings fall between 82 and 88 kyr, compared with four and six between 73 and 80 kyr and four each between 89 and 95 kyr (Fig. 5c, d). The gap near the double-obliquity period is thus present in the δ^{18}O record as well, and improved chronologies should resolve it further.

DISCUSSION

The spectral history of Quaternary glacial cycles is richer than a switch from a 41-kyr to a 100-kyr world: a ~52-kyr band accompanied the 41-kyr regime before the MPT, a ~76-kyr peak emerged at its onset (~1.2 Ma) as the ~52-kyr band disappeared, and ~95- and ~120-kyr cycles followed. Of these, ~76, ~95, and ~120 kyr are absent from the spectrum of the insolation forcing, and ~52 kyr

has only a weak counterpart in it. All of these timescales are integer multiples of the local-mean precession period, modulated by obliquity ($T_{\mathrm{ins}} = nT_p + \delta$). Within the T17 framework, precession sets the unit of glacial-cycle duration, obliquity shifts the timing within each unit and helps select which insolation peaks cross the threshold, and the deglaciation threshold, which rose across the MPT, determines how many units each glacial cycle spans. After the end of the MPT (~700 ka), the dominant period, a running measure over several cycles, tracked the ~100-kyr eccentricity component and lengthened from ~95 to ~120 kyr (Fig. 1f). Given the frequency locking between ice volume and eccentricity and the abrupt increase in 100-kyr cycle amplitude at ~700 ka (*43, 44*), we hypothesize that a *resonance* between the two has operated since then (*55*). Alternatively, simple models suggest that the ice–climate system can shift spontaneously between dominant periods without any change in system parameters, through the long memory of ice advection (*56*) or chaotic dynamics (*57*), so that shifts in the dominant period, including this lengthening, need not require an external control.

While the prominence of the ~76-kyr periodicity has been noted in several studies (*21, 58, 59*), its physical origin has remained elusive. For instance, Bolton et al. (1995) (*58*) identified ~75-kyr power around 750 ka but attributed it to internal variability, noting the lack of a corresponding periodicity in the astronomical forcing. Rial (1999) (*59*) proposed that the ~75-kyr peak is a sideband frequency ($1/77 \approx 1/95 + 1/413$) generated by frequency modulation of the 95-kyr cycle by the 413-kyr eccentricity component, and illustrated it with a parametrically excited oscillator, but left the mechanism of the modulation unresolved. Verbitsky et al. (2019) (*60*) proposed that the ice sheet–climate system may exhibit ~70-kyr spectral power generated by low-frequency beating among multiple millennial-scale oscillations.

Our results instead indicate that the ~76-kyr spectral power arises from subharmonic phase-locking to either three precession cycles (mean period $T_p \approx 24$ kyr) or four precession cycles ($T_p \approx 19$ kyr), with minor modulation by obliquity. Rial described the ~400-kyr alternation between ~80- and ~120-kyr glacial cycles as frequency modulation of the ~100-kyr eccentricity signal by its 413-kyr component; in our framework, four-cycle spacings of ~76 kyr near the minima of the 405-kyr cycle alternate with four- or five-cycle spacings of ~92–118 kyr elsewhere, because deglaciations are paced by precession cycles whose period is itself switched by the 405-kyr beat (Fig. 7). Blackburn et al. (2024) (*21*) likewise identified glacial cycles of 76–77 kyr spanning four

precession cycles (MIS 21 to 17) and attributed their variable duration to the eccentricity-modulated precession period, a dependence that is well established (*51*); what we add is that the 405-kyr beat of the 23.7- and 22.4-kyr terms sets the two levels of that duration. This precession-based 76-kyr mode is distinct from the previously proposed ~70-kyr variability, interpreted as a beat between obliquity and eccentricity ($1/70 \approx 1/41 - 1/100$) in marine δ^{18}O (*46*) and in East Asian monsoon records (*61*). Within our framework, the ~95-kyr spectral power likewise arises from phase-locking to four ($T_p \approx 23$ kyr) or five ($T_p \approx 19$ kyr) precession cycles (*18, 19, 21, 24, 25, 27*).

While the dominant power prior to the MPT is often characterized as ~41 kyr (*62*), this represents only a statistical average. In reality, interglacial spacings exhibit large variations of ~10 kyr around this mean because they correspond to either two or three multiples of climatic precession cycles, whose periods themselves vary significantly. Such variability in glacial duration is indeed reproduced in a conceptual ice-age model (*41*) and a climate–ice sheet model (*52*) (Fig. 3h). Our analysis identifies the ~52-kyr band on the long-period side of the 41-kyr peak as a diagnostic signature of this precessional influence prior to the onset of the MPT (~1.2 Ma). Spectral power near 50 and 55 kyr can in principle arise as an overtone of the 100-kyr band ($1/50 = 2/100$ kyr^{-1}) and as a sideband of obliquity, as Huybers and Wunsch (2004) (*46*) showed for a synthetic orbital signal. In contrast, we attribute the ~52-kyr band to a subharmonic response to two or three precession cycles (Fig. 6a). The obliquity sideband is real: the obliquity solution contains a 53.7-kyr term (*12*) whose power in the 65°N caloric summer insolation is 6% of that of the 41-kyr line, and a linear response to it may contribute to the band, particularly where the band peaks at 50–56 kyr (U1476, the tuned LR04, and the two models). The band is, however, two to five times stronger relative to the 41-kyr peak than in the forcing, and the interglacial spacings that fall within it (47–48 kyr from two precession cycles of 25–26 kyr, and 51–53 kyr from three cycles of 18–20 kyr or two of 26.5 kyr; Table S1) give it a time-domain origin that the obliquity term alone does not provide, including the timing of the three-cycle spacings of 52–53 kyr near minima of the 405-kyr eccentricity cycle (Fig. 7d). We therefore regard the threshold selection of precession peaks as the primary origin of the ~52-kyr band, with a linear response to the obliquity term as a secondary contribution superimposed on it.

The ~52-kyr band invites comparison with the heterodyne of precession and obliquity reported in monsoon records. For example, Clemens et al. (2010) (*63*) interpreted a 52.6-kyr peak in

Chinese cave δ^{18}O as the difference tone of obliquity and the 23-kyr component of precession ($1/23 - 1/41 \approx 1/52.4$). The mechanism proposed here is different: the ~52-kyr spacings arise from deglaciations paced by two or three precession cycles, $T_{\mathrm{ins}} = nT_p + \delta$, in which obliquity enters only through the small shift δ rather than through a product of the two forcings, so that T_{ins} is not the heterodyne period $1/(1/T_p - 1/T_o)$. The two descriptions are not mutually exclusive: a heterodyne characterizes the spectral signature of the precession–obliquity interaction, whereas the present framework describes its time-domain expression for ice volume and explains the timing of individual deglaciations (mean absolute error of 0.8 kyr), which we regard as essential to understanding the ~52-kyr band.

The presence of bundles of precession cycles—~52-kyr cycles before ~1.2 Ma, ~76-kyr cycles after ~1.2 Ma, and ~95-kyr cycles after ~0.9 Ma—throughout the Pleistocene suggests that the MPT was not a disappearance of the obliquity-driven 41-kyr world, but rather a progressive shift in the skipping behavior of precession-paced deglaciations. This persistent influence of precession cycles both before and after the MPT is consistent with recent findings (*26, 42, 52, 53, 64*). Obliquity thus plays the dual role introduced above: it determines which precession peaks are skipped (*21, 28–30, 32*), and it shifts each spacing away from an exact multiple of the precession period by the small amount δ.

Consequently, the MPT can be understood as a period-adding sequence in precession phase-locking that, within the conceptual framework adopted here, is represented by a gradual rise in the effective deglaciation threshold of the coupled ice-sheet–ocean–carbon system (Materials and Methods). This threshold is not a single physical quantity but an effective phenomenological parameter that summarizes unresolved long-term changes in the coupled climate system affecting the stability of Northern Hemisphere ice sheets; the underlying processes remain uncertain. One plausible explanation, synthesized by Clark et al. (2025) (*4*), is that progressive cooling of the Southern Hemisphere (*1*) drove an equatorward shift of the westerlies (*65*), an increase in dust flux to the Southern Ocean (*66*), and greater stratification of its surface waters (*67*). The resulting increase in glacial carbon storage lowered glacial atmospheric CO_2 (*68–70*) and increased the glacial–interglacial amplitude of CO_2 (*4, 69, 70*), thereby stabilizing Northern Hemisphere ice sheets against deglaciation; changes in deep-ocean stratification (*71*) and in North Atlantic deep-water formation (*72*) may have contributed. The coeval expansion of marine-based Antarctic ice

sheets is also consistent with this long-term evolution (*72, 73*). An alternative hypothesis invokes progressive removal of subglacial regolith beneath the Laurentide ice sheet, favoring thicker, more stable ice (*40, 74*), for which some geochemical evidence exists (*75*). Sea-level reconstructions indicating that early-Pleistocene Northern Hemisphere ice sheets were already comparable in volume to those of the Last Glacial Maximum weigh against the low-aspect-ratio ice sheets that this hypothesis requires (*4*). Estimates of early-Pleistocene ice volume differ among methods, however: Mg/Ca-based and noble-gas-based decompositions of the benthic δ^{18}O record indicate enhanced ice-sheet growth across the MPT (*76, 77*). Identifying which of these processes raised the threshold is beyond the scope of this study; our framework requires only that it rose across the MPT, so that glacial cycles lengthened from two or three precession cycles to four or five.

The three constraints identified above (Fig. 8) preclude cycles of ~60–66, ~82–88, and ~100–110 kyr. The role of high eccentricity in terminating cycles early is consistent with the anticorrelation between ~100-kyr eccentricity power and ~100-kyr ice-age power reported previously (*37, 52*). Our analysis shows that mean eccentricity does not exceed 0.04 during the observed ~100-kyr cycles (Fig. 6c). This implies that the development of ~100-kyr cycles was precluded during the high-eccentricity interval between ~950 and 1100 ka. Consequently, the onset of the MPT—specifically the lengthening of glacial cycles—appears to have been constrained by the long-term evolution of eccentricity (*11, 52*). Herbert (2023) (*9*) argued that the MPT puzzle will be resolved when climatic rhythms tied to precession are better constrained over the course of the Pleistocene; the quantized interglacial spacings and their 405-kyr timing identified here provide one such constraint. The framework also yields a test that discriminates between precession pacing and a direct response to obliquity in the 41-kyr world: if deglaciations are paced by precession, proxy-derived spacings should shorten to 37–40 kyr (two precession cycles) or lengthen to ~52 kyr (three) near minima of the 405-kyr eccentricity cycle and lie at 42–48 kyr elsewhere (Fig. 7d), whereas a direct response to obliquity would keep them near 41 kyr (37–45 kyr, the range of the local obliquity period) irrespective of the phase of the 405-kyr cycle. Applying this test to high-resolution records of the early Pleistocene and Pliocene is a natural next step.

MATERIALS AND METHODS

Benthic δ^{18}O records

We analyze seven benthic δ^{18}O records (Fig. S1) categorized by their degree of orbital tuning. Three of them are the BIGSTACK chronologies of Zhou et al. (2026) (*7*), which place the same stack of 221 records on different age models. Among the records with minimal or no orbital tuning, the age model of $\text{BIGSTACK}_{\text{magrev}}$ is derived from 33 cores with paleomagnetic measurements and is constrained by 15 paleomagnetic events over the last 2.606 Ma to minimize orbital circularity. The δ^{18}O stack of Huybers (2007) (*36*) is based on a depth-derived age model; while the original study focuses on the last 2 Ma, the dataset provides a tuning-free chronology anchored to the 2.58 Ma geomagnetic boundary (`https://doi.org/10.25921/d1zr-t492`, last accessed 8 April 2026). The tuning-free version of the LR04 stack from Lisiecki (2010) (*37*) assumes a constant sedimentation rate between three primary tie points: the core top (0 ka) and the geomagnetic reversals at 0.78 and 2.6 Ma. The single-site benthic δ^{18}O record from IODP Site U1476 is anchored to an independent paleomagnetic age model (U1476pMag) (*26*); because this record spans only the last 1786.542 kyr, its coverage of the pre-MPT interval (1.0–1.79 Ma) is relatively short, and the presence or absence of periodicities in this epoch should be interpreted with caution.

Among the orbitally tuned records, $\text{BIGSTACK}_{\text{mixed}}$ uses speleothem-based age constraints for 0–654 ka and, for earlier intervals, tuning to an ice-sheet model (*78*) forced by a combination of Northern and Southern Hemisphere summer insolation. $\text{BIGSTACK}_{\text{auto}}$ is derived from $\text{BIGSTACK}_{\text{magrev}}$ by applying the eTimeOpt algorithm (*38, 39*) to minimally tune the pervasive 41-kyr obliquity signal without assuming astronomical phase relationships. The standard LR04 stack (*8*) is tuned to the same ice-sheet model driven by 65°N summer insolation.

As described in Results, we do not treat any single class of chronology as decisive: we regard a periodicity as robust when it is detected across the tuning-free, orbitally tuned, and model groups, and we report the degree of tuning explicitly for each record.

Model outputs

For comparison with the proxy records, we analyze the outputs of two models of glacial cycles. The first is the RAMP model of Pollak et al. (2026) (*41*), a conceptual model in which the deglaciation threshold rises in a ramp-like manner across the MPT; we use the simulated global ice volume from the run tuned to the sea level reconstruction of Berends et al. (2021) (*10*). The second is the transient simulation of Willeit et al. (2019) (*40*) with the CLIMBER-2 Earth system model of intermediate complexity, driven by orbital forcing together with prescribed scenarios of gradual regolith removal and declining volcanic CO_2 outgassing; here we analyze the simulated benthic $\delta^{18}O$, which is directly comparable to the proxy records. Both are forced by the astronomical solution of Laskar et al. (2004) (*12*), so their time axes are exact by construction. We note that the RAMP model is calibrated against a sea level target derived from the LR04 stack; this calibration adjusts a small number of scalar parameters and cannot transfer spectral structure from that stack, and the CLIMBER-2 simulation is independent of LR04 in any case. Model outputs are analyzed with the same procedure as the proxy records.

Weighted wavelet spectral analysis

Paleoclimate time series are commonly unevenly spaced, which complicates the application of conventional spectral estimators, such as the periodogram (*79*) and the multitaper method (*80*). Standard approaches often rely on interpolation to a regular time grid prior to analysis; however, such interpolation acts as a low-pass filter, leading to a reddening of the power spectrum and, consequently, spurious results in hypothesis testing (*81*). While the Lomb–Scargle periodogram (*82, 83*) avoids interpolation, it is known to overestimate power at high frequencies (*81*). Moreover, Fourier-based methods, which assume stationarity, necessitate data detrending (*84*). However, even with recent methodological advances, identifying and removing a trend without inadvertently compromising the underlying climate signal remains an inherently difficult task (*85*). These issues are directly relevant here: four of the seven observational records are not uniformly spaced (Fig. S1).

To address these difficulties, we primarily employ a weighted wavelet spectral analysis method, which directly accommodates variable sampling intervals without interpolation, and use Lomb–Scargle periodograms as an independent complementary analysis. The former, originally developed

by Foster (1996) (*33*) as the Weighted Wavelet Z-transform (WWZ) and subsequently refined by Kirchner and Neal (2013) (*34*), estimates spectral power via weighted least-squares projection. Implemented in the Python package `Pyleoclim` (*35*), it resolves both the time-evolving nature of dominant periodicities (scalograms) and the overall frequency content (power spectral density; PSD) without requiring prior interpolation or detrending. Because different spectral estimators involve different trade-offs between spectral resolution, variance reduction, and significance estimation, we do not expect identical results from every method, especially for weaker spectral features near the significance threshold. We also compared the weighted wavelet scalograms with those from a conventional continuous wavelet transform, which requires interpolation onto a uniform grid (Fig. S11); the timing of the ~76-kyr band is essentially unchanged, though the conventional transform yields somewhat broader significant intervals, consistent with the smoothing introduced by interpolation.

The method estimates time-dependent harmonic amplitudes (a_1, a_2) through localized fits of sinusoidal functions and a constant to the data using weighted least squares (*34*). Specifically, for each center time t^* and angular frequency ω, the coefficients a_1 and a_2 are obtained by fitting: $x_i = a_0 + a_1 \cos[\omega(t_i - t^*)] + a_2 \sin[\omega(t_i - t^*)]$, where each observation x_i at time t_i is weighted by a Gaussian weight $w_i = \exp[-c\omega^2(t_i - t^*)^2]$, with a decay constant c controlling the time-frequency resolution trade-off. However, when the data are unevenly spaced in time, the basis functions can be non-orthogonal (e.g., $\sum_i \cos[\omega(t_i - t^*)] \sin[\omega(t_i - t^*)] \neq 0$), which can lead to significant errors in estimating the coefficients. To address this, Kirchner and Neal (2013) fit instead $x_i = b_0 + b_1 (\cos[\omega(t_i - \tau)] - \bar{c}) + b_2 (\sin[\omega(t_i - \tau)] - \bar{s})$, where $\bar{c}$ and $\bar{s}$ are the weighted means of $\cos[\omega(t_i - \tau)]$ and $\sin[\omega(t_i - \tau)]$, so that the two centered terms are orthogonal to the constant term, and the time shift τ is chosen so that they are also orthogonal to each other under the weights. With all three basis functions mutually orthogonal, b_1 and b_2 follow from simple weighted projections; the centering only redefines b_0. The coefficients b_0, b_1, and b_2 obtained via weighted regression are then converted back to the original coefficients a_0, a_1, and a_2 by accounting for the phase shift $\omega(t^* - \tau)$.

The local spectral power, or scalogram, is calculated at each t^* as: $S_{\mathrm{loc}}(t^*, \omega) = \frac{1}{2}(a_1^2 + a_2^2)(t_{\max} - t_{\min})\frac{n_{\mathrm{eff}}}{n}$, where $t_{\max} - t_{\min}$ is the total time interval covered by the n samples, and $n_{\mathrm{eff}} = (\sum_i w_i)^2 / \sum_i w_i^2$ represents the effective number of points. Finally, a robust global estimate of

the power spectral density (PSD) is obtained by averaging the local spectral power over the entire time interval, as $S(\omega) = \sum_{t^*} v_{\text{eff}}(t^*) S_{\text{loc}}(t^*, \omega) / \sum_{t^*} v_{\text{eff}}(t^*)$, where $v_{\text{eff}}(t^*) = \max\{0,\, n_{\text{eff}} - 3\}$ is the effective degrees of freedom (*34*).

The decay constant c determines the frequency resolution in the spectral analysis and balances the frequency and time resolution in the time-frequency analysis. For the time-frequency analysis (scalogram), we adopt $c = 1/(8\pi^2)$, the standard value for this analysis in `Pyleoclim` (*35*), which provides a balanced resolution for identifying transient shifts in ice age periodicity. With this value, the Gaussian weight at period $T = 2\pi/\omega$ reduces to $w_i = \exp[-(t_i - t^*)^2/(2T^2)]$, i.e., a window whose standard deviation equals the period, so that the local power at period T is effectively averaged over roughly $\pm 2T$, or several cycles. For the global spectral analysis (PSD), we set $c = 0.0005$, half the default value of 0.001 in `Pyleoclim`; the smaller c gives a broader effective time window and hence higher frequency resolution.

The frequency grid on which the spectrum is evaluated is a separate matter from the resolution set by c. Because the weighted least-squares projection is evaluated at whatever frequencies are specified, the spectrum can be sampled arbitrarily finely without altering the estimate itself. We use a logarithmic grid of 1000 points for the PSDs in Figs. 2 and 3, giving a spacing of about 0.5 kyr near 76 kyr compared with 4–6 kyr on the default grids of `Pyleoclim`, so that reported peak positions are not affected by rounding to grid nodes. To limit computational cost, the AR(1) confidence levels are computed on the default grid. All confidence levels, for both the PSDs and the scalograms, are estimated from 1000 AR(1) surrogates.

To check the sensitivity of our results, we also compute the conventional periodogram (*79*) and the Lomb–Scargle periodogram (*82, 83*) (Fig. S10). For the former, the time series is interpolated at 1-kyr intervals. In both cases, the series are linearly detrended over the analysis period. All analyses are performed with `Pyleoclim` (version 1.2.0) (*35*).

Interglacial spacings in Tzedakis et al. (2017)

Tzedakis et al. (2017) proposed a simple rule to determine which insolation peaks trigger interglacials (*29*). In their model, 51 interglacials are identified over the Quaternary based on the LR04 benthic δ^{18}O stack (*8*), supported by additional composite records from Eastern Equatorial Pacific

sites. An interglacial onset is defined when the detrended δ^{18}O value falls below a lower threshold of 3.68 ‰ after having exceeded a higher threshold of 3.92 ‰. To apply this criterion consistently, δ^{18}O values prior to 1.5 Ma are detrended as $\delta^{18}O_{\text{detrended}} = \delta^{18}O + 3.296 \times 10^{-4}(t - 1500)$, where t is the time in kyr, while values after 1.5 Ma remain unchanged. This trend is attributed to the long-term cooling of deep-water temperatures or an increase in Antarctic ice volume.

The T17 model predicts interglacial onsets based on caloric summer half-year insolation. This measure represents the total insolation integrated over the caloric summer half-year, which is defined such that every day within this period receives more insolation than any day in the winter half (*13,86*). At 65°N, the variance of this insolation measure receives approximately equal contributions from climatic precession and obliquity (*29*): over the past 2.6 Myr, linear regression of the series on climatic precession and obliquity attributes 50% and 49% of its variance to the two components, which together account for 99.7% of the total. In the T17 framework, an interglacial is triggered when a peak in the 65°N caloric summer insolation exceeds a threshold that decreases as a function of the time elapsed since the previous interglacial (Δt), reflecting the accumulation of glacial instability. This condition can be expressed as the effective energy, defined as $E(I_{\text{peak}}, \Delta t) = I_{\text{peak}} + b\Delta t$, exceeding a constant deglaciation threshold $I_{\text{threshold}}$. Here, $b = 0.0021 \pm 0.0001$ GJ m^{-2} kyr^{-1}, and $I_{\text{threshold}}$ is defined to ramp up from 6.02 GJ m^{-2} to 6.14 GJ m^{-2} over the interval from 1.55 Ma to 0.61 Ma. Using this criterion, the model can predict most of the 51 interglacial onsets, with only two false negatives (MIS 59 and 63). For these false negatives, the insolation peaks immediately preceding their respective isotopic minima are assumed to be the trigger. In the present work, the interglacial spacings (T_{ins}) are defined as the durations between successive caloric summer insolation peaks that led to each interglacial. Using T17, the interglacial spacing T_{ins} is determined as the minimal peak-to-peak spacing that satisfies the condition $E(I_{\text{peak}}, T_{\text{ins}}) = I_{\text{peak}} + bT_{\text{ins}} > I_{\text{threshold}}$. Therefore, $n = \text{argmin}_{\tilde{n}\geq 1}\{I_{\text{peak}} + b(\tilde{n}T_p + \delta) > I_{\text{threshold}}\}$.

Decomposition of climatic precession

Because the mechanism of Fig. 7 concerns the duration of individual precession cycles, we decompose climatic precession $e \sin \varpi$ itself rather than eccentricity; eccentricity is the amplitude envelope of $e \sin \varpi$, so the decomposition describes both. Here ϖ is the longitude of perihelion

measured from the moving equinox in the convention of Laskar et al. (2004) (*12*), in which $e \sin \varpi$ is minimal when perihelion occurs at the boreal summer solstice; throughout this paper, the series computed with `palinsol` (*13*), which follows the convention of Berger (1978) (*17*), is sign-reversed to this convention.

Climatic precession is well approximated by a sum of sinusoids with frequencies $p + \mu_k$, where p is the precession frequency and μ_k are the secular frequencies of the planetary system (*12, 17*). Laskar et al. (2004) (*12*) expand $e \exp(i\varpi')$, where ϖ' is measured from the fixed equinox of J2000, over the interval from −15 to +5 Myr; the phases of the climatic precession terms therefore depend on the precession angle, and we fitted the five leading terms directly to the La2004 solution over the past 2.6 Myr, taking $p = 50.4677''\ \mathrm{yr}^{-1}$ and μ_k (g_5, g_2, g_1, g_4, g_3) as initial frequencies, refining them by nonlinear least squares (they change by less than 0.1%), and estimating amplitudes and phases by linear least squares. The fit explains 98.7% of the variance. The fitted periods are 23.68, 22.37, 23.10, 18.96, and 19.09 kyr, with amplitudes of 0.0188, 0.0169, 0.0045, 0.0154, and 0.0078, respectively; the modulus of the sum of the five complex terms reproduces eccentricity with a correlation of 0.98. The curves in Fig. 7a are the real parts of the sums of the first three terms (22–24-kyr group) and of the last two (~19-kyr group), and the envelopes in Fig. 7a, b are their moduli.

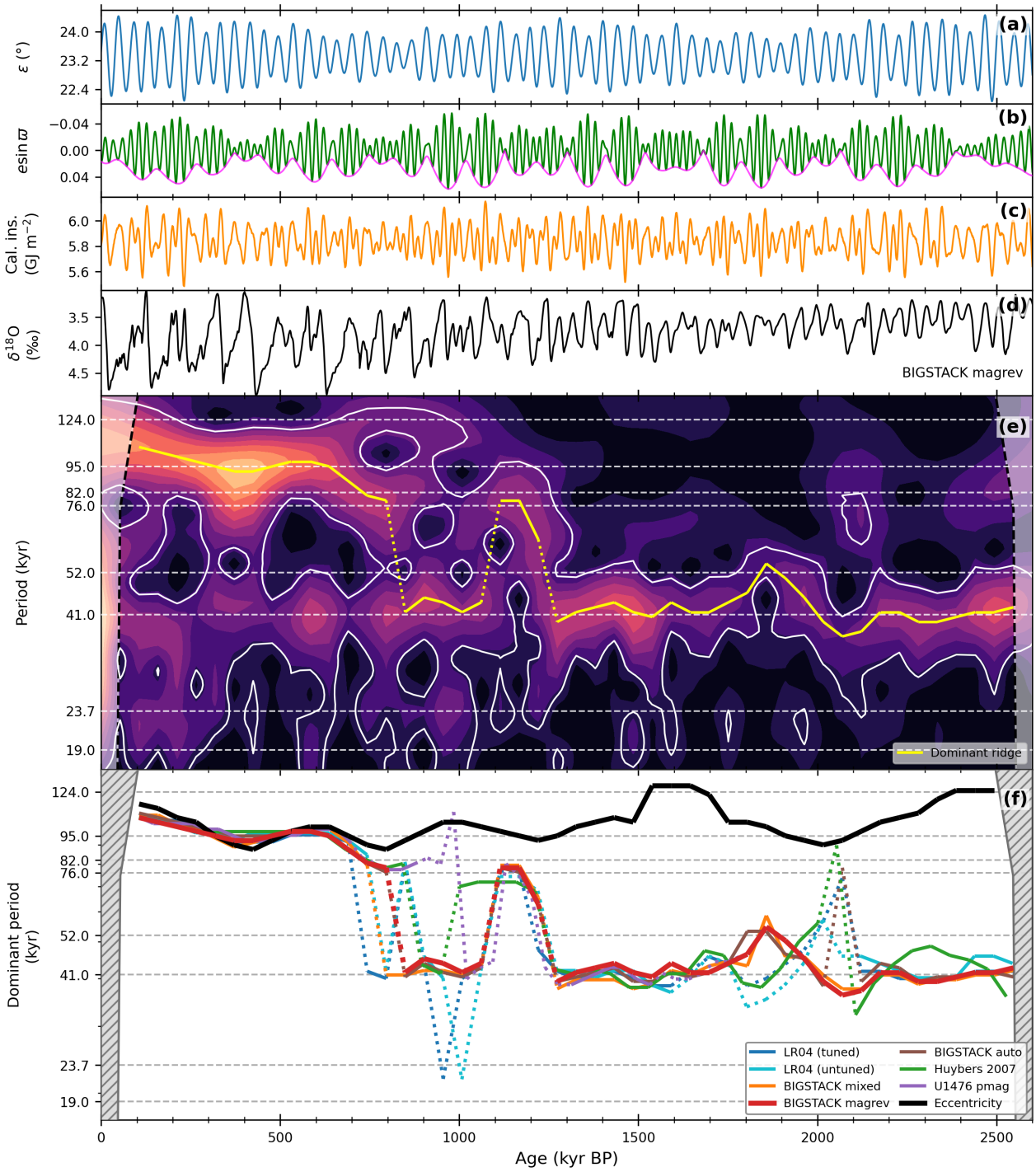


Figure 1: **Orbital forcing and wavelet analyses of the BIGSTACK$_{\text{magrev}}$ benthic δ^{18}O stack record over the last 2.6 Myr. The full caption is given on the following page.**

Figure 1 (continued). (a) Obliquity (ε) and (b) climatic precession ($e \sin \varpi$, green) with its eccentricity envelope (e, magenta) (*12*); negative values of climatic precession correspond to positive anomalies in Northern Hemisphere summer insolation. (c) Caloric summer half-year insolation at 65°N (*13*). (d) BIGSTACK$_{\text{magrev}}$ benthic δ^{18}O stack (*7*), whose age model is anchored to paleomagnetic events rather than orbital tuning. (e) Wavelet power scalogram of the record in (d). The yellow line traces the ridge of maximum wavelet power; white dashed contours enclose power significant at the 95% confidence level against an AR(1) benchmark; horizontal dashed lines mark the periodicities discussed in the text. (f) Dominant period, defined as the period of maximum wavelet power at each time, for the seven benthic δ^{18}O records analyzed here and for eccentricity (black; excluding the ~405-kyr band). Solid segments join successive time points at which the ridge power is significant at the 95% level; segments are dotted where it is not, or where the dominant period switches between spectral bands (a change by more than a factor of 1.5 between successive points), that is, where two components exchange rank. The shaded region marks the cone of influence of BIGSTACK$_{\text{magrev}}$, within which the ridge is not shown.

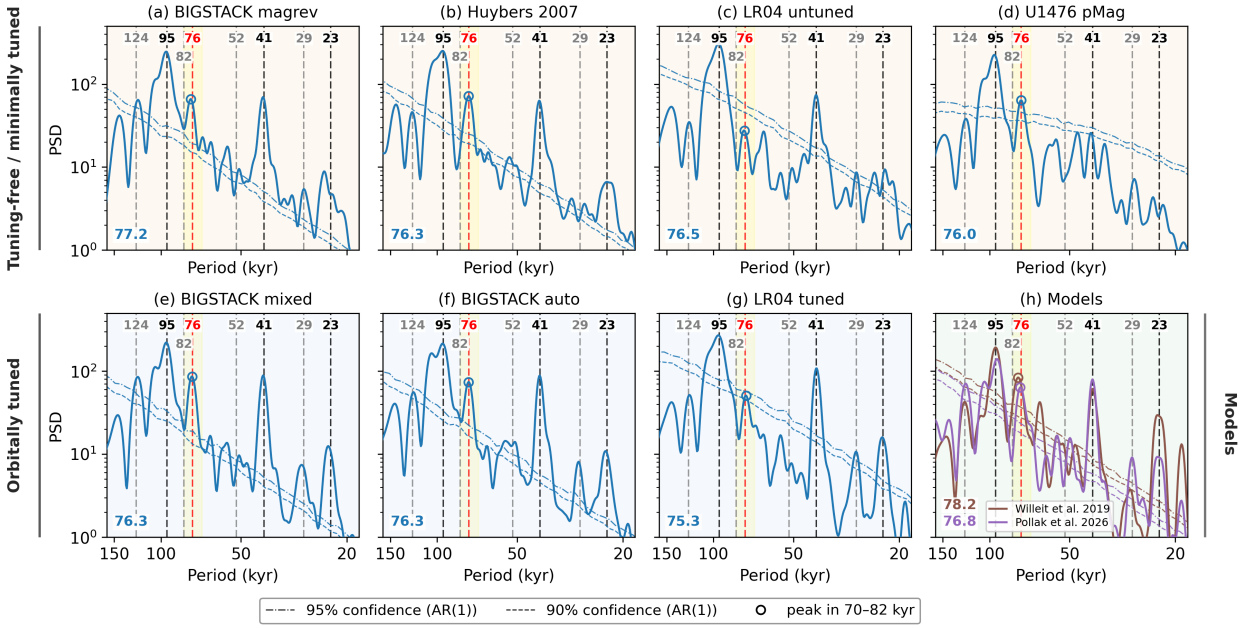


Figure 2: **Power spectral densities (PSD) of benthic δ^{18}O records and model outputs over the last 1.25 Myr.** Panels are grouped by the degree of orbital tuning. Tuning-free or minimally tuned records: (a) BIGSTACK$_{\text{magrev}}$ (*7*), (b) the untuned record from Huybers (2007) (*36*), (c) the untuned LR04 stack (*37*), and (d) the U1476 record (*26*). Orbitally tuned records: (e) BIGSTACK$_{\text{mixed}}$ (*7*), (f) BIGSTACK$_{\text{auto}}$ (*7*), and (g) the tuned LR04 stack (*8*). Model outputs: (h) Willeit et al. (2019) (*40*) and Pollak et al. (2026) (*41*). Solid lines denote the PSD of the standardized series, and dashed/dotted lines indicate the 95% and 90% confidence levels against an AR(1) benchmark. Vertical dashed lines highlight key periodicities: eccentricity (124 and 95 kyr), obliquity (41 kyr), and climatic precession (23 kyr). Also indicated are the subharmonic of 41 kyr (82 kyr), the combination tone (29 kyr; $1/29 \approx 1/41 + 1/95$) (*46*), and specific timescales of interest in this study (76 kyr, red, and 52 kyr). The shaded band marks the 70–82 kyr interval; open circles and the numbers at the lower left of each panel give the period of maximum PSD within this band. Spectra are evaluated on a logarithmic frequency grid of 1000 points so that peak positions are not affected by rounding to grid nodes. This refines the sampling of the spectrum rather than its resolution, which is set by the wavelet window width and the record length; the confidence levels are computed on the default grid.

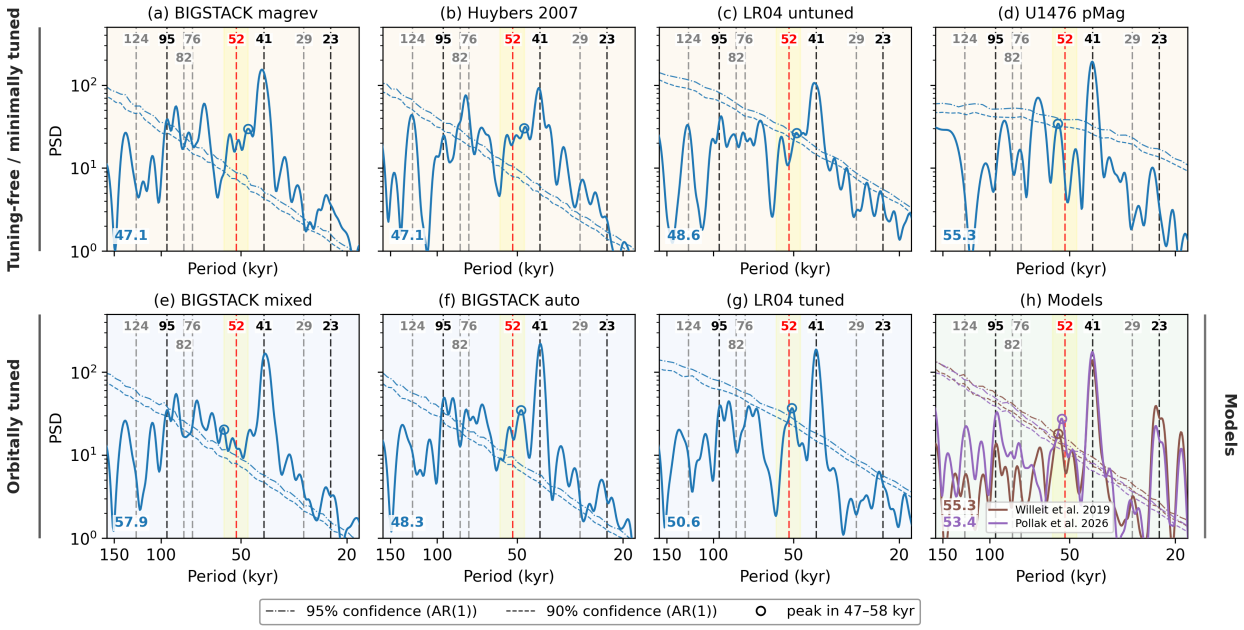


Figure 3: **Power spectral densities (PSD) of benthic δ^{18}O records and model outputs over 1.0–2.6 Ma.** Panels, line styles, and vertical dashed lines are as in Fig. 2, except that the 52-kyr line is shown in red. In contrast to the ~76-kyr peak in Fig. 2, the enhanced power near 52 kyr does not form a single well-defined peak but is distributed over a broader band; the shaded band marks the 47–58 kyr interval, and open circles and the numbers at the lower left of each panel give the period of maximum PSD within this band, which should be read as indicative rather than as a well-constrained peak period.

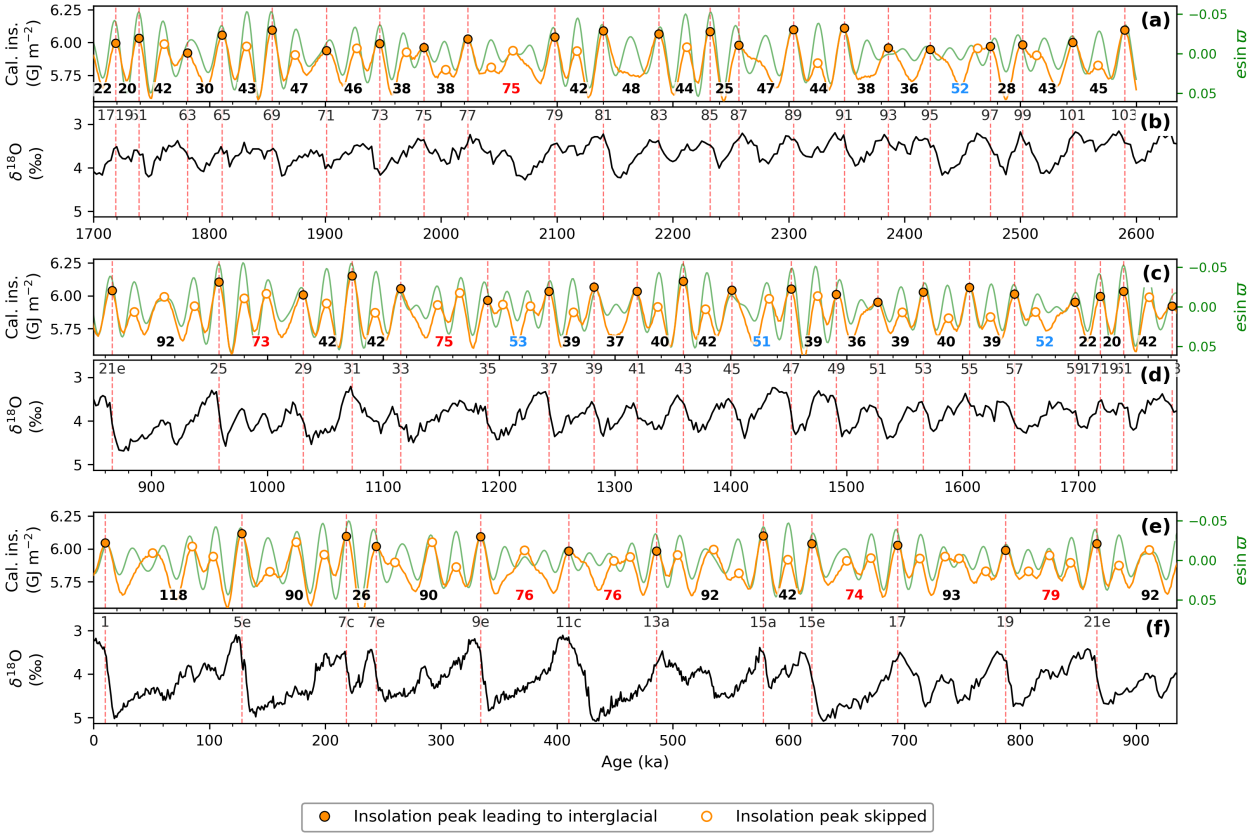


Figure 4: **Selection of insolation peaks and the resulting spacings between interglacial onsets.** Each pair of panels covers a different interval, with a small overlap: (a, b) 1.7–2.6 Ma, (c, d) 0.85–1.75 Ma, and (e, f) 0–0.9 Ma. (a, c, e) Caloric summer half-year insolation at 65°N (orange) (*13*), with climatic precession ($e \sin \varpi$, green). Filled circles mark insolation peaks that led to an interglacial according to the criterion of Tzedakis et al. (2017) (*29*); open circles mark peaks that did not. Numbers give the spacing (kyr) between successive peaks leading to interglacials, with spacings of 50–60 kyr in blue and 70–80 kyr in red. (b, d, f) LR04 benthic δ^{18}O stack (*8*), with the Marine Isotope Stage (MIS) of each corresponding interglacial labeled at the top. Vertical red dashed lines mark the timing of insolation peaks leading to interglacials across all panels.

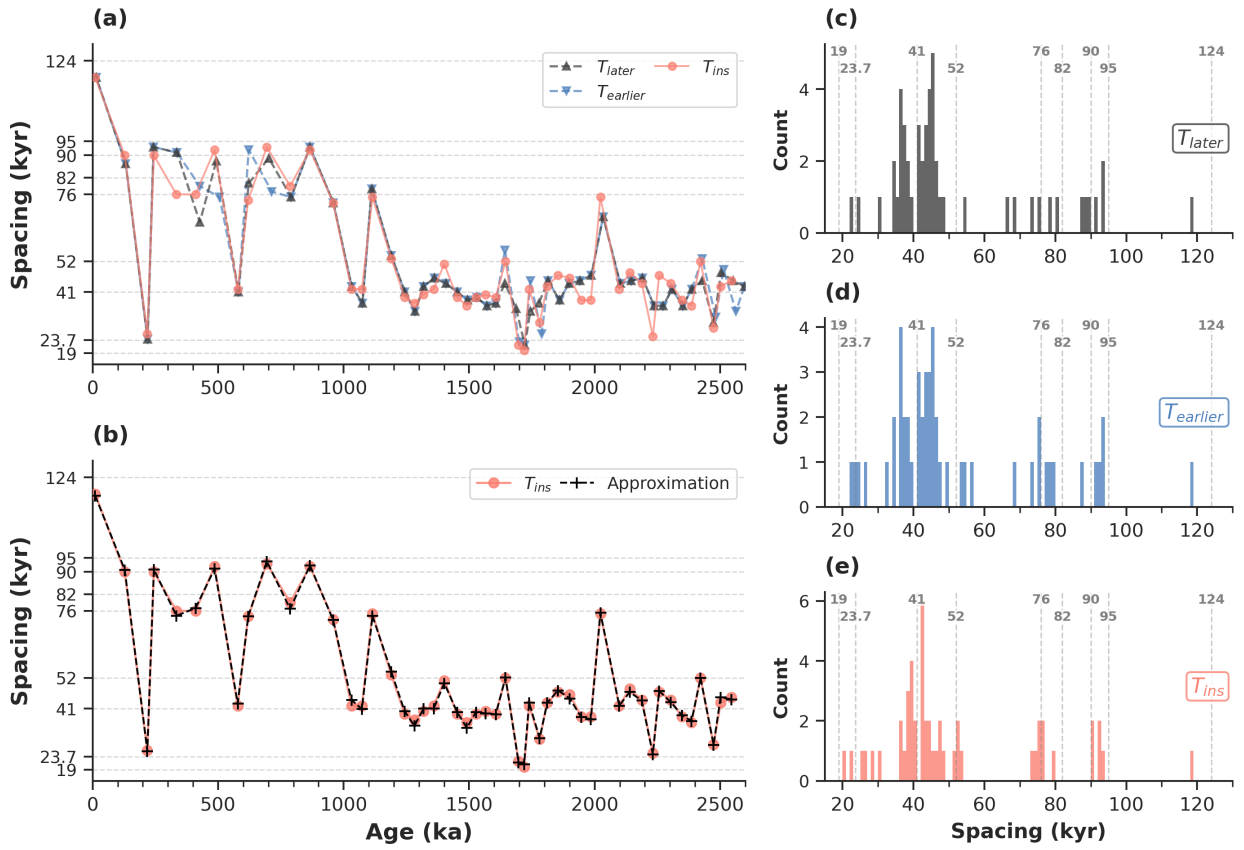


Figure 5: **Comparison of proxy-based deglaciation spacings and insolation-based interglacial spacings.** (a) Time series of spacings over the past 2600 kyr. These intervals are defined by three different metrics: orbital insolation peaks (T_{ins}, salmon circles) and the timing of peak deglaciation rates (T_{later}, dark blue triangles; T_{earlier}, light blue inverted triangles). Horizontal dashed lines indicate key orbital periodicities and the sub-harmonic periodicities discussed in this study (52, 76, and 82 kyr); the line at 90 kyr is drawn for reference. (b) Comparison between the insolation-based spacings (T_{ins}) and their theoretical approximation (black crosses). (c)–(e) Frequency distributions (histograms) of (c) T_{later}, (d) T_{earlier}, and (e) T_{ins}. The insolation-based distribution (e) exhibits distinct clustering around 73–76 kyr and 90–93 kyr; this pattern is partially reflected in the T_{earlier} and T_{later} metrics. All proxy-based metrics align well with T_{ins} ($r \gtrsim 0.95$, RMSE $\lesssim$ 6.5 kyr), justifying the use of T_{ins} for interpreting the spectra.

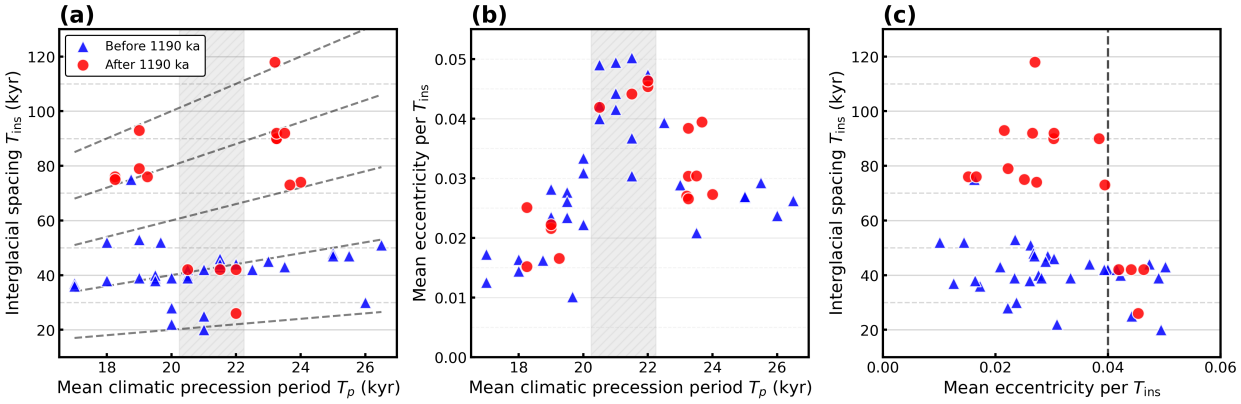


Figure 6: **Orbital constraints on interglacial spacing and the role of eccentricity.** (a) Mean climatic precession period (T_p) versus the insolation-based interglacial spacing (T_{ins}). T_p is defined as the average duration of climatic precession cycles within each interglacial spacing. Dashed lines represent integer multiples of T_p ($T_{\text{ins}} = nT_p$ for $n = 1, \ldots, 5$), showing the clustering of interglacial spacing. (b) T_p versus the mean eccentricity ($\bar{e}$), averaged over the full duration of each interglacial spacing. In (a) and (b), the vertical hatched area (20.25–22.25 kyr) indicates the range of T_p where high mean eccentricity generally precludes glacial cycles longer than 50 kyr. (c) Mean eccentricity versus T_{ins}. The vertical dashed line at $\bar{e} = 0.04$ indicates the threshold above which high eccentricity constrains T_{ins} to values below 50 kyr by facilitating deglaciation. In all panels, blue triangles and red circles represent intervals before and after 1190 ka, respectively. The two exceptional spacings (MIS 95–93 and MIS 93–91), for which T_p is undefined, are excluded (Supplementary text).

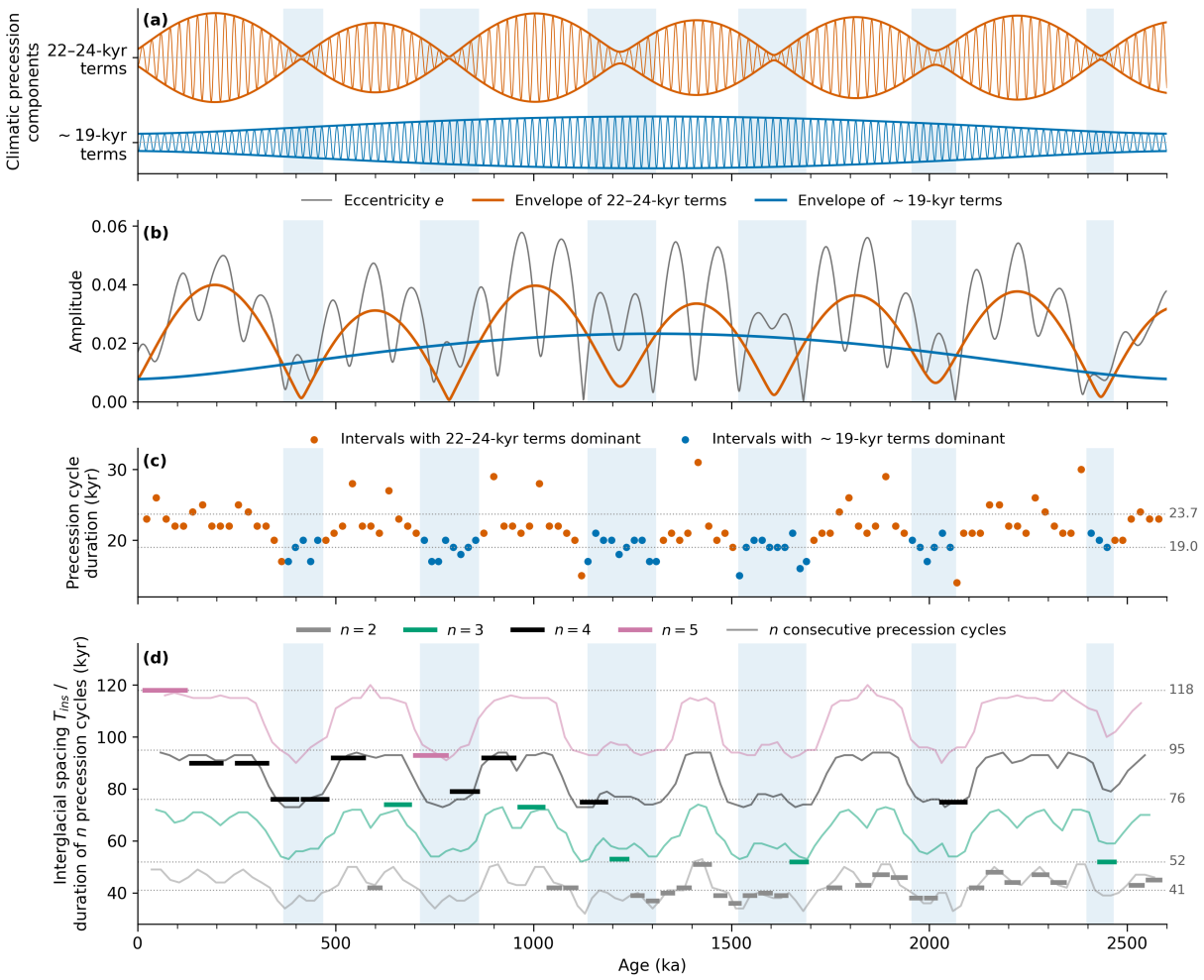


Figure 7: **Timing of the ~52-, ~76-, and ~95-kyr cycles set by the 405-kyr eccentricity cycle.** (a) The two groups of terms of climatic precession obtained by the decomposition described in Materials and Methods: the sum of the 23.7-, 22.4-, and 23.1-kyr terms ($p + g_5$, $p + g_2$, and $p + g_1$; orange, thin line) and the sum of the 19.0- and 19.1-kyr terms ($p + g_4$ and $p + g_3$; blue, thin line), offset vertically, with their amplitude envelopes (thick lines). The beat of the former, with a period of 405 kyr, is the 405-kyr eccentricity cycle. (b) Eccentricity (gray) and the two envelopes of (a). Blue shading marks the intervals in which the ~19-kyr terms dominate, which coincide with minima of the 405-kyr eccentricity cycle. (c) Duration of individual precession cycles, colored by the interval in which each cycle falls, as in (b). (d) Insolation-based interglacial spacings T_{ins} (horizontal bars spanning the two bounding insolation peaks; Table S1), classified by the number of precession cycles n, together with the durations of n consecutive precession cycles (thin lines). Dotted lines mark 41, 52, 76, 95, and 118 kyr.

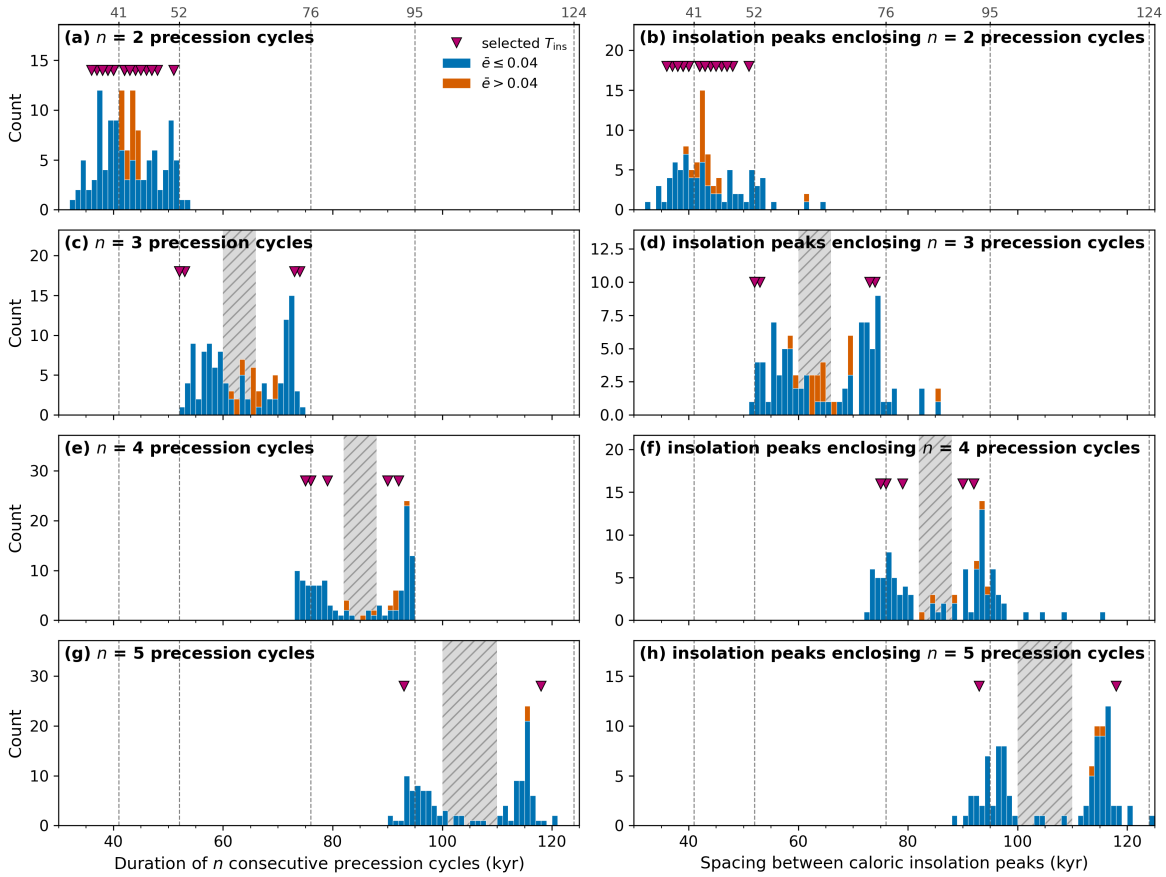


Figure 8: **Durations offered by the astronomical forcing and the constraints that shape interglacial spacings.** Histograms of the durations of n consecutive climatic precession cycles (left) and of the spacings between pairs of caloric summer insolation peaks at 65°N (the 110 peaks of Fig. 4) that enclose n precession cycles (right), over the past 2.6 Myr, for n = 2–5 (rows); all peaks, not only those leading to interglacials, are used. Bars are colored by the mean eccentricity over the window ($\bar{e} \leq 0.04$, blue; $\bar{e} > 0.04$, orange). Gray bands mark the durations that are not realized as interglacial spacings (60–66, 82–88, and 100–110 kyr). Magenta triangles show the interglacial spacings actually selected (Table S1), classified by the number of precession cycles n as in Fig. 6; the two exceptional spacings are excluded. Dotted lines mark 41, 52, 76, 95, and 124 kyr. The durations of four cycles cluster at 73–80 and 89–95 kyr and are rare in the 82–88 kyr band; those of five cycles are rare in the 100–110 kyr band; those of three cycles are common in the 60–66 kyr band but occur preferentially at high eccentricity ($\bar{e} > 0.04$). At such high eccentricity, deglaciation is triggered within one or two precession cycles, so that durations of 60–66 kyr are not realized as interglacial spacings.

References and Notes

1. P. U. Clark, J. D. Shakun, Y. Rosenthal, P. Köhler, P. J. Bartlein, Global and regional temperature change over the past 4.5 million years. *Science* **383** (6685), 884–890 (2024).

2. J. Jouzel, *et al.*, Orbital and millennial Antarctic climate variability over the past 800,000 years. *Science* **317** (5839), 793–796 (2007).

3. E. J. Rohling, *et al.*, Comparison and synthesis of sea-level and deep-sea temperature variations over the past 40 million years. *Reviews of Geophysics* **60** (4), e2022RG000775 (2022).

4. P. U. Clark, *et al.*, Global mean sea level over the past 4.5 million years. *Science* **390** (6770), eadv8389 (2025).

5. D. Lüthi, *et al.*, High-resolution carbon dioxide concentration record 650,000–800,000 years before present. *Nature* **453** (7193), 379–382 (2008).

6. L. Loulergue, *et al.*, Orbital and millennial-scale features of atmospheric CH4 over the past 800,000 years. *Nature* **453** (7193), 383–386 (2008).

7. Y. Zhou, L. E. Lisiecki, S. R. Meyers, T. Lee, C. Lawrence, Global and regional Pleistocene benthic δ 18 O stacks with a comparison of different age modeling strategies. *Geochronology* **8** (1), 85–107 (2026).

8. L. E. Lisiecki, M. E. Raymo, A Pliocene-Pleistocene stack of 57 globally distributed benthic δ18O records. *Paleoceanography* **20** (1), PA1003 (2005).

9. T. D. Herbert, The mid-Pleistocene climate transition. *Annual Review of Earth and Planetary Sciences* **51** (1), 389–418 (2023).

10. C. J. Berends, P. Köhler, L. J. Lourens, R. S. W. van de Wal, On the Cause of the Mid-Pleistocene Transition. *Reviews of Geophysics* **59** (2), e2020RG000727 (2021), e2020RG000727 2020RG000727, doi:https://doi.org/10.1029/2020RG000727.

11. E. L. McClymont, S. M. Sosdian, A. Rosell-Melé, Y. Rosenthal, Pleistocene sea-surface temperature evolution: Early cooling, delayed glacial intensification, and implications for the mid-Pleistocene climate transition. *Earth-Science Reviews* **123**, 173–193 (2013).

12. J. Laskar, *et al.*, A long-term numerical solution for the insolation quantities of the Earth. *Astronomy & Astrophysics* **428** (1), 261–285 (2004).

13. M. Crucifix, Palinsol: insolation for palaeoclimate studies, R package version 0.93 (2016).

14. D. Paillard, Glacial cycles: toward a new paradigm. *Reviews of Geophysics* **39** (3), 325–346 (2001).

15. J. D. Hays, J. Imbrie, N. J. Shackleton, Variations in the Earth's Orbit: Pacemaker of the Ice Ages. *Science* **194** (4270), 1121–1132 (1976).

16. A. Berger, Support for the astronomical theory of climatic change. *Nature* **269** (5623), 44–45 (1977).

17. A. Berger, Long-term variations of daily insolation and Quaternary climatic changes. *Journal of Atmospheric Sciences* **35** (12), 2362–2367 (1978).

18. M. Raymo, The timing of major climate terminations. *Paleoceanography* **12** (4), 577–585 (1997).

19. A. J. Ridgwell, A. J. Watson, M. E. Raymo, Is the spectral signature of the 100 kyr glacial cycle consistent with a Milankovitch origin? *Paleoceanography* **14** (4), 437–440 (1999).

20. K. H. Nyman, P. D. Ditlevsen, The middle Pleistocene transition by frequency locking and slow ramping of internal period. *Climate Dynamics* **53** (5), 3023–3038 (2019).

21. T. Blackburn, S. Kodama, G. Piccione, Eccentricity paces late Pleistocene glaciations. *Geophysical Research Letters* **51** (12), e2024GL108751 (2024).

22. P. Huybers, C. Wunsch, Obliquity pacing of the late Pleistocene glacial terminations. *Nature* **434** (7032), 491–494 (2005).

23. P. Bajo, *et al.*, Persistent influence of obliquity on ice age terminations since the Middle Pleistocene transition. *Science* **367** (6483), 1235–1239 (2020).

24. A. Abe-Ouchi, *et al.*, Insolation-driven 100,000-year glacial cycles and hysteresis of ice-sheet volume. *Nature* **500** (7461), 190–193 (2013).

25. H. Cheng, *et al.*, The Asian monsoon over the past 640,000 years and ice age terminations. *Nature* **534** (7609), 640–646 (2016).

26. S. Barker, *et al.*, Persistent influence of precession on northern ice sheet variability since the early Pleistocene. *Science* **376** (6596), 961–967 (2022).

27. B. Hobart, L. E. Lisiecki, D. Rand, T. Lee, C. E. Lawrence, Late Pleistocene 100-kyr glacial cycles paced by precession forcing of summer insolation. *Nature Geoscience* **16** (8), 717–722 (2023).

28. P. Huybers, Combined obliquity and precession pacing of late Pleistocene deglaciations. *Nature* **480** (7376), 229–232 (2011).

29. P. Tzedakis, M. Crucifix, T. Mitsui, E. W. Wolff, A simple rule to determine which insolation cycles lead to interglacials. *Nature* **542** (7642), 427–432 (2017).

30. T. Mitsui, M. Willeit, N. Boers, Synchronization phenomena observed in glacial-interglacial cycles simulated in an Earth system model of intermediate complexity. *Earth System Dynamics* **2023**, 1277–1294 (2023), doi:10.5194/esd-14-1277-2023, `https://doi.org/10.5194/esd-14-1277-2023`.

31. T. Mitsui, P. C. Tzedakis, E. W. Wolff, Insolation evolution and ice volume legacies determine interglacial and glacial intensity. *Climate of the Past* **18** (9), 1983–1996 (2022).

32. S. Barker, L. E. Lisiecki, G. Knorr, S. Nuber, P. C. Tzedakis, Distinct roles for precession, obliquity, and eccentricity in Pleistocene 100-kyr glacial cycles. *Science* **387** (6737), eadp3491 (2025).

33. G. Foster, Time series analysis by projection. I. Statistical properties of Fourier analysis. *Astronomical Journal v. 111, p. 541* **111**, 541 (1996).

34. J. W. Kirchner, C. Neal, Universal fractal scaling in stream chemistry and its implications for solute transport and water quality trend detection. *Proceedings of the National Academy of Sciences* **110** (30), 12213–12218 (2013).

699 35. D. Khider, *et al.*, Pyleoclim: Paleoclimate timeseries analysis and visualization with Python.
700 *Paleoceanography and Paleoclimatology* **37** (10), e2022PA004509 (2022).

701 36. P. Huybers, Glacial variability over the last two million years: an extended depth-derived
702 agemodel, continuous obliquity pacing, and the Pleistocene progression. *Quaternary Science*
703 *Reviews* **26** (1-2), 37–55 (2007).

704 37. L. E. Lisiecki, Links between eccentricity forcing and the 100,000-year glacial cycle. *Nature*
705 *Geoscience* **3** (5), 349–352 (2010).

706 38. S. R. Meyers, The evaluation of eccentricity-related amplitude modulation and bundling in
707 paleoclimate data: An inverse approach for astrochronologic testing and time scale optimization.
708 *Paleoceanography* **30** (12), 1625–1640 (2015).

709 39. S. R. Meyers, Cyclostratigraphy and the problem of astrochronologic testing. *Earth-Science*
710 *Reviews* **190**, 190–223 (2019).

711 40. M. Willeit, A. Ganopolski, R. Calov, V. Brovkin, Mid-Pleistocene transition in glacial cycles
712 explained by declining CO2 and regolith removal. *Science Advances* **5** (4), eaav7337 (2019).

713 41. F. Pollak, *et al.*, Simulating global ice volume across the Mid-Pleistocene Transition with a
714 ramp-like increase in the deglaciation threshold. *Climate of the Past* **22** (3), 675–688 (2026).

715 42. P. R. Liautaud, D. A. Hodell, P. J. Huybers, Detection of significant climatic precession
716 variability in early Pleistocene glacial cycles. *Earth and Planetary Science Letters* **536**, 116137
717 (2020).

718 43. M. Mudelsee, K. Stattegger, Exploring the structure of the mid-Pleistocene revolution with
719 advanced methods of time-series analysis. *Geologische Rundschau* **86** (2), 499–511 (1997).

720 44. P. U. Clark, *et al.*, The middle Pleistocene transition: characteristics, mechanisms, and impli-
721 cations for long-term changes in atmospheric pCO2. *Quaternary Science Reviews* **25** (23-24),
722 3150–3184 (2006).

723 45. L. E. Lisiecki, M. E. Raymo, Plio–Pleistocene climate evolution: trends and transitions in
724 glacial cycle dynamics. *Quaternary Science Reviews* **26** (1-2), 56–69 (2007).

46. P. Huybers, C. Wunsch, A depth-derived Pleistocene age model: Uncertainty estimates, sedimentation variability, and nonlinear climate change. *Paleoceanography* **19** (1), PA1028 (2004).

47. S. Ahn, D. Khider, L. E. Lisiecki, C. E. Lawrence, A probabilistic Pliocene–Pleistocene stack of benthic δ18O using a profile hidden Markov model. *Dynamics and Statistics of the Climate System* **2** (1), dzx002 (2017).

48. H. Le Treut, M. Ghil, Orbital forcing, climatic interactions, and glaciation cycles. *Journal of Geophysical Research: Oceans* **88** (C9), 5167–5190 (1983).

49. E. K. Thomas, *et al.*, Heterodynes dominate precipitation isotopes in the East Asian monsoon region, reflecting interaction of multiple climate factors. *Earth and Planetary Science Letters* **455**, 196–206 (2016), doi:10.1016/j.epsl.2016.09.049.

50. K. Kawamura, *et al.*, Northern Hemisphere forcing of climatic cycles in Antarctica over the past 360,000 years. *Nature* **448** (7156), 912–916 (2007), doi:10.1038/nature06015.

51. P. Huybers, O. Aharonson, Orbital tuning, eccentricity, and the frequency modulation of climatic precession. *Paleoceanography* **25** (4), PA4228 (2010).

52. Y. Watanabe, *et al.*, Astronomical forcing shaped the timing of early Pleistocene glacial cycles. *Communications Earth & Environment* **4** (1), 113 (2023).

53. D. Liebrand, A. de Bakker, Bispectra of climate cycles show how ice ages are fuelled. *Climate of the Past* **15** (6), 1959–1983 (2019).

54. E. Tziperman, M. E. Raymo, P. Huybers, C. Wunsch, Consequences of pacing the Pleistocene 100 kyr ice ages by nonlinear phase locking to Milankovitch forcing. *Paleoceanography* **21** (4), PA4206 (2006).

55. T. Mitsui, P. Ditlevsen, N. Boers, M. Crucifix, 100 kyr ice age cycles as a timescale-matching problem. *Earth System Dynamics* **16** (5), 1569–1584 (2025).

56. M. Y. Verbitsky, D. Volobuev, Milankovitch theory "as an initial value problem": Implications of the long memory of ice advection. *Earth System Dynamics* **16** (6), 1989–2002 (2025).

57. P. Huybers, Pleistocene glacial variability as a chaotic response to obliquity forcing. *Climate of the Past* **5** (3), 481–488 (2009), doi:10.5194/cp-5-481-2009.

58. E. W. Bolton, K. A. Maasch, J. M. Lilly, A wavelet analysis of Plio-Pleistocene climate indicators: A new view of periodicity evolution. *Geophysical Research Letters* **22** (20), 2753–2756 (1995).

59. J. A. Rial, Pacemaking the ice ages by frequency modulation of Earth's orbital eccentricity. *Science* **285** (5427), 564–568 (1999).

60. M. Y. Verbitsky, M. Crucifix, D. M. Volobuev, ESD Ideas: Propagation of high-frequency forcing to ice age dynamics. *Earth System Dynamics* **10** (2), 257–260 (2019).

61. S. C. Clemens, *et al.*, Precession-band variance missing from East Asian monsoon runoff. *Nature Communications* **9**, 3364 (2018), doi:10.1038/s41467-018-05814-0.

62. M. E. Raymo, K. H. Nisancioglu, The 41 kyr world: Milankovitch's other unsolved mystery. *Paleoceanography* **18** (1), 1011 (2003).

63. S. C. Clemens, W. L. Prell, Y. Sun, Orbital-scale timing and mechanisms driving Late Pleistocene Indo-Asian summer monsoons: Reinterpreting cave speleothem δ^{18}O. *Paleoceanography* **25**, PA4207 (2010), doi:10.1029/2010PA001926.

64. S. T. Kodama, T. Blackburn, Eccentricity controls the magnitude and periodicity of Pleistocene glacial cycles. *Paleoceanography and Paleoclimatology* **41** (3), e2026PA005420 (2026).

65. D. M. Sigman, *et al.*, The Southern Ocean during the ice ages: A review of the Antarctic surface isolation hypothesis, with comparison to the North Pacific. *Quaternary Science Reviews* **254**, 106732 (2021), doi:10.1016/j.quascirev.2020.106732.

66. A. Martínez-Garcia, *et al.*, Southern Ocean dust–climate coupling over the past four million years. *Nature* **476** (7360), 312–315 (2011).

67. A. P. Hasenfratz, *et al.*, The residence time of Southern Ocean surface waters and the 100,000-year ice age cycle. *Science* **363**, 1080–1084 (2019), doi:10.1126/science.aat7067.

68. B. Hönisch, N. G. Hemming, D. Archer, M. Siddall, J. F. McManus, Atmospheric carbon dioxide concentration across the mid-Pleistocene transition. *Science* **324** (5934), 1551–1554 (2009).

69. T. B. Chalk, *et al.*, Causes of ice age intensification across the Mid-Pleistocene Transition. *Proceedings of the National Academy of Sciences* **114** (50), 13114–13119 (2017).

70. K. A. Dyez, B. Hönisch, A. C. Ravelo, Early Pleistocene obliquity-scale pCO_2 variability at ~1.5 million years ago. *Paleoceanography and Paleoclimatology* **33**, 1270–1291 (2018), doi:10.1029/2018PA003349.

71. S. K. Hines, *et al.*, Revisiting the mid-Pleistocene transition ocean circulation crisis. *Science* **386** (6722), 681–686 (2024).

72. C. Basak, *et al.*, Southern Hemisphere initiation of the mid-Pleistocene transition. *Science Advances* **12** (10), eaea6811 (2026).

73. Z. An, *et al.*, Mid-Pleistocene climate transition triggered by Antarctic Ice Sheet growth. *Science* **385** (6708), 560–565 (2024).

74. P. U. Clark, D. Pollard, Origin of the middle Pleistocene transition by ice sheet erosion of regolith. *Paleoceanography* **13** (1), 1–9 (1998).

75. M. Yehudai, *et al.*, Evidence for a Northern Hemispheric trigger of the 100,000-y glacial cyclicity. *Proceedings of the National Academy of Sciences* **118** (46), e2020260118 (2021).

76. H. Elderfield, *et al.*, Evolution of ocean temperature and ice volume through the mid-Pleistocene climate transition. *Science* **337** (6095), 704–709 (2012).

77. S. Shackleton, *et al.*, Global ocean heat content over the past 3 million years. *Nature* **651**, 653–657 (2026), doi:10.1038/s41586-026-10116-3.

78. J. Imbrie, J. Z. Imbrie, Modeling the climatic response to orbital variations. *Science* **207** (4434), 943–953 (1980).

79. P. Bloomfield, *Fourier analysis of time series: an introduction* (John Wiley & Sons) (2004).

80. D. J. Thomson, Spectrum estimation and harmonic analysis. *Proceedings of the IEEE* **70** (9), 1055–1096 (1982).

81. M. Schulz, M. Mudelsee, REDFIT: estimating red-noise spectra directly from unevenly spaced paleoclimatic time series. *Computers & Geosciences* **28** (3), 421–426 (2002).

82. N. R. Lomb, Least-squares frequency analysis of unequally spaced data. *Astrophysics and space science* **39** (2), 447–462 (1976).

83. J. D. Scargle, Studies in astronomical time series analysis. II-Statistical aspects of spectral analysis of unevenly spaced data. *The Astrophysical Journal* **263**, 835–853 (1982).

84. Z. Wu, N. E. Huang, S. R. Long, C.-K. Peng, On the trend, detrending, and variability of nonlinear and nonstationary time series. *Proceedings of the National Academy of Sciences* **104** (38), 14889–14894 (2007).

85. F. Zhu, *et al.*, Climate models can correctly simulate the continuum of global-average temperature variability. *Proceedings of the National Academy of Sciences* **116** (18), 8728–8733 (2019).

86. M. Milankovitch, Kanon der Erdbestrahlung und seine Anwendung auf das Eiszeitenproblem. *Königlich Serbische Akademie, Belgrad, Special Publication* **133** (1941).

87. K. H. Nisancioglu, Plio-pleistocene glacial cycles and milankovitch variability. *Elements of Physical Oceanography: A derivative of the Encyclopedia of Ocean Sciences* p. 344 (2009).

Acknowledgments

The author thanks Dr. Polychronis Tzedakis and Dr. Eric W. Wolff for insightful communications that inspired this work, Dr. Masanobu Yamamoto for drawing the author's attention to heterodyne periods in monsoon records, Dr. Ryuji Tada for encouraging the author to explore when the ~76-kyr cycles occur, and the three anonymous referees for their constructive comments, which substantially improved the manuscript.

Funding: The author was supported in part by JSPS KAKENHI Grant Numbers JP26K00011 and JP25K07942.

Competing interests: The author declares no competing interests.

Data, code, and materials availability: All data needed to evaluate the conclusions in the paper are present in the paper and/or the Supplementary Materials. Data S1 (`Data_S1_formula.xlsx`, the electronic version of Table S1) is archived at Zenodo (`https://doi.org/10.5281/zenodo.19534113`). All proxy records and model outputs analyzed here are previously published and publicly available from the original sources cited in the main text and Supplementary Materials. The analysis code (Python notebooks using `Pyleoclim`) used to produce the figures is available from the author upon request and will be archived in the same Zenodo repository upon acceptance. This study did not generate new materials.

Supplementary materials

Supplementary Text

Figs. S1 to S22

Table S1

Supplementary Materials for

Beyond the 100-kyr and 41-kyr dichotomy: ~76- and ~52-kyr signals and forbidden periodicities in Quaternary glacial cycles

Takahito Mitsui*

*Corresponding author. Email: takahito321@gmail.com

This PDF file includes:

Supplementary Text

Figs. S1 to S22

Table S1

Other Supplementary Materials for this manuscript:

Data S1 (`Data_S1_formula.xlsx`): electronic version of Table S1, available at `https://doi.org/10.5281/zenodo.19534113`

Supplementary text

Derivation of the approximation formulae of interglacial spacings

Following Tzedakis et al. (2017) (*29*), we assume that each interglacial onset can be linked with a specific peak in the caloric summer half-year insolation at 65°N (*13, 86*). Thus, the insolation-based interglacial spacings (T_{ins}) are defined between successive caloric summer insolation peaks that ultimately led to each interglacial (*29*) (Figs. S14a–S16a). Of the 110 insolation peaks of the past 2.6 Myr, the 51 that led to interglacials almost all (98%) occurred when obliquity was above its mean, illustrating the role of obliquity in selecting the peaks. Here we derive approximate formulae for T_{ins} of each glacial cycle based on local information on climatic precession and obliquity (*12*) (Figs. S18–S21).

The caloric summer insolation, especially at 65°N, is well approximated by a superposition of standardized indices of climatic precession and obliquity, which contribute with similar magnitude (*86, 87*). Since the climatic precession oscillates more rapidly than obliquity, the insolation peak closest to the deglaciation isotopic change is more tightly linked with a climatic precession peak (minimum). Indeed, the link between the length of glacial cycles and the durations of astronomical cycles—particularly precession—has been noted in various studies (*21, 24, 25, 27*). On the other hand, the duration of climatic precession cycles varies widely (between 14 and 31 kyr) when eccentricity is low, whereas it remains relatively stable near 22 kyr when eccentricity is high (Fig. S17) (*21, 51*). Building on this, we here derive finer relationships between T_{ins} and the varying durations of precession and obliquity cycles.

For each glacial cycle, we approximate the local variations in the caloric summer insolation as $f(t) = A_p \cos(\omega_p t + \varphi_p) + A_o \cos(\omega_o t + \varphi_o)$, accounting for the respective positive contributions of climatic precession and obliquity to the insolation. Here, $A_{p,o}$ are the local-mean amplitudes, $\omega_{p,o}$ are the angular frequencies (corresponding to local-mean periods $T_{p,o}$), and $\varphi_{p,o}$ are the local phases of climatic precession and obliquity cycles. Note that the maxima of $A_p \cos(\omega_p t + \varphi_p)$ correspond to the minima of the climatic precession cycles, as precession minima contribute to maximal insolation. Then, we can derive analytical expressions for T_{ins}. A complete correspondence between individual glacial cycles and their respective formulae is provided in Table S1.

Formula types 2a, 3a, 4a, and 5a. When the peaks of climatic precession and obliquity nearly

coincide and collectively lead to an interglacial, we define this peak time as $t = 0$ by setting $\varphi_p = \varphi_o = 0$ (Fig. S22a). If the spacing $T_{\rm ins}$ between the peak at $t = 0$ and the next peak leading to an interglacial is close to the n-th multiple of the local-mean precession period T_p, it can be expressed as $T_{\rm ins} = nT_p + \delta$, where the small shift δ reflects the phase modulation by obliquity. By linearizing the peak condition $f'(nT_p + \delta) = 0$ as $f'(nT_p + \delta) \approx f'(nT_p) + f''(nT_p)\delta = 0$, we obtain approximation formulae for $T_{\rm ins}$ ($n = 2,\ 3,\ 4,\ 5$), called type-a:

$$T_{\rm ins} \approx nT_p - \frac{A_o\omega_o \sin(n\omega_o T_p)}{A_p\omega_p^2 + A_o\omega_o^2 \cos(n\omega_o T_p)}.$$

An example of type-a is the ~76-kyr spacing between interglacials MIS 11c and MIS 9e (Fig. S18), where the insolation peaks are separated by four precession cycles ($n = 4$) with a local-mean period of $T_p = 18.25$ kyr, and the local-mean obliquity period is $T_o = 41.5$ kyr. The type-a formula then predicts $T_{\rm ins} = 74.3$ kyr. This value is closer to the actual value of 76 kyr than the simple multiple of precession, $nT_p = 73$ kyr, obtained without the shift $\delta = 1.3$ kyr.

Formula types 1b and 3b. The second case occurs when a glacial cycle spans roughly one or three precession cycles (i.e., $n = 1$ or 3), with the insolation locally approximated as $f(t) = -A_p \cos(\omega_p t) - A_o \cos(\omega_o t)$ over the interval $-\frac{n}{2}T_p \lesssim t \lesssim \frac{n}{2}T_p$ (corresponding to $\varphi_p = \varphi_o = \pi$). For this case, we assume that deglaciations occur at $t = \pm(\frac{n}{2}T_p + \delta)$, with δ being a small obliquity-induced shift. By linearizing the peak condition $f'(\frac{n}{2}T_p + \delta) \approx f'(\frac{n}{2}T_p) + f''(\frac{n}{2}T_p)\delta = 0$, we obtain approximation formulae for $T_{\rm ins}$ ($n = 1,\ 3$), called type-1b or 3b:

$$T_{\rm ins} \approx nT_p + \frac{2A_o\omega_o \sin\left(\frac{n}{2}\omega_o T_p\right)}{A_p\omega_p^2 - A_o\omega_o^2 \cos\left(\frac{n}{2}\omega_o T_p\right)}.$$

An example of type-3b is the spacing between interglacials MIS 37 and MIS 35 (Fig. S19), where the insolation peaks are separated by three precession cycles ($n = 3$) with a local-mean period of $T_p = 19$ kyr, and the local-mean obliquity period is $T_o = 39$ kyr. Then, the type-3b formula predicts $T_{\rm ins} = 54.2$ kyr. This value is closer to the actual value of 53 kyr than the simple multiple of precession, $nT_p = 57$ kyr, obtained without the shift $\delta = -2.8$ kyr.

Formula type 2b. Consider a case where a glacial cycle spans approximately two precession cycles, in which the central precession peak is counteracted by an obliquity minimum, while the outer precession peaks are enhanced by adjacent obliquity maxima. This situation is approximated as $f(t) = A_p \cos(\omega_p t) - A_o \cos(\omega_o t)$ over the interval $-T_p \lesssim t \lesssim T_p$ (corresponding to $\varphi_p = 0$ and

$\varphi_o = \pi$). In a similar manner to the derivation of the formulae type-1b and 3b, T_{ins} is given by the formula called type-2b:

$$T_{\mathrm{ins}} \approx 2T_p + \frac{2A_o\omega_o \sin\left(\omega_o T_p\right)}{A_p\omega_p^2 - A_o\omega_o^2 \cos\left(\omega_o T_p\right)}.$$

Formula type 4b. Consider a case where a glacial cycle spans approximately four precession cycles, in which the central precession peak is enhanced by an obliquity maximum, while the outer precession peaks are also enhanced by adjacent obliquity maxima. This situation is approximated as $f(t) = A_p \cos(\omega_p t) + A_o \cos(\omega_o t)$ over the interval $-2T_p \lesssim t \lesssim 2T_p$ (corresponding to $\varphi_p = \varphi_o = 0$). In a similar manner to the derivation of the formulae type-2b, T_{ins} is given by the formula called type-4b:

$$T_{\mathrm{ins}} \approx 4T_p - \frac{2A_o\omega_o \sin\left(2\omega_o T_p\right)}{A_p\omega_p^2 + A_o\omega_o^2 \cos\left(2\omega_o T_p\right)}.$$

Formula types 1c and 2c. Consider a case where a glacial cycle spans roughly one or two precession cycles ($n = 1$ or 2), with the insolation locally approximated as $f(t) = A_p \cos(\omega_p t) - A_o \sin(\omega_o t)$ over the interval $0 \le t \lesssim nT_p$ (corresponding to $\varphi_p = 0$ and $\varphi_o = \frac{\pi}{2}$). In this case, the deglaciations occur at $t = 0$ and $t = nT_p + \delta$, where δ is a small shift. By linearizing the peak condition $f'(nT_p + \delta) \approx f'(nT_p) + f''(nT_p)\delta = 0$, we obtain approximation formulae for T_{ins} ($n = 1,\ 2$), called type-1c or 2c:

$$T_{\mathrm{ins}} \approx nT_p - \frac{A_o\omega_o \cos\left(n\omega_o T_p\right)}{A_p\omega_p^2 - A_o\omega_o^2 \sin\left(n\omega_o T_p\right)}.$$

Formula type 2d. Consider a case where a glacial cycle spans roughly two precession cycles, with the insolation locally approximated as $f(t) = A_p \cos(\omega_p t) + A_o \sin(\omega_o t)$ over the interval $0 \le t \lesssim 2T_p$ (corresponding to $\varphi_p = 0$ and $\varphi_o = -\frac{\pi}{2}$). In this case, the deglaciations occur at $t = 0$ and $t = 2T_p + \delta$, where δ is a small shift. By linearizing the peak condition $f'(2T_p + \delta) \approx f'(2T_p) + f''(2T_p)\delta = 0$, we obtain the approximation formula for T_{ins}, called type-2d:

$$T_{\mathrm{ins}} \approx 2T_p + \frac{A_o\omega_o \cos\left(2\omega_o T_p\right)}{A_p\omega_p^2 + A_o\omega_o^2 \sin\left(2\omega_o T_p\right)}.$$

Formula type pp. In this case, the interglacial spacing is primarily determined by the spacing between precession peaks; while obliquity cycles may shift the timing of both deglaciations, they do so by the same amount, leaving the net spacing almost unchanged. Therefore,

$$T_{\mathrm{ins}} \approx nT_p.$$

Choice of amplitude $A_{p,o}$. Climatic precession and obliquity contribute nearly equally to the total variance in the caloric summer insolation at 65°N (Materials and Methods). For simplicity, we therefore set $A_p = A_o = 1$, except for two cycles: those from MIS 99 to 97 and from MIS 97 to 95 fall at low eccentricity (low precession amplitude) and high obliquity amplitude (Fig. S21). Assessing the variances locally, we took $A_o/A_p = 2.5$ and 3 for the two cycles, respectively.

Two exceptions. The spacings MIS 95–93 and MIS 93–91 represent epochs during which eccentricity remains near zero (Fig. S21). The aforementioned formulae are inapplicable to these events because deglaciation coincides with the obliquity maximum at 2386 ka, where eccentricity is virtually zero. For these cases, we adopt simplified estimates for T_{ins}. The MIS 95–93 interval is assumed to be initiated by an insolation peak occurring midway between the obliquity maximum at 2426 ka and the precession minimum at 2419 ka, and is finalized by the obliquity maximum at 2386 ka. Consequently, the spacing is estimated as $(2426 + 2419)/2 - 2386 = 36.5$ kyr. Similarly, the MIS 93–91 interval is initiated by the 2386-ka obliquity maximum and finalized by an insolation peak midway between the obliquity maximum at 2348 ka and the precession minimum at 2347 ka. The spacing is thus estimated as $2386 - (2348 + 2347)/2 = 38.5$ kyr.

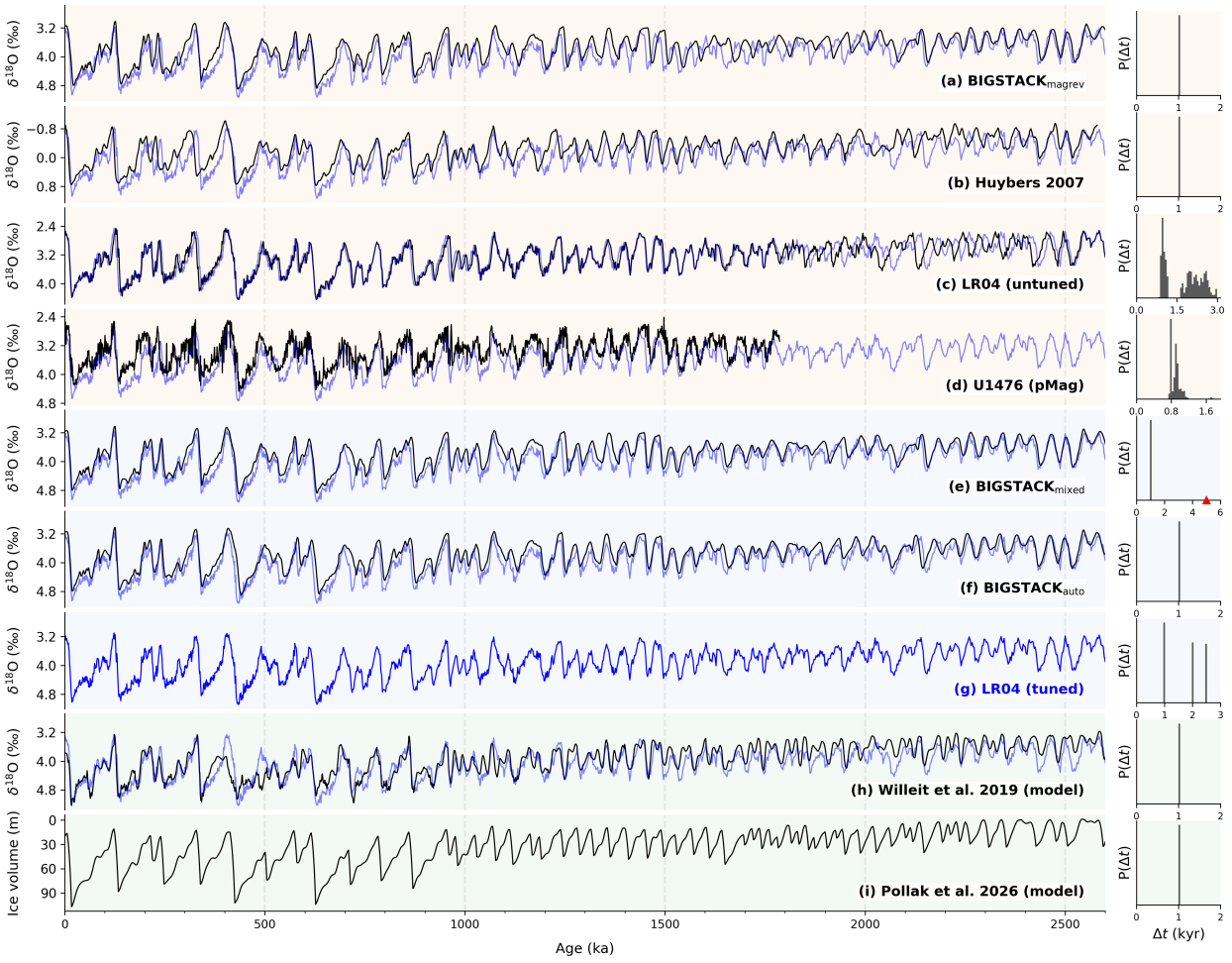


Figure S1: **Benthic δ^{18}O records and model outputs analyzed in this study, and their sampling intervals.** The full caption is given on the following page.

Figure S1 (continued). Panels are grouped and ordered as in Figs. 2 and 3: (a)–(d) tuning-free or minimally tuned records, (e)–(g) orbitally tuned records, (h)–(i) model outputs, distinguished by background shading. Except in (g) and (i), the tuned LR04 stack is shown as a blue background reference, vertically shifted to match the mean of each target series (black). The small square to the right of each panel shows the distribution $P(\Delta t)$ of the sampling interval Δt over the analyzed window 0–2600 kyr, computed from the age model of each series. The Δt axis is scaled individually for each panel. Series with a single sampling interval appear as a single line, the stepwise series (g) as three lines, and the irregularly spaced series (c, d) as a broad distribution reflecting their age models. (a) $\text{BIGSTACK}_{\text{magrev}}$ (*7*). (b) The depth-derived stack of Huybers (2007) (*36*). (c) The tuning-free LR04 stack (*37*). (d) IODP Site U1476 on a paleomagnetic age model (*26*); spans only the last 1786.542 kyr. (e) $\text{BIGSTACK}_{\text{mixed}}$ (*7*); the red triangle marks a single interval of $\Delta t = 5$ kyr (645–650 ka), which is too rare to be visible in the histogram. (f) $\text{BIGSTACK}_{\text{auto}}$ (*7*). (g) The tuned LR04 stack (*8*), shown in blue; sampled at 1, 2, and 2.5 kyr over 0–600, 600–1500, and 1500–2600 kyr, respectively. (h) Simulated benthic δ^{18}O of Willeit et al. (2019) (*40*). (i) Simulated global ice volume of Pollak et al. (2026) (*41*); no LR04 reference, as the quantity differs.

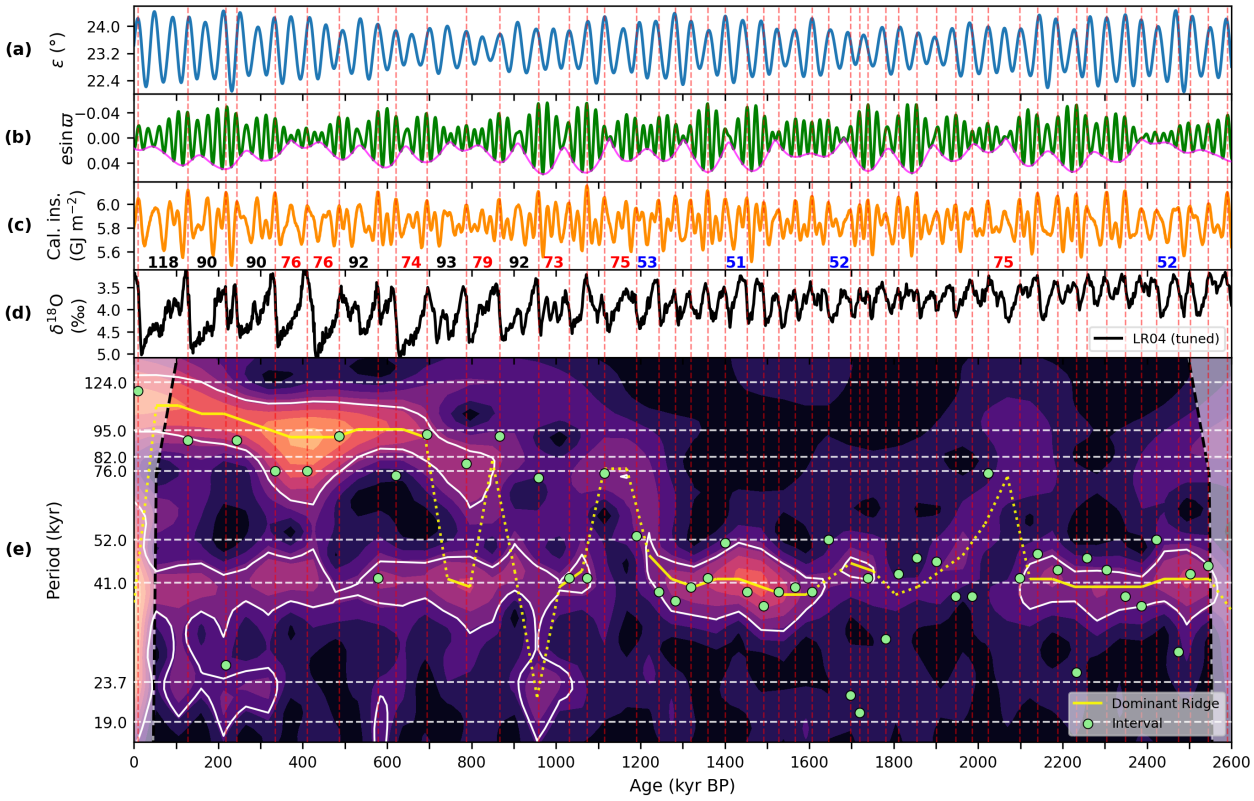


Figure S2: **Time-series and wavelet analyses of the orbitally tuned LR04 benthic δ^{18}O stack record (*8*), aligned with astronomical forcing (*12*) over the last 2.6 Myr.** (a) Obliquity (ε). (b) Climatic precession ($e \sin \varpi$, green) shown with its eccentricity envelope (e, magenta). (c) Caloric summer half-year insolation at 65°N (*13*). (d) The orbitally tuned LR04 benthic δ^{18}O stack record (*8*). (e) Wavelet power scalogram of the δ^{18}O record. The yellow line indicates the ridge of maximum wavelet power, drawn solid or dotted as in Fig. 1e. Areas enclosed by white dashed lines indicate power significant at the 95% confidence level against an AR(1) benchmark. Horizontal dashed lines denote major astronomical periodicities, including the 76-kyr and 52-kyr scales discussed in this study.

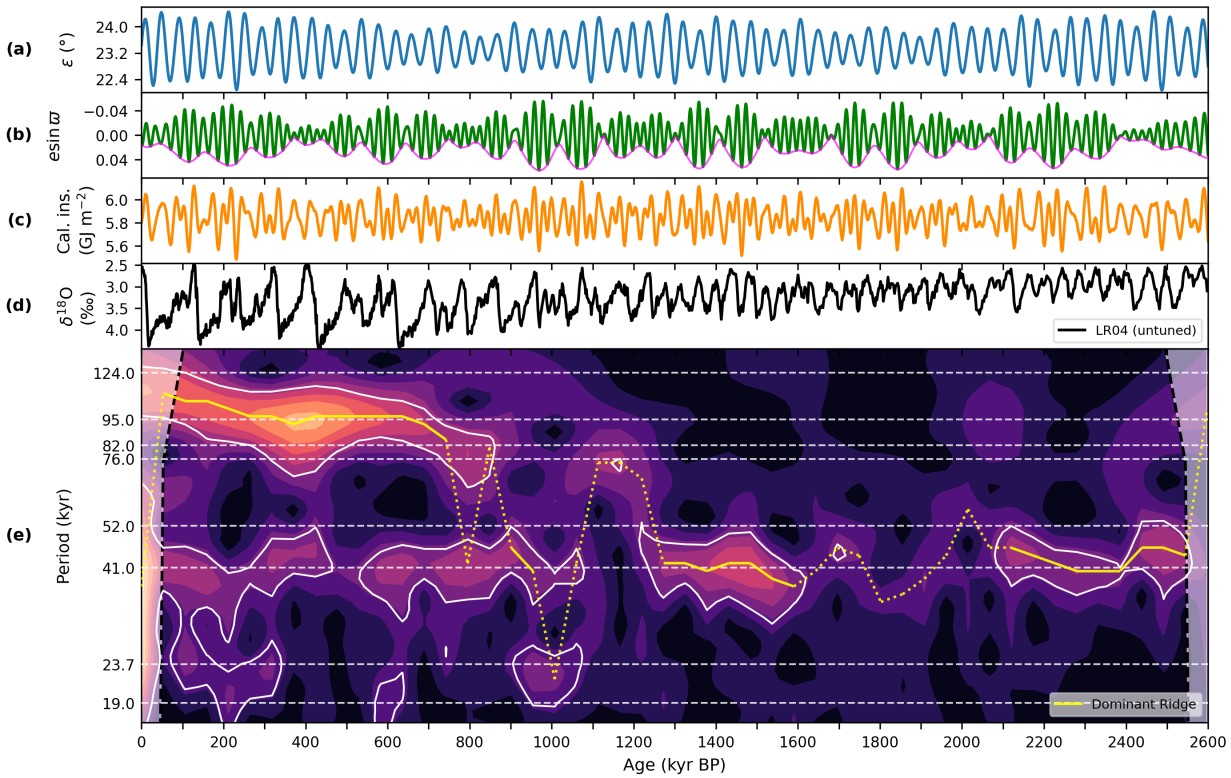


Figure S3: **Time-series and wavelet analyses of the LR04 benthic δ^{18}O stack record free from orbital tuning (*37*), aligned with astronomical forcing (*12*) over the last 2.6 Myr.** (a) Obliquity (ε). (b) Climatic precession ($e \sin \varpi$, green) shown with its eccentricity envelope (e, magenta). (c) Caloric summer half-year insolation at 65°N (*13*). (d) The LR04 benthic δ^{18}O stack record without orbital tuning (*37*). (e) Wavelet power scalogram of the δ^{18}O record. The yellow line indicates the ridge of maximum wavelet power, drawn solid or dotted as in Fig. 1e. Areas enclosed by white dashed lines indicate power significant at the 95% confidence level against an AR(1) benchmark. Horizontal dashed lines denote major astronomical periodicities, including the 76-kyr and 52-kyr scales discussed in this study.

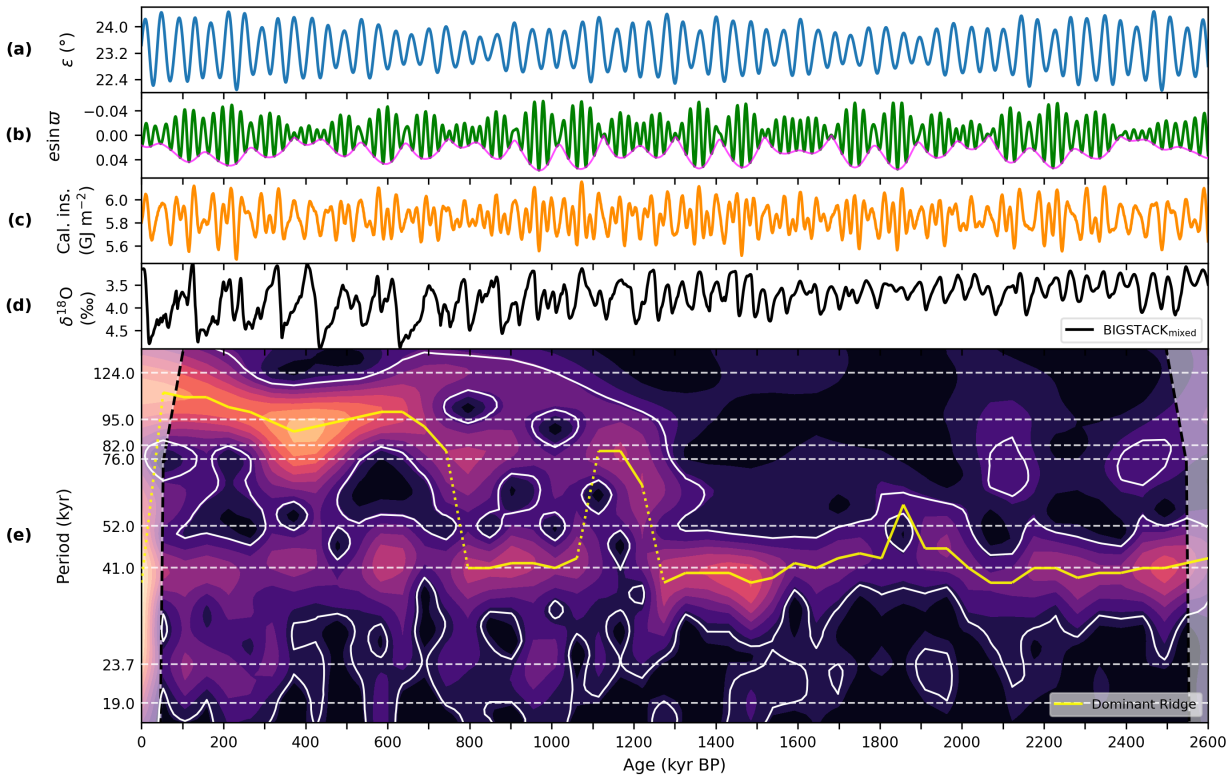


Figure S4: **Time-series and wavelet analyses of the benthic δ^{18}O stack record of BIGSTACK$_{\text{mixed}}$ (*7*), aligned with astronomical forcing (*12*) over the last 2.6 Myr.** (a) Obliquity (ε). (b) Climatic precession ($e \sin \varpi$, green) shown with its eccentricity envelope (e, magenta). (c) Caloric summer half-year insolation at 65°N (*13*). (d) The benthic δ^{18}O stack record of BIGSTACK$_{\text{mixed}}$ (*7*). (e) Wavelet power scalogram of the δ^{18}O record. The yellow line indicates the ridge of maximum wavelet power, drawn solid or dotted as in Fig. 1e. Areas enclosed by white dashed lines indicate power significant at the 95% confidence level against an AR(1) benchmark. Horizontal dashed lines denote major astronomical periodicities, including the 76-kyr and 52-kyr scales discussed in this study.

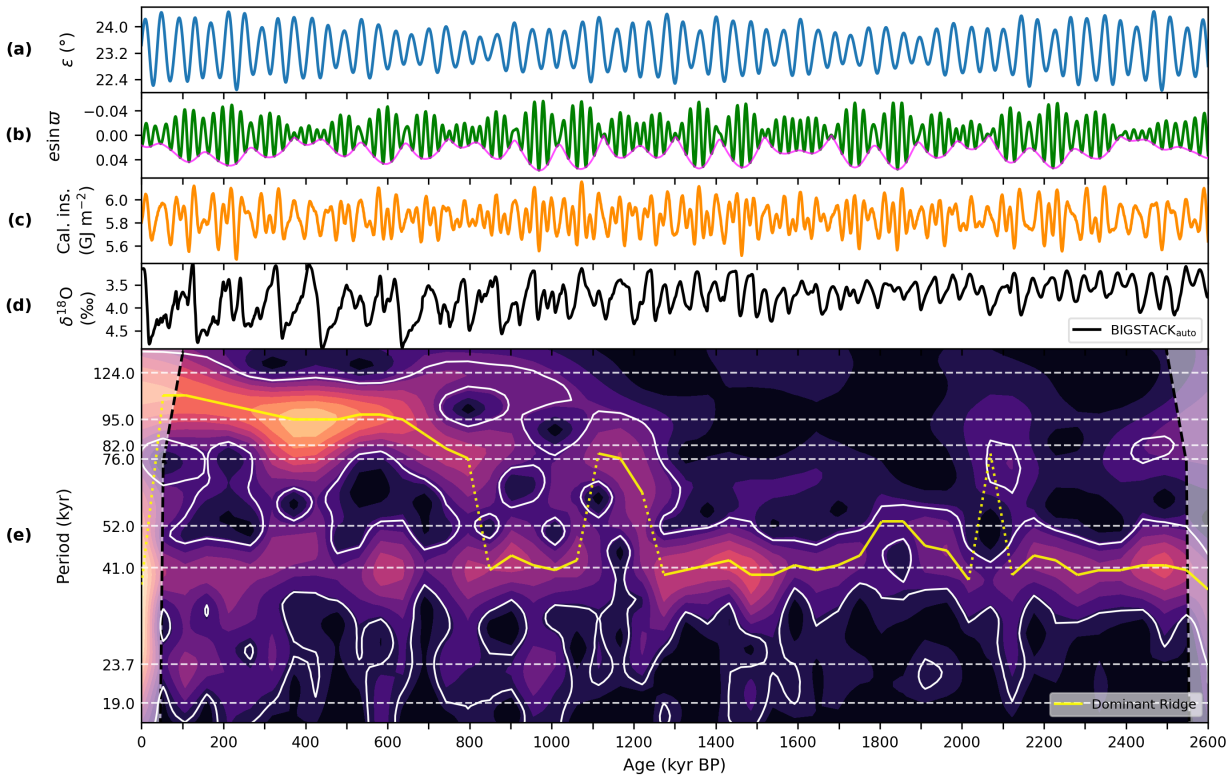


Figure S5: **Time-series and wavelet analyses of the benthic δ^{18}O stack record of BIGSTACK$_{\text{auto}}$ (*7*), aligned with astronomical forcing (*12*) over the last 2.6 Myr.** (a) Obliquity (ε). (b) Climatic precession ($e \sin \varpi$, green) shown with its eccentricity envelope (e, magenta). (c) Caloric summer half-year insolation at 65°N (*13*). (d) The benthic δ^{18}O stack record of BIGSTACK$_{\text{auto}}$ (*7*). (e) Wavelet power scalogram of the δ^{18}O record. The yellow line indicates the ridge of maximum wavelet power, drawn solid or dotted as in Fig. 1e. Areas enclosed by white dashed lines indicate power significant at the 95% confidence level against an AR(1) benchmark. Horizontal dashed lines denote major astronomical periodicities, including the 76-kyr and 52-kyr scales discussed in this study.

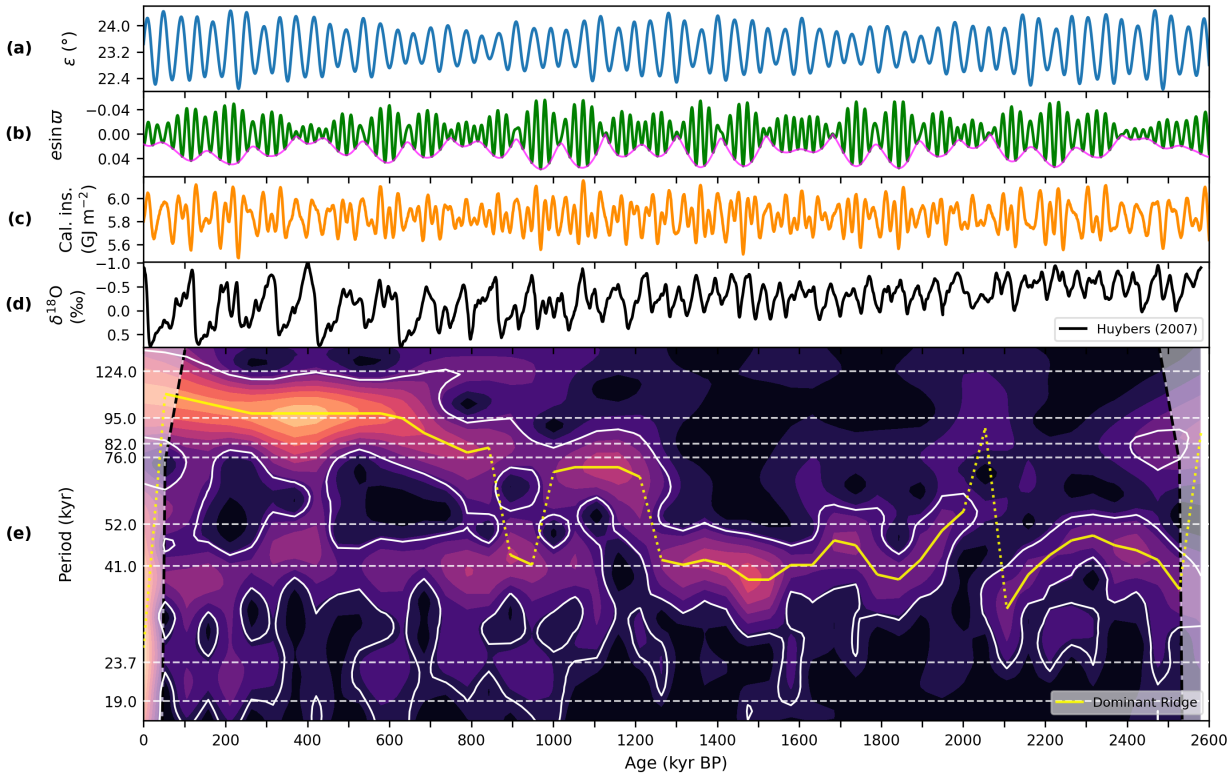


Figure S6: **Time-series and wavelet analyses of the benthic δ^{18}O stack record of Huybers (2007) (*36*), aligned with astronomical forcing (*12*) over the last 2.6 Myr.** (a) Obliquity (ε). (b) Climatic precession ($e \sin \varpi$, green) shown with its eccentricity envelope (e, magenta). (c) Caloric summer half-year insolation at 65°N (*13*). (d) The benthic δ^{18}O stack record of Huybers (2007) (*36*). (e) Wavelet power scalogram of the δ^{18}O record. The yellow line indicates the ridge of maximum wavelet power, drawn solid or dotted as in Fig. 1e. Areas enclosed by white dashed lines indicate power significant at the 95% confidence level against an AR(1) benchmark. Horizontal dashed lines denote major astronomical periodicities, including the 76-kyr and 52-kyr scales discussed in this study.

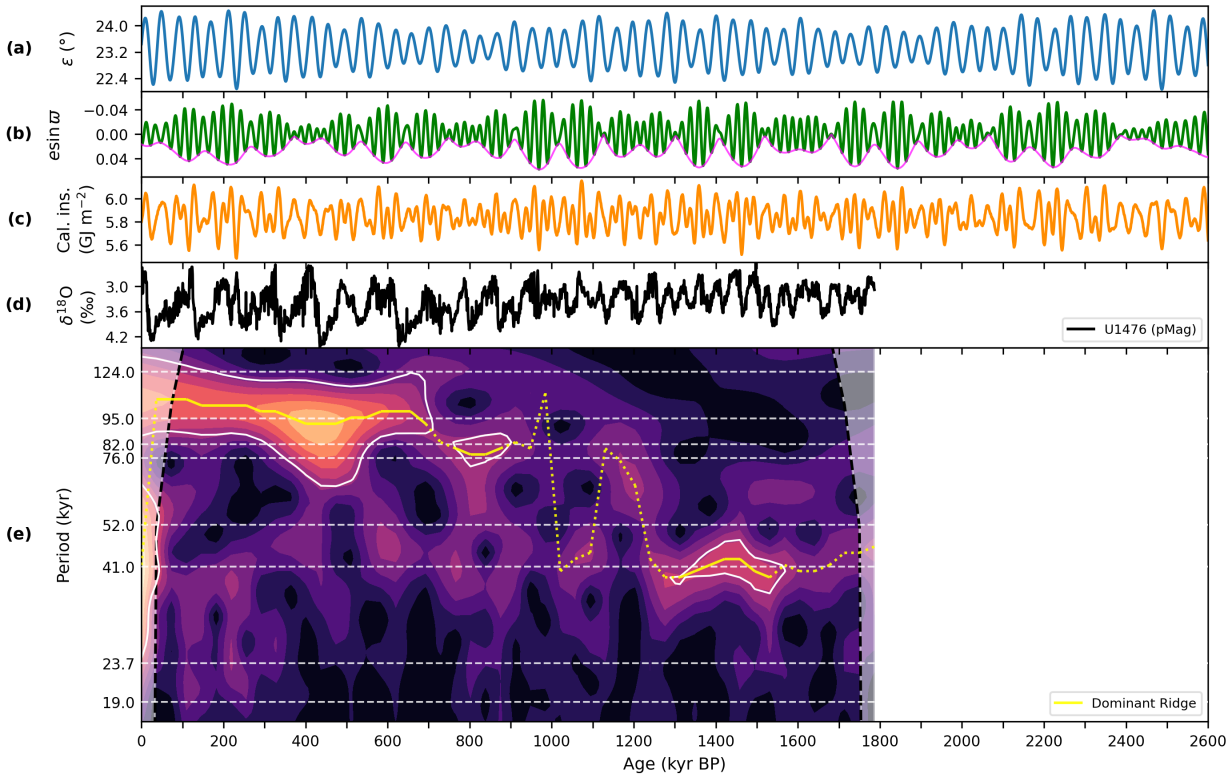


Figure S7: **Time-series and wavelet analyses of the benthic δ^{18}O record from U1476pMag (*26*), aligned with astronomical forcing (*12*) over the last 2.6 Myr.** (a) Obliquity (ε). (b) Climatic precession ($e \sin \varpi$, green) shown with its eccentricity envelope (e, magenta). (c) Caloric summer half-year insolation at 65°N (*13*). (d) The benthic δ^{18}O record from U1476pMag (*26*). (e) Wavelet power scalogram of the δ^{18}O record. The yellow line indicates the ridge of maximum wavelet power, drawn solid or dotted as in Fig. 1e. Areas enclosed by white dashed lines indicate power significant at the 95% confidence level against an AR(1) benchmark. Horizontal dashed lines denote major astronomical periodicities, including the 76-kyr and 52-kyr scales discussed in this study.

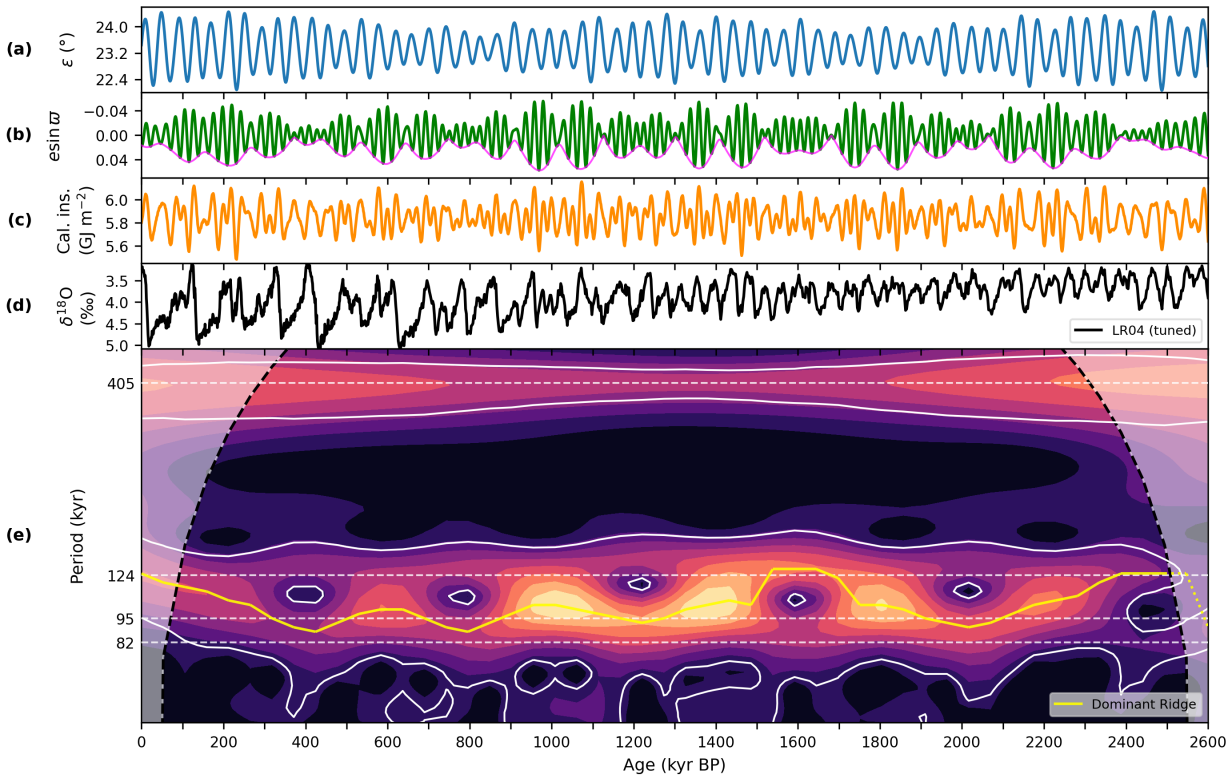


Figure S8: **Time-series and wavelet analyses of eccentricity, aligned with other astronomical elements (*12*) and the LR04 benthic δ^{18}O stack record over the last 2.6 Myr.** (a) Obliquity (ε). (b) Climatic precession ($e \sin \varpi$, green) shown with its eccentricity envelope (e, magenta). (c) Caloric summer half-year insolation at 65°N (*13*). (d) The orbitally tuned LR04 benthic δ^{18}O stack record (*8*). (e) Wavelet power scalogram of eccentricity. The yellow line indicates the ridge of maximum wavelet power obtained by omitting the 405-kyr band, drawn solid or dotted as in Fig. 1e. Areas enclosed by white dashed lines indicate power significant at the 95% confidence level against an AR(1) benchmark. Horizontal dashed lines denote major astronomical periodicities of eccentricity.

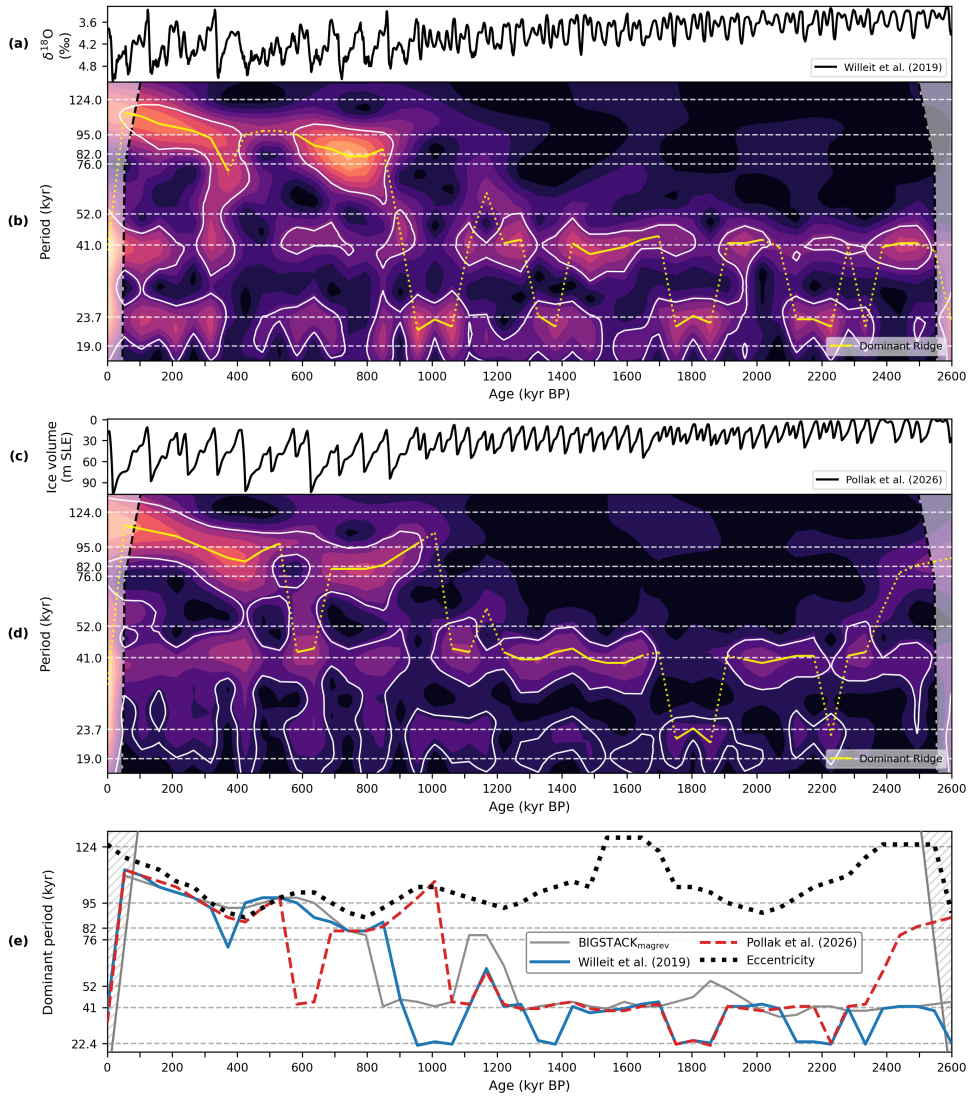


Figure S9: **Weighted wavelet analysis of the two model outputs.** (a) Simulated benthic δ^{18}O from the CLIMBER-2 transient simulation of Willeit et al. (2019) (*40*) and (b) its wavelet power scalogram. (c) Simulated global ice volume from the RAMP model of Pollak et al. (2026) (*41*) and (d) its scalogram. In (b) and (d), the yellow line traces the ridge of maximum wavelet power (solid or dotted as in Fig. 1e), areas enclosed by white lines indicate power significant at the 95% confidence level against an AR(1) benchmark, and horizontal dashed lines mark the periodicities discussed in the text. (e) Dominant period of the two model outputs compared with those of BIGSTACK$_{\text{magrev}}$ (gray) and eccentricity (black; obtained excluding the ~405-kyr band), computed as in Fig. 1f; the hatched region marks the cone of influence. Both models track the observed lengthening of the dominant period after ~700 ka, which follows that of eccentricity.

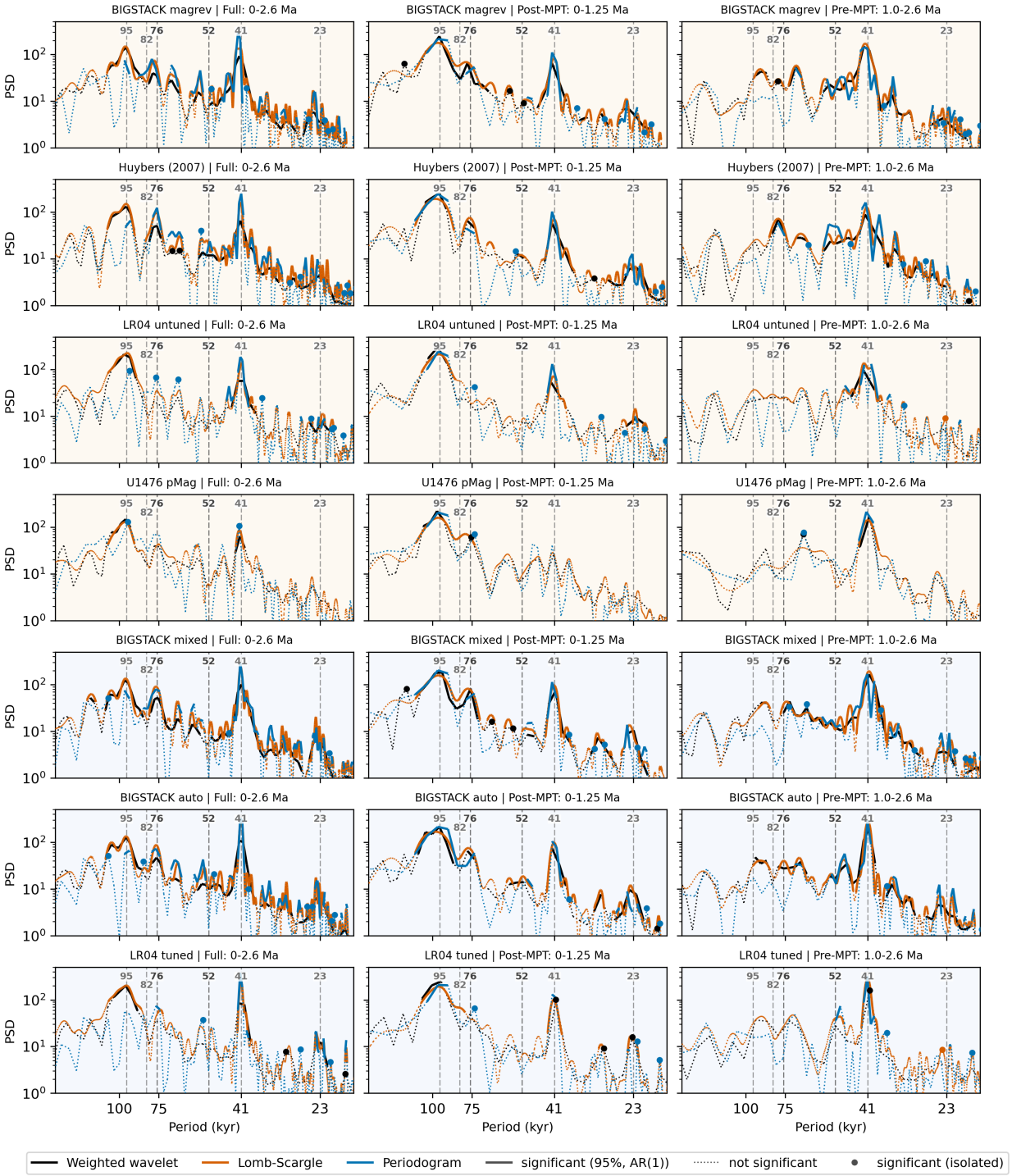


Figure S10: **Comparison of three spectral estimators for each benthic δ^{18}O record.** The full caption is given on the following page.

Figure S10 (continued). Rows correspond to records, grouped as tuning-free or minimally tuned ($\text{BIGSTACK}_{\text{magrev}}$ (*7*), Huybers (2007) (*36*), the untuned LR04 stack (*37*), and the U1476 record (*26*)) and orbitally tuned ($\text{BIGSTACK}_{\text{mixed}}$ and $\text{BIGSTACK}_{\text{auto}}$ (*7*), and the tuned LR04 stack (*8*)); columns correspond to the three time intervals. Each panel shows the power spectral density obtained by weighted wavelet spectral analysis (black), the Lomb–Scargle periodogram (orange), and the conventional periodogram (blue). Each curve is drawn as a thick solid line where the power exceeds the 95% confidence level against an AR(1) benchmark at both ends of a segment, and as a thin dotted line otherwise; a filled circle marks a single isolated frequency at which the power exceeds the threshold. The confidence levels themselves are not shown. Note that, unlike Figs. 2 and 3, only the 95% level is used here, so features significant at the 90% but not the 95% level appear as non-significant. Each method is applied following its own standard practice: the weighted wavelet analysis requires neither interpolation nor detrending; the Lomb–Scargle periodogram is applied to linearly detrended series without interpolation; and the conventional periodogram is applied to series interpolated at 1-kyr intervals and then linearly detrended. Window functions were selected separately for each method to give the clearest peak definition (boxcar for the Lomb–Scargle periodogram, Hann for the conventional periodogram). Vertical dashed lines denote key periodicities, with the 76-kyr and 52-kyr scales discussed in this study shown in darker gray. The U1476 record extends only to 1786 ka, so its panels cover 0–1.79 Ma and 1.0–1.79 Ma rather than the nominal intervals given in the panel titles.

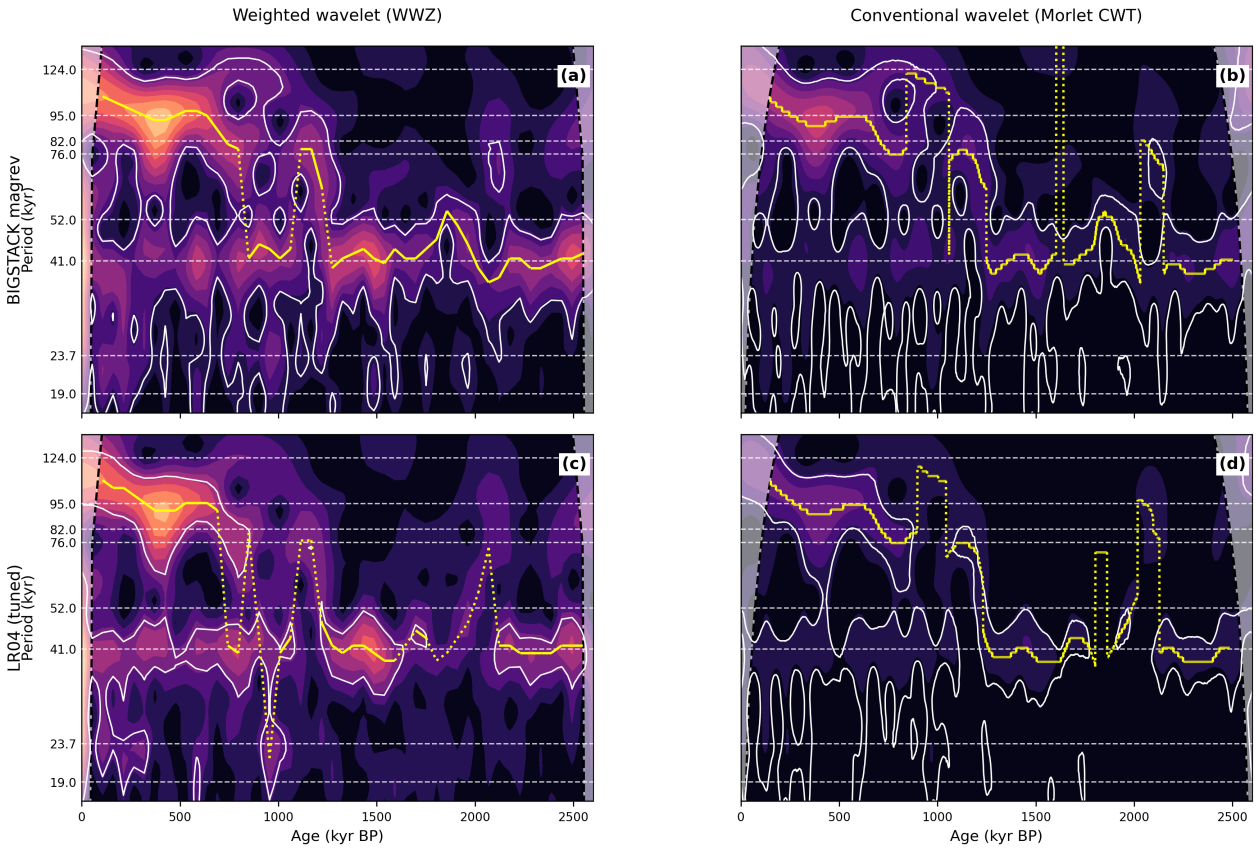


Figure S11: **Comparison of weighted wavelet and conventional Morlet wavelet transforms.** Scalograms of (a, b) $\text{BIGSTACK}_{\text{magrev}}$ (*7*) and (c, d) the orbitally tuned LR04 stack (*8*), computed with (a, c) the weighted wavelet transform and (b, d) a conventional continuous wavelet transform using the Morlet wavelet. Because the conventional transform requires evenly spaced data, the records were interpolated onto a uniform 1-kyr grid before analysis; no interpolation was applied for the weighted wavelet analysis. Areas enclosed by white contours indicate power significant at the 95% confidence level against an AR(1) benchmark. The yellow line traces the ridge of maximum wavelet power, drawn solid or dotted as in Fig. 1e; the ridge is not shown within the cone of influence (shaded). Horizontal dashed lines denote major astronomical periodicities. The intervals over which the ridge lies within the 70–82 kyr band and is significant are 743–796 and 1114–1167 ka in (a), 712–841, 1060–1203, and 2077–2146 ka in (b), and 716–877 and 1092–1194 ka in (d); the ridge does not reach significance within this band in (c). All analyses use `Pyleoclim` (version 1.2.0) (*35*).

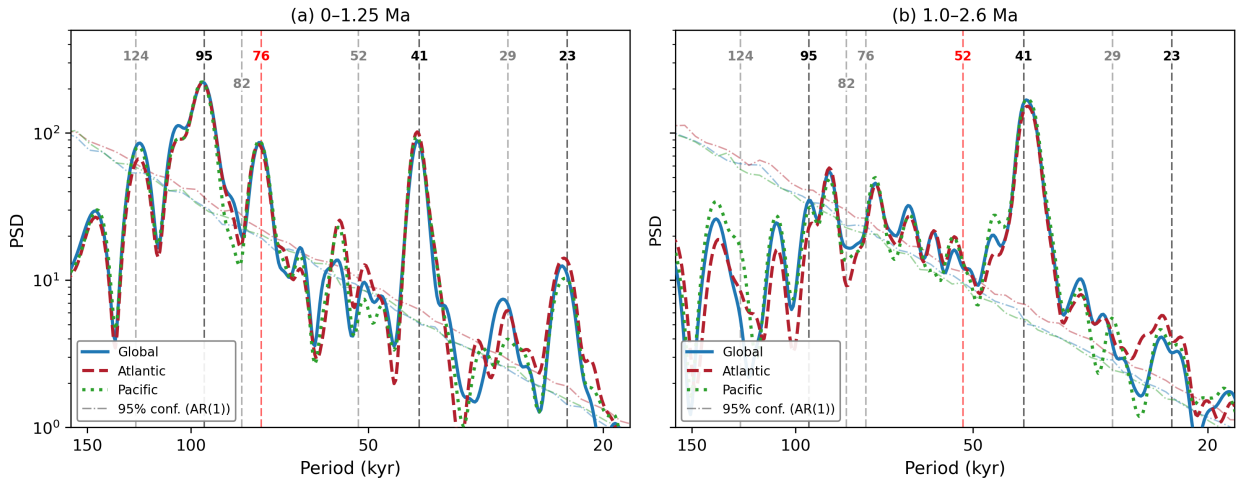


Figure S12: **Spatial coverage independence of the spectral analysis.** Power spectral densities (PSD) of the global BIGSTACK$_{\text{mixed}}$ stack and of its Atlantic-only (BIGSTACK$_{\text{mixedA}}$) and Pacific-only (BIGSTACK$_{\text{mixedP}}$) versions (*7*) for (a) 0–1.25 Ma and (b) 1.0–2.6 Ma. The three spectra share the same dominant peaks. Solid lines denote the PSD of the standardized series, and dashed/dotted lines indicate the 95% and 90% confidence levels against an AR(1) benchmark. Vertical dashed lines highlight key periodicities: eccentricity (124 and 95 kyr), obliquity (41 kyr), and climatic precession (23 kyr). Also indicated are the subharmonic of 41 kyr (82 kyr), the combination tone (29 kyr; $1/29 \approx 1/41 + 1/95$) (*46*), and specific timescales of interest in this study (76 kyr, red, and 52 kyr).

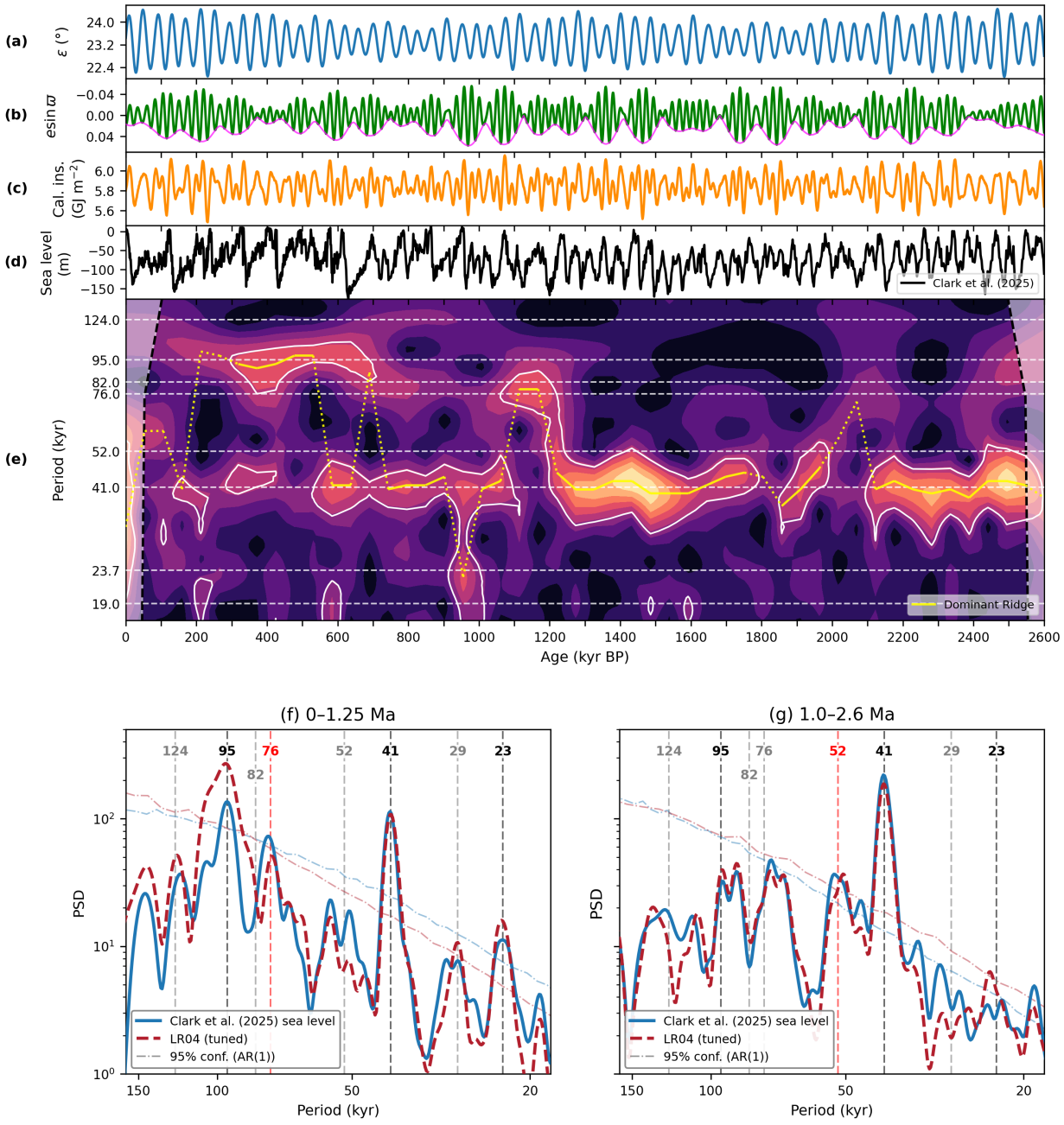


Figure S13: **Weighted wavelet analysis of the global mean sea level reconstruction of Clark et al. (2025) (*4*).** The full caption is given on the following page.

Figure S13 (continued). (a) Obliquity (ε). (b) Climatic precession ($e \sin \varpi$, green) shown with its eccentricity envelope (e, magenta) (*12*). (c) Caloric summer half-year insolation at 65°N (*13*). (d) Global mean sea level of Clark et al. (2025) (*4*), derived from the seawater δ^{18}O component of the Prob-stack benthic δ^{18}O record of Ahn et al. (2017) (*47*); low sea level (large ice volume) is plotted downward. (e) Wavelet power scalogram of the sea-level record, computed as for the δ^{18}O records (Figs. S2–S7). The yellow line indicates the ridge of maximum wavelet power, drawn solid or dotted as in Fig. 1e. Areas enclosed by white dashed lines indicate power significant at the 95% confidence level against an AR(1) benchmark. Horizontal dashed lines denote major astronomical periodicities, including the 76-kyr and 52-kyr scales discussed in this study. (f, g) Power spectral densities of the sea-level record (blue) and of the orbitally tuned LR04 stack (*8*) (red dashed) over (f) 0–1.25 Ma and (g) 1.0–2.6 Ma, computed as in Figs. 2 and 3; dash-dotted lines show the 95% confidence levels against AR(1) benchmarks. The sea-level record shows the ~76-kyr peak (76.8 kyr, significant at the 95% level) in (f) and the ~52-kyr peak (53.1 kyr, 95%) in (g), with no significant power at 58–66 kyr in either window. Over the last ~150 kyr, the ridge in (e) lies near 60 kyr rather than near 100 kyr as in the δ^{18}O records, because the reconstruction places the MIS 3 highstand at about −50 m, so that the last glacial cycle appears as two ~60-kyr oscillations.

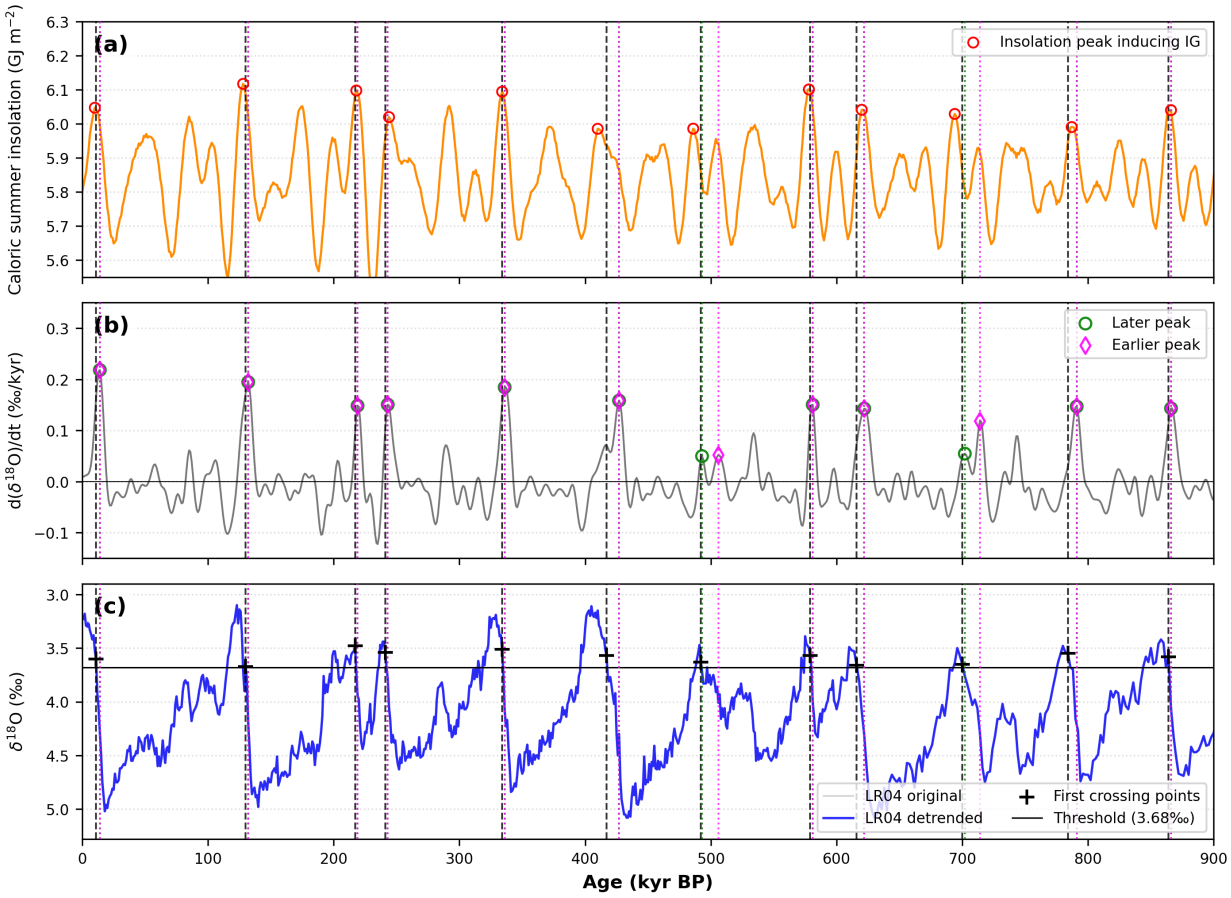


Figure S14: **Detailed deglaciation analysis and timing of interglacial onsets (0–900 ka).** (a) Caloric summer insolation at 65°N (*13*). Red open circles denote the insolation peaks leading to interglacials (*29*) (see Materials and Methods). (b) The rate of change in benthic δ^{18}O ($d(\delta^{18}\mathrm{O})/dt$) derived from the 10-kyr smoothed LR04 δ^{18}O record. Green circles and magenta diamonds highlight the local maxima in the deglaciation rate, representing later and earlier phases of ice-sheet retreat, respectively. (c) Benthic δ^{18}O records from the LR04 stack. The original record (light gray) is shown alongside the detrended series (*29*) (blue line) used for threshold analysis (see Materials and Methods). Black crosses ('+') mark the first points at which the detrended δ^{18}O falls below the 3.68‰ threshold, defining the onset of interglacial conditions. Vertical dashed lines (black) and dotted lines (green and magenta) indicate the timings of threshold crossings and peak deglaciation rates, respectively, highlighting the phase relationship between each insolation peak and climate response.

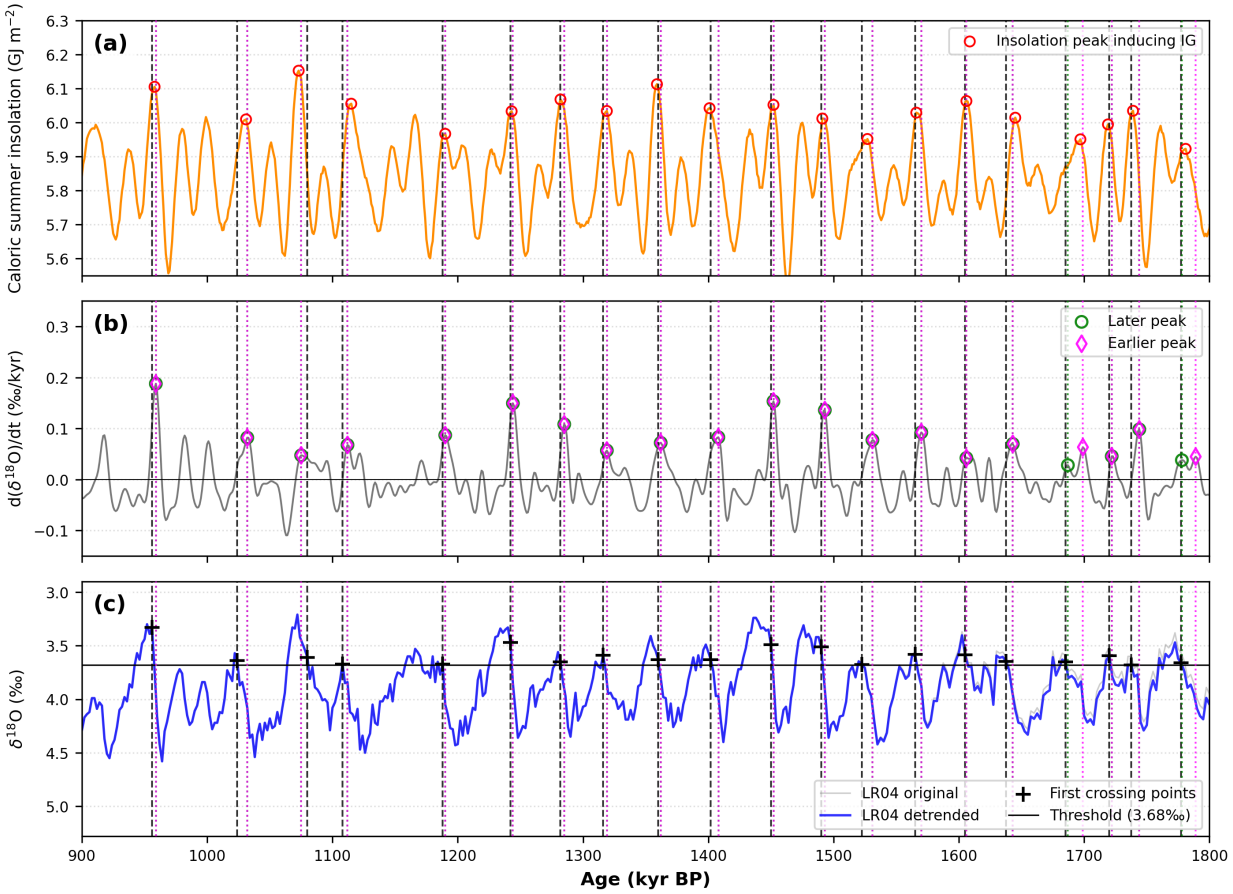


Figure S15: **Detailed deglaciation analysis and timing of interglacial onsets (900–1800 ka).** (a) Caloric summer insolation at 65°N (*13*). Red open circles denote the insolation peaks leading to interglacials (*29*) (see Materials and Methods). (b) The rate of change in benthic δ^{18}O ($d(\delta^{18}\mathrm{O})/dt$) derived from the 10-kyr smoothed LR04 δ^{18}O record. Green circles and magenta diamonds highlight the local maxima in the deglaciation rate, representing later and earlier phases of ice-sheet retreat, respectively. (c) Benthic δ^{18}O records from the LR04 stack. The original record (light gray) is shown alongside the detrended series (*29*) (blue line) used for threshold analysis (see Materials and Methods). Black crosses ('+') mark the first points at which the detrended δ^{18}O falls below the 3.68‰ threshold, defining the onset of interglacial conditions. Vertical dashed lines (black) and dotted lines (green and magenta) indicate the timings of threshold crossings and peak deglaciation rates, respectively, highlighting the phase relationship between each insolation peak and climate response.

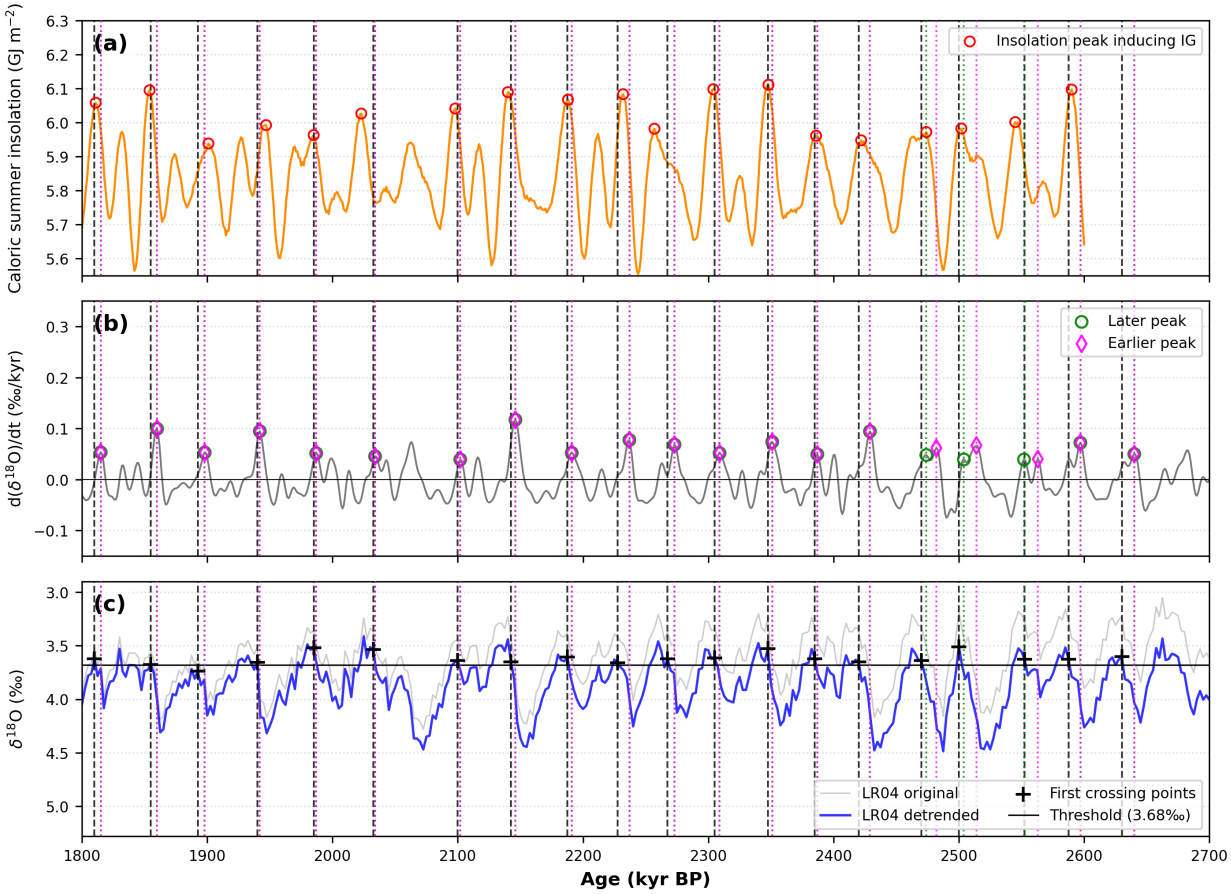


Figure S16: **Detailed deglaciation analysis and timing of interglacial onsets (1800–2700 ka).** (a) Caloric summer insolation at 65°N (*13*). Red open circles denote the insolation peaks leading to interglacials (*29*) (see Materials and Methods). (b) The rate of change in benthic δ^{18}O ($d(\delta^{18}\mathrm{O})/dt$) derived from the 10-kyr smoothed LR04 δ^{18}O record. Green circles and magenta diamonds highlight the local maxima in the deglaciation rate, representing later and earlier phases of ice-sheet retreat, respectively. (c) Benthic δ^{18}O records from the LR04 stack. The original record (light gray) is shown alongside the detrended series (*29*) (blue line) used for threshold analysis (see Materials and Methods). Black crosses ('+') mark the first points at which the detrended δ^{18}O falls below the 3.68‰ threshold, defining the onset of interglacial conditions. Vertical dashed lines (black) and dotted lines (green and magenta) indicate the timings of threshold crossings and peak deglaciation rates, respectively, highlighting the phase relationship between each insolation peak and climate response.

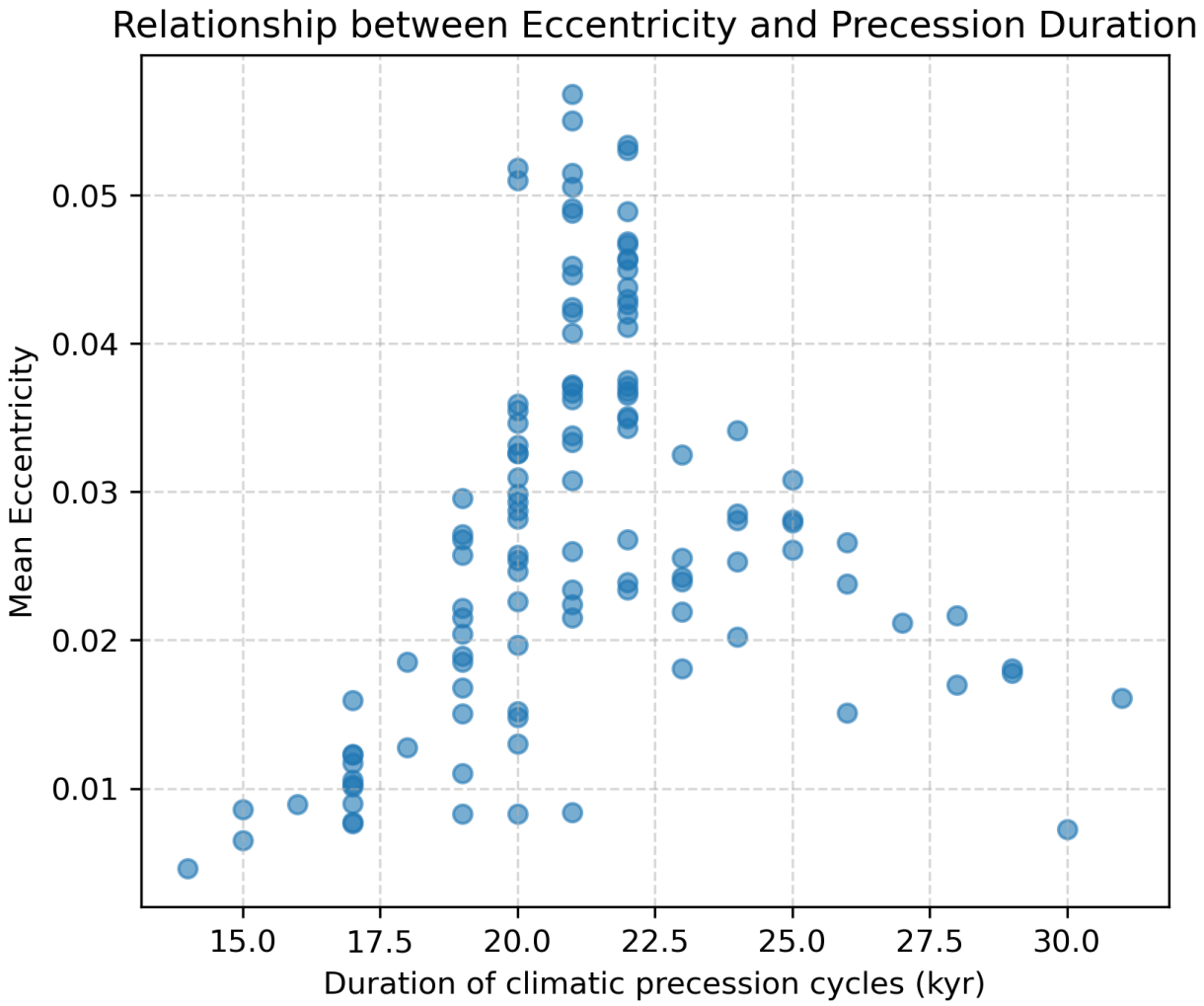


Figure S17: **Relationship between eccentricity and the duration of climatic precession cycles.** The duration of each climatic precession cycle is the spacing between successive precession minima, and the local mean of eccentricity is taken over the same interval.

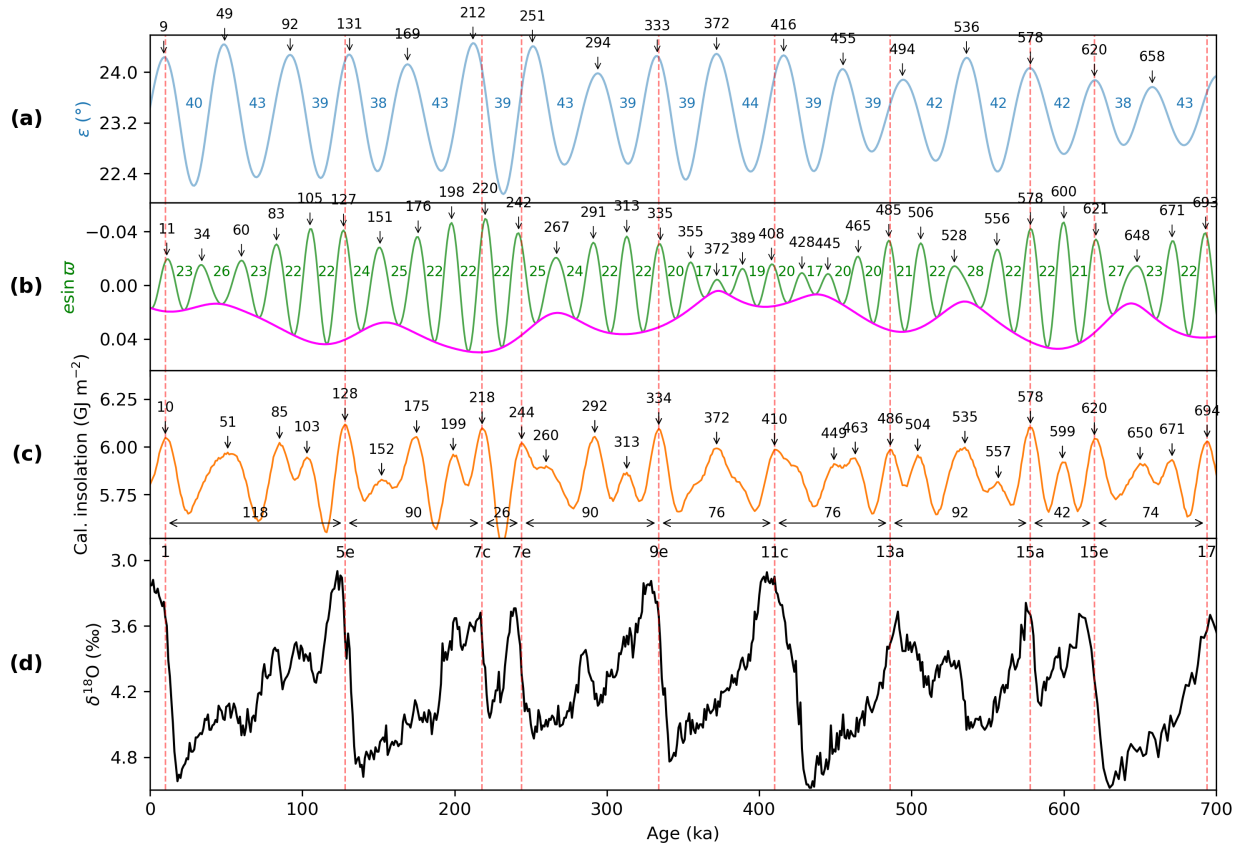


Figure S18: **Orbital forcing and glacial-interglacial cycles over the last 700 kyr.** (a) Obliquity (ε) with peak ages (ka) indicated by arrows. Peak-to-peak spacings are shown in blue between consecutive peaks. (b) Climatic precession ($e \sin \varpi$, green) and eccentricity (e, magenta). Note that the $e \sin \varpi$ axis is inverted to align with insolation peaks. Peak-to-peak spacings are shown in green between consecutive minima. (c) Caloric summer half-year insolation at 65°N (*13*). Horizontal double-headed arrows indicate the interglacial spacings (T_{ins}), where values correspond to the spacings between successive insolation maxima leading to interglacials. (d) LR04 δ^{18}O stack (*8*). Numbers at the top denote Marine Isotope Stages (MIS). Vertical red dashed lines across all panels mark the timing of insolation peaks that led to interglacials (*29*). The orbital solutions are from Laskar et al. (2004) (*12*).

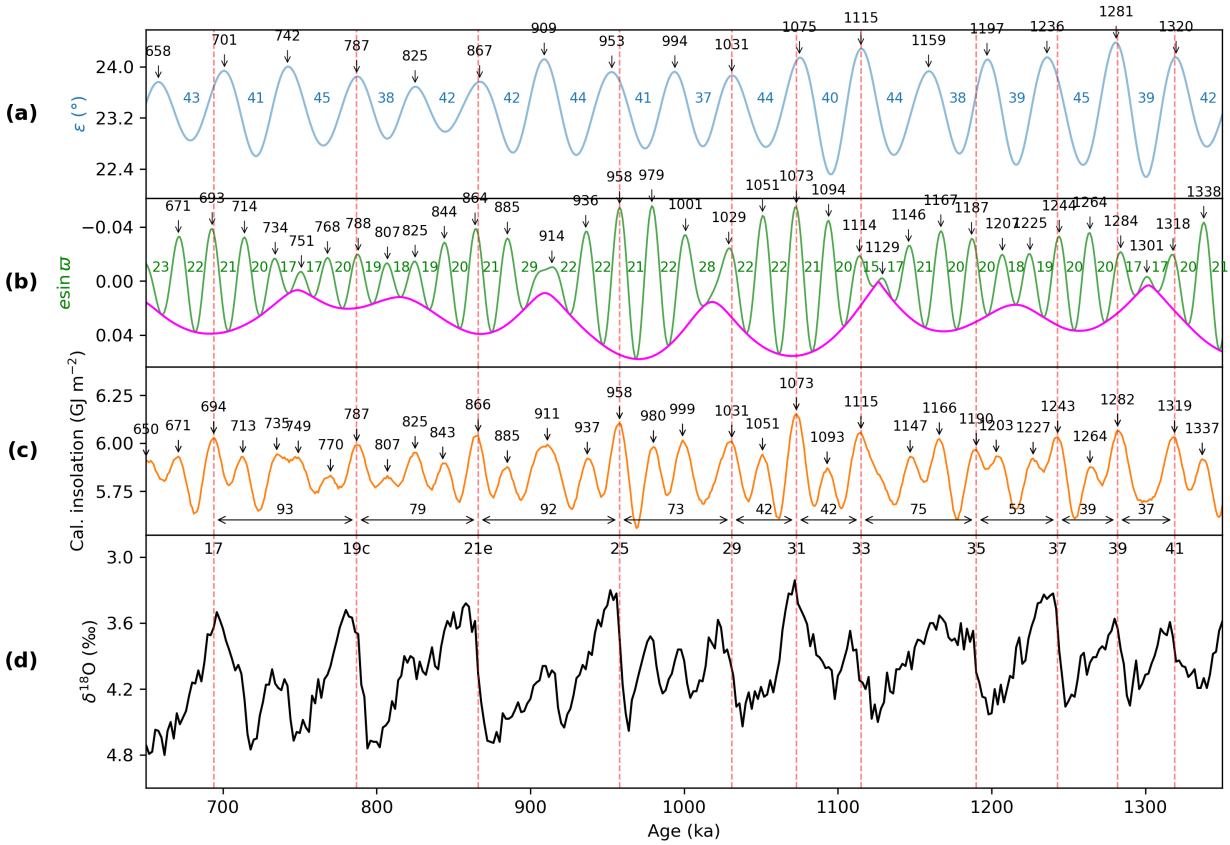


Figure S19: **Orbital forcing and glacial-interglacial cycles from 650 to 1350 ka.** (a) Obliquity (ε) with peak ages (ka) indicated by arrows. Peak-to-peak spacings are shown in blue between consecutive peaks. (b) Climatic precession ($e \sin \varpi$, green) and eccentricity (e, magenta). Note that the $e \sin \varpi$ axis is inverted to align with insolation peaks. Peak-to-peak spacings are shown in green between consecutive minima. (c) Caloric summer half-year insolation at 65°N (*13*). Horizontal double-headed arrows indicate the interglacial spacings (T_{ins}), where values correspond to the spacings between successive insolation maxima leading to interglacials. (d) LR04 δ^{18}O stack (*8*). Numbers at the top denote Marine Isotope Stages (MIS). Vertical red dashed lines across all panels mark the timing of insolation peaks that led to interglacials (*29*). The orbital solutions are from Laskar et al. (2004) (*12*).

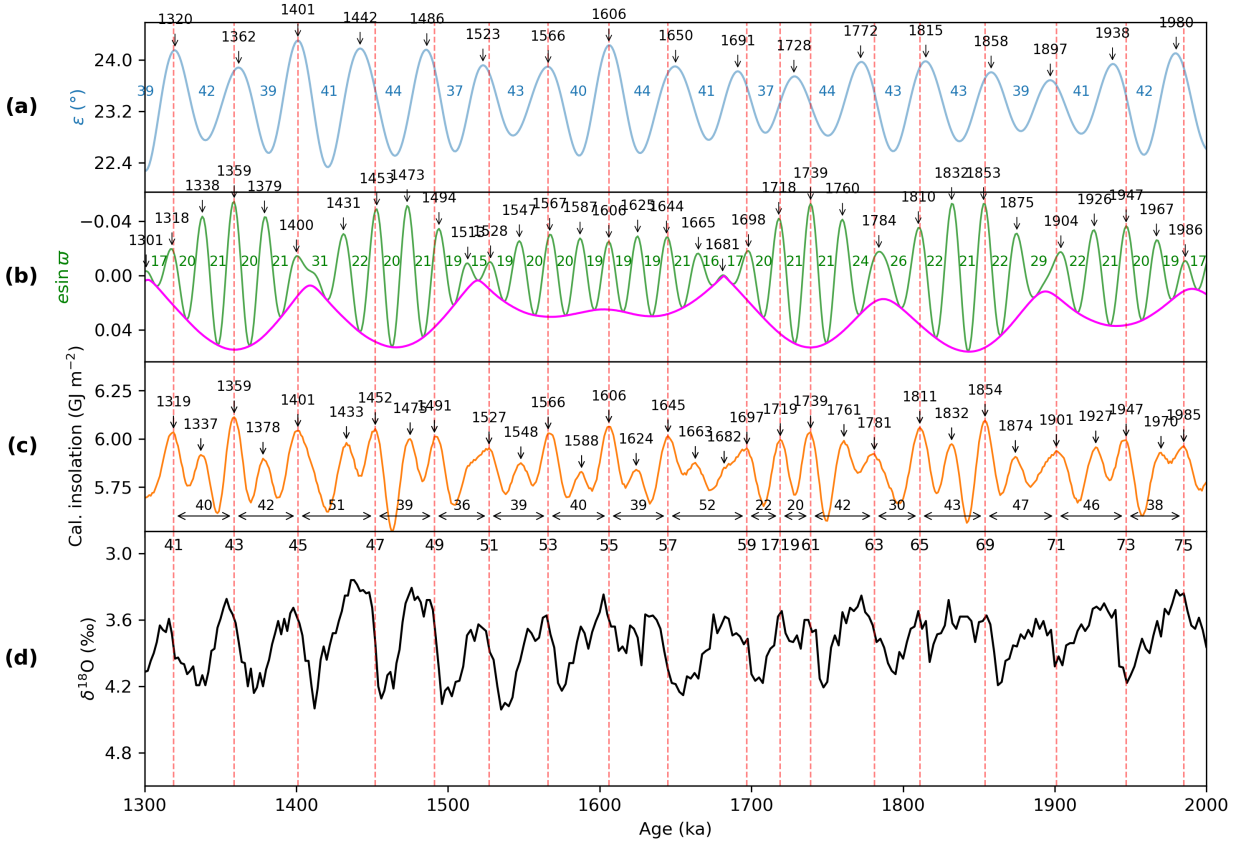


Figure S20: **Orbital forcing and glacial-interglacial cycles from 1300 to 2000 ka.** (a) Obliquity (ε) with peak ages (ka) indicated by arrows. Peak-to-peak spacings are shown in blue between consecutive peaks. (b) Climatic precession ($e \sin \varpi$, green) and eccentricity (e, magenta). Note that the $e \sin \varpi$ axis is inverted to align with insolation peaks. Peak-to-peak spacings are shown in green between consecutive minima. (c) Caloric summer half-year insolation at 65°N (*13*). Horizontal double-headed arrows indicate the interglacial spacings (T_{ins}), where values correspond to the spacings between successive insolation maxima leading to interglacials. (d) LR04 δ^{18}O stack (*8*). Numbers at the top denote Marine Isotope Stages (MIS). Vertical red dashed lines across all panels mark the timing of insolation peaks that led to interglacials (*29*). The orbital solutions are from Laskar et al. (2004) (*12*).

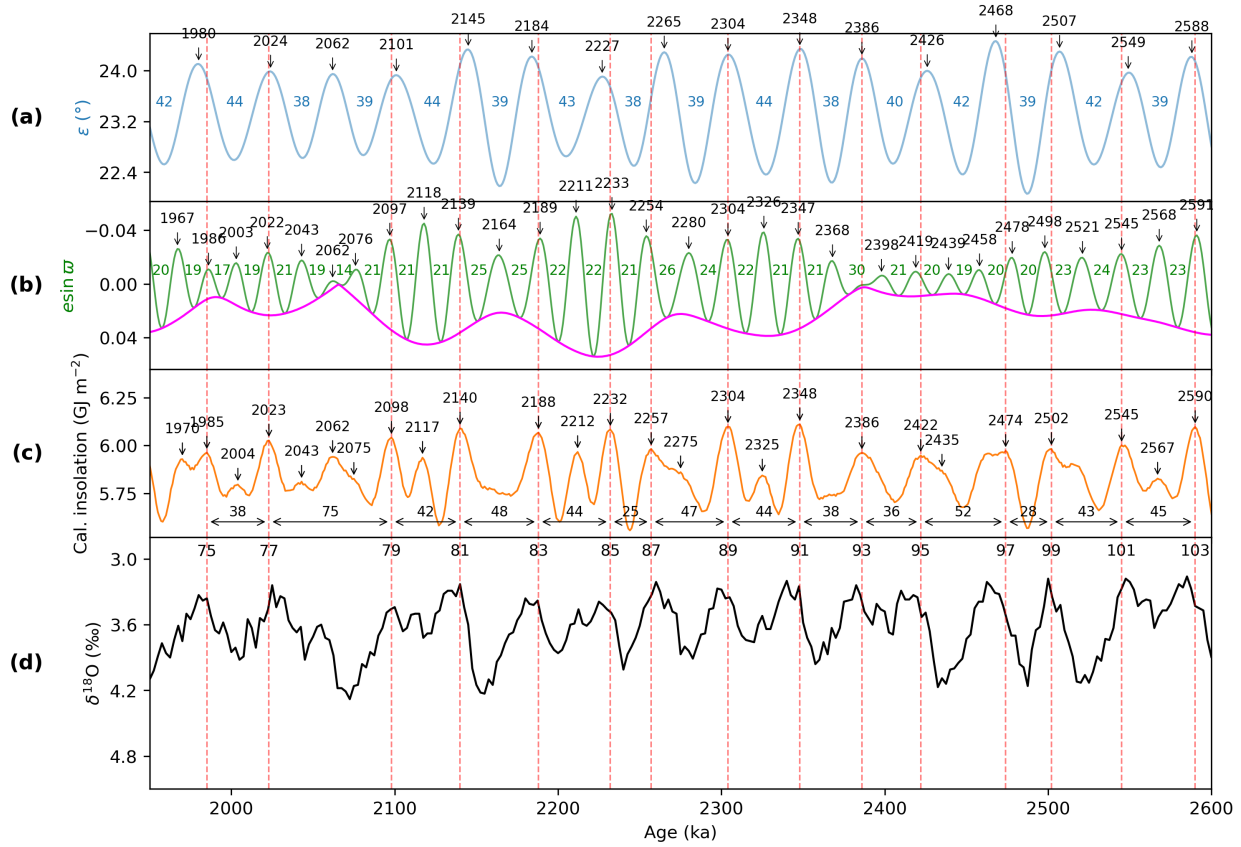


Figure S21: **Orbital forcing and glacial-interglacial cycles from 1950 to 2600 ka.** (a) Obliquity (ε) with peak ages (ka) indicated by arrows. Peak-to-peak spacings are shown in blue between consecutive peaks. (b) Climatic precession ($e \sin \varpi$, green) and eccentricity (e, magenta). Note that the $e \sin \varpi$ axis is inverted to align with insolation peaks. Peak-to-peak spacings are shown in green between consecutive minima. (c) Caloric summer half-year insolation at 65°N (*13*). Horizontal double-headed arrows indicate the interglacial spacings (T_{ins}), where values correspond to the spacings between successive insolation maxima leading to interglacials. (d) LR04 δ^{18}O stack (*8*). Numbers at the top denote Marine Isotope Stages (MIS). Vertical red dashed lines across all panels mark the timing of insolation peaks that led to interglacials (*29*). The orbital solutions are from Laskar et al. (2004) (*12*).

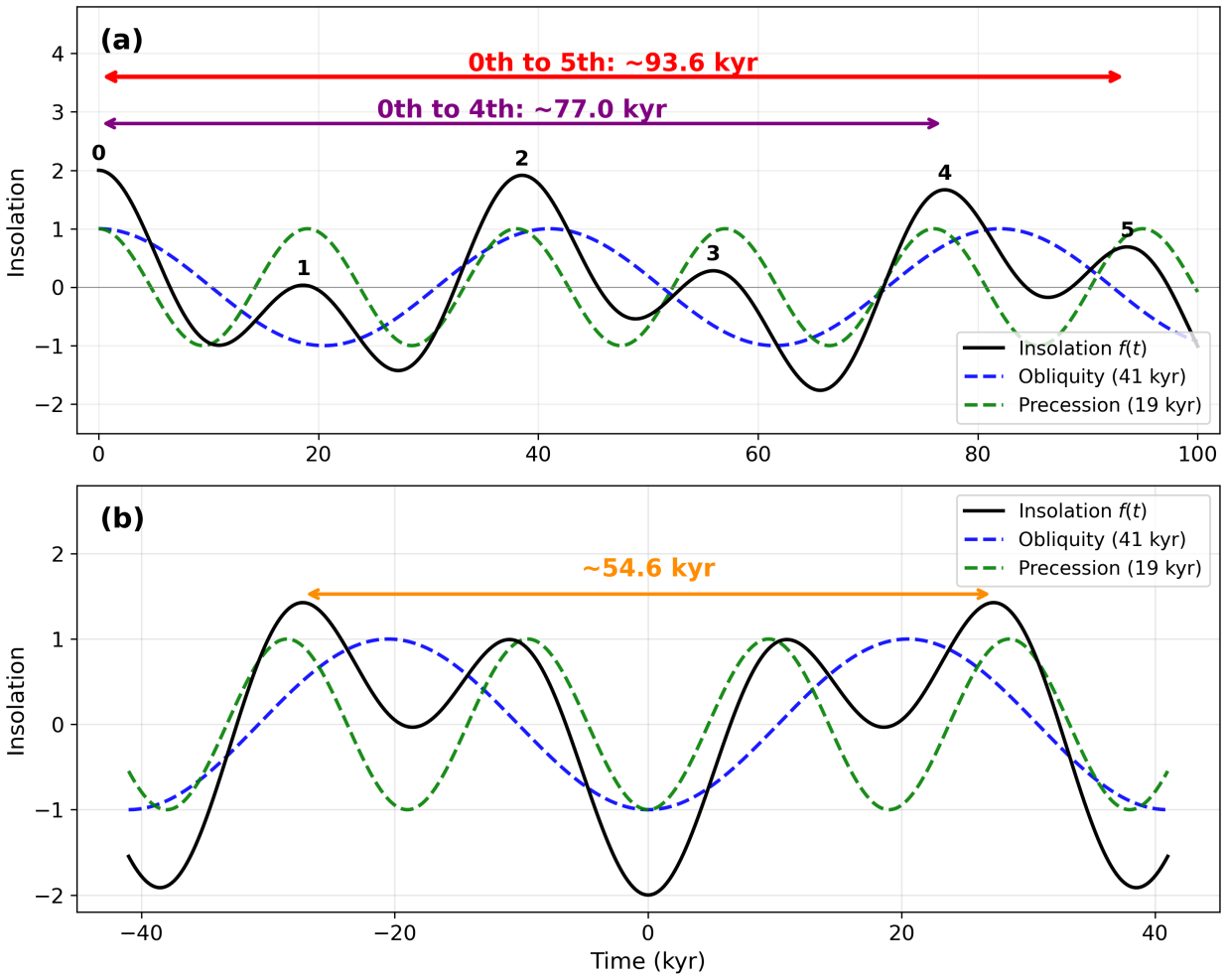


Figure S22: **Schematic representation of an insolation curve approximated by two harmonic components.** The insolation curve is assumed to be represented as the sum of two harmonic components: $\cos(2\pi t/19)$ (climatic precession) and $\cos(2\pi t/41)$ (obliquity). (a) The insolation curve is given by $f(t) = \cos(2\pi t/19) + \cos(2\pi t/41)$. (b) The insolation curve is given by $f(t) = -\cos(2\pi t/19) - \cos(2\pi t/41)$.

Supporting Information Table S1 for "Beyond the 100-kyr and 41-kyr dichotomy: ∼76- and ∼52-kyr signals and forbidden periodicities in Quaternary glacial cycles" by Takahito Mitsui

Creator: Takahito Mitsui (Juntendo University). (email: takahito321ATgmail.com)

Date: 25 September 2026

Description: This sheet shows the calculation of the insolation-based inter-deglaciation intervals (T_{ins}) by using the approximation formulae described in Supporting Information document. The caloric summer half-year insolation at 65°N is chosen as the insolation metric following Tzedakis et al. Nature (2017). It is calculated based on the orbital solution of Laskar et al. A&A (2004) using R-package 'Palinsol' created by Michel Crucifix. The insolation-based inter-deglaciation interval (T_{ins}) between two interglacials (called "start" and "end" below) is approximately given by the spacing between two insolation peaks that induce interglacials.

Marine Isotope Stage (MIS) of interglacial "end"	Marine Isotope Stage (MIS) of interglacial "start"	Insolation peak "end" (ka)	Insolation peak "start" (ka)	Actual inter-deglaciation interval (T_{ins}) (kyr)	Precession ($e\sin\varpi$) peak "end" (ka)	Precession ($e\sin\varpi$) peak "start" (ka)	Number of precession cycles	Local-mean precession period T_p (kyr)	Obliquity peak "end" (ka)	Obliquity peak "start" (ka)	Number of obliquity cycles	Local-mean obliquity period (kyr)	Formula type	Predicted Inter-deglaciation interval (T_{ins}) (kyr)	Difference = predicted T_{ins} - actual T_{ins} (kyr)	T_{later} (kyr)	T_{earlier} (kyr)
1	5*e*	10	128	118	11	127	5	23.2	9	131	3	40.67	5a	117.41	-0.59	118	118
5*e*	7*c*	128	218	90	127	220	4	23.25	131	212	2	40.5	4a	90.75	0.75	87	87
7*c*	7*e*	218	244	26	220	242	1	22	212	251	1	39	1b	25.64	-0.36	24	24
7*e*	9*e*	244	334	90	242	335	4	23.25	251	333	2	41	4a	90.84	0.84	93	93
9*e*	11*c*	334	410	76	335	408	4	18.25	333	416	2	41.5	4a	74.26	-1.74	91	91
11*c*	13a	410	486	76	408	485	4	19.25	416	494	2	39	*pp*	77	1	66	79
13a	15a	486	578	92	485	578	4	23.25	494	578	2	42	4a	91.13	-0.87	88	75
15a	15*e*	578	620	42	578	621	2	21.5	578	620	1	42	2a	42.79	0.79	41	41
15*e*	17	620	694	74	621	693	3	24	620	701	2	40.5	3a	74.1	0.1	80	92
17	19*c*	694	787	93	693	788	5	19	701	787	2	43	5a	93.77	0.77	89	77
19*c*	21*e*	787	866	79	788	864	4	19	787	867	2	40	4b	76.73	-2.27	75	75
21*e*	25	866	958	92	864	958	4	23.5	867	953	2	43	4a	92.32	0.32	93	93
25	29	958	1031	73	958	1029	3	23.67	953	1031	2	39	3a	72.78	-0.22	73	73
29	31	1031	1073	42	1029	1073	2	22	1031	1075	1	44	2a	44	2	43	43
31	33	1073	1115	42	1073	1114	2	20.5	1075	1115	1	40	2a	40.79	-1.21	37	37
33	35	1115	1190	75	1114	1187	4	18.25	1115	1197	2	41	4a	74.22	-0.78	78	78
35	37	1190	1243	53	1187	1244	3	19	1197	1236	1	39	3b	54.16	1.16	54	54
37	39	1243	1282	39	1244	1284	2	20	1236	1281	1	45	*pp*	40	1	41	41
39	41	1282	1319	37	1284	1318	2	17	1281	1320	1	39	2b	34.79	-2.21	34	34
41	43	1319	1359	40	1318	1359	2	20.5	1320	1362	1	42	*pp*	41	1	43	43
43	45	1359	1401	42	1359	1400	2	20.5	1362	1401	1	39	*pp*	41	-1	46	46
45	47	1401	1452	51	1400	1453	2	26.5	1401	1442	1	41	2a	50.04	-0.96	44	44
47	49	1452	1491	39	1453	1494	2	20.5	1442	1486	1	44	2*c*	39.73	0.73	41	41
49	51	1491	1527	36	1494	1528	2	17	1486	1523	1	37	*pp*	34	-2	38	38
51	53	1527	1566	39	1528	1567	2	19.5	1523	1566	1	43	2a	39.66	0.66	39	39
53	55	1566	1606	40	1567	1606	2	19.5	1566	1606	1	40	2a	39.19	-0.81	36	36
55	57	1606	1645	39	1606	1644	2	19	1606	1650	1	44	2a	38.88	-0.12	37	37
57	59	1645	1697	52	1644	1698	3	18	1650	1691	1	41	3b	52.09	0.09	44	56
59	1719	1697	1719	22	1698	1718	1	20	1691	1728	1	37	1*c*	21.55	-0.45	35	23
1719	61	1719	1739	20	1718	1739	1	21	1728	1728	0	n/a	*pp*	21	1	22	22
61	63	1739	1781	42	1739	1784	2	22.5	1728	1772	1	44	2*c*	43.12	1.12	34	45
63	65	1781	1811	30	1784	1810	1	26	1772	1815	1	43	1b	30.24	0.24	37	26
65	69	1811	1854	43	1810	1853	2	21.5	1815	1858	1	43	*pp*	43	0	45	45
69	71	1854	1901	47	1853	1904	2	25.5	1858	1897	1	39	2b	47.49	0.49	38	38
71	73	1901	1947	46	1904	1947	2	21.5	1897	1938	1	41	2*d*	44.58	-1.42	44	44
73	75	1947	1985	38	1947	1986	2	19.5	1938	1980	1	42	2*c*	37.81	-0.19	45	45
75	77	1985	2023	38	1986	2022	2	18	1980	2024	1	44	2b	37.11	-0.89	47	47
77	79	2023	2098	75	2022	2097	4	18.75	2024	2101	2	38.5	4b	75.38	0.38	68	68
79	81	2098	2140	42	2097	2139	2	21	2101	2145	1	44	*pp*	42	0	44	44
81	83	2140	2188	48	2139	2189	2	25	2145	2184	1	39	2b	46.86	-1.14	45	45
83	85	2188	2232	44	2189	2233	2	22	2184	2227	1	43	2b	43.79	-0.21	46	46
85	87	2232	2257	25	2233	2254	1	21	2227	2265	1	38	1b	24.47	-0.53	36	36
87	89	2257	2304	47	2254	2304	2	25	2265	2304	1	39	2a	47.28	0.28	36	36
89	91	2304	2348	44	2304	2347	2	21.5	2304	2348	1	44	2a	43.19	-0.81	42	42
91	93	2348	2386	38	2347	2398	undef.	undef.	2348	2386	1	38	$O_2-(P_1+O_1)/2$	38.5	0.5	36	36
93	95	2386	2422	36	2398	2419	undef.	undef.	2386	2426	1	40	$(O_2+P_2)/2-O_1$	36.5	0.5	42	42
95	97	2422	2474	52	2419	2478	3	19.67	2426	2468	1	42	3b*	51.96	-0.04	45	53
97	99	2474	2502	28	2478	2498	1	20	2468	2507	1	39	1b*	27.94	-0.06	30	32
99	101	2502	2545	43	2498	2545	2	23.5	2507	2549	1	42	2*c*	45.05	2.05	48	49
101	103	2545	2590	45	2545	2591	2	23	2549	2588	1	39	2b	44.22	-0.78	45	34

Note: Special rules are employed for MIS 99-97, 97-95, 95-93, and 93-91, where eccentricity is particularly low. See Supplementary Text. For MIS 95-93 and 93-91, the number of precession cycles and the local-mean precession period are undefined because the bounding insolation peaks are obliquity maxima at near-zero eccentricity. These two spacings are excluded from Fig. 6 and from the statistics of $T_{\mathrm{ins}} - nT_p$.